STARK SHIFTS AND TUNNELING RATES FOR RYDBERG STATES OF SODIUM IN THE HIGH FIELD LIMIT

by

Michael G. Littman

A.B., summa cum laude, Brandeis University
(1972)

Submitted in partial fulfillment
of the requirements for the
degree of

DOCTOR OF PHILOSOPHY

at the

MASSACHUSETTS INSTITUTE OF TECHNOLOGY
November 1976

Signature of Author.....Michael G. Littman.....
Department of Physics

Certified by.....Daniel Kleppner.....
Thesis Supervisor

Accepted by.....
Chairman, Department Committee

STARK SHIFTS AND TUNNELING RATES FOR RYDBERG STATES OF SODIUM IN THE HIGH FIELD LIMIT

by

Michael G. Littman

Submitted to the Department of Physics
in November of 1976 in partial fulfillment of the requirements
for the degree of Doctor of Philosophy.

ABSTRACT

We have studied the effect of a strong electric field on the energies and spontaneous ionization probabilities for excited states (n = 12 - 15) of sodium. The measured Stark energies agree with theoretical values that were calculated using the Coulomb approximation. The measured ionization rates for the lowest m=2 Stark components of a given term are in agreement with rates that were calculated for corresponding hydrogen states. The systematics of the ionization of the higher sublevels, however, is in serious disagreement with hydrogenic theory because of level mixing.

Thesis Supervisor: Professor Daniel Kleppner

to my father,

the late Maxwell L. Littman M.D.,Ph.D.

CONTENTS

INTRODUCTION

Ionization of hydrogen in a static electric field by electron tunneling has evoked continuing interest since the early days of quantum mechanics, and has assumed new importance with the growing interest in highly excited atoms. Many useful experimental techniques based upon the ionization characteristics of these atoms have been developed. A detailed understanding of the ionization process is desirable to assure the validity of tunneling calculations, and is essential in view of the scope of the experimental work whose interpretation rests on it. We present here first measurements of the ionization rates of individual Stark sublevels of sodium. The Stark structure of the $|m|=2$ Stark states is well described by hydrogenic theory except in small regions near level anti-crossings. We find that the ionization rates for the low-lying Stark sublevels of several terms are in excellent agreement with the rates that have been calculated for hydrogen. For the higher-lying sublevels, however, there is serious disagreement. The discrepancy is due to level mixing with ionizing levels which has been neglected in existing tunneling calculations.

In chapter I, the field ionization of Stark levels in hydrogen is discussed in detail. Chapter II describes the theory that we have applied to determine the Stark structure of alkalis, in particular, sodium. In chapter III we discuss both the equipment and the techniques that we have used to carry out the field ionization experiments. Chapter IV contains a description of the six experiments that we have performed. The first four experiments deal with the problems of exciting, detecting, and identifying specific Stark states. The last two experiments concern measurements of spontaneous field ionization rates of selected Stark levels in sodium.

UNITS

Throughout this thesis we assume that all quantities are in atomic units (ie. $e=\hbar=m=1$) unless noted otherwise. Listed in the table below are the conversion factors for the units which were most often used.

Unit	Value	Conversion Factor	Known as
length	$a_o = \frac{\hbar^2}{me^2}$	5.292×10^{-9}cm $\approx \frac{1}{2}$ Å	bohr
charge	e	4.803×10^{-10} esu	electron charge
mass	m	9.108×10^{-28} gm	electron mass
electric field strength	$\frac{e}{a^2}$	5.142×10^{3}V/cm $\approx$ 5GV/cm	
energy	$\frac{e^2}{a}$	$2 \times R_{\infty} = 27.2$eV $= 219474$cm^{-1}	hartree
time	$\frac{\hbar^3}{me^4}$	2.419×10^{-17}sec	

CHAPTER I

ELECTRIC FIELD IONIZATION OF HYDROGEN

I.1 Introduction to Ionization Theory

In this chapter we shall examine the behaviour of hydrogen in weak to strong electric fields. In the next section the Stark problem is treated by separating the three-dimensional Schroedinger equation into three one-dimensional equations in parabolic coordinates. Here we present a simplified treatment of field ionization in rectilinear coordinates so that the reader can develop an understanding of the process in a familiar basis. We assume that the electron is confined to motion along the z axis, parallel to the direction of the field. We also assume that the total energy, W, is known. The one-dimensional Schroedinger equation is,

$$\left\{ -\frac{1}{2}\frac{d^2}{dz^2} + V(z) \right\} \psi(z) = W\psi(z)$$

where $V(z) = -1/|z| - Fz$. This potential function is plotted in Fig. I.1-1a for $F>0$. Note that the potential curve

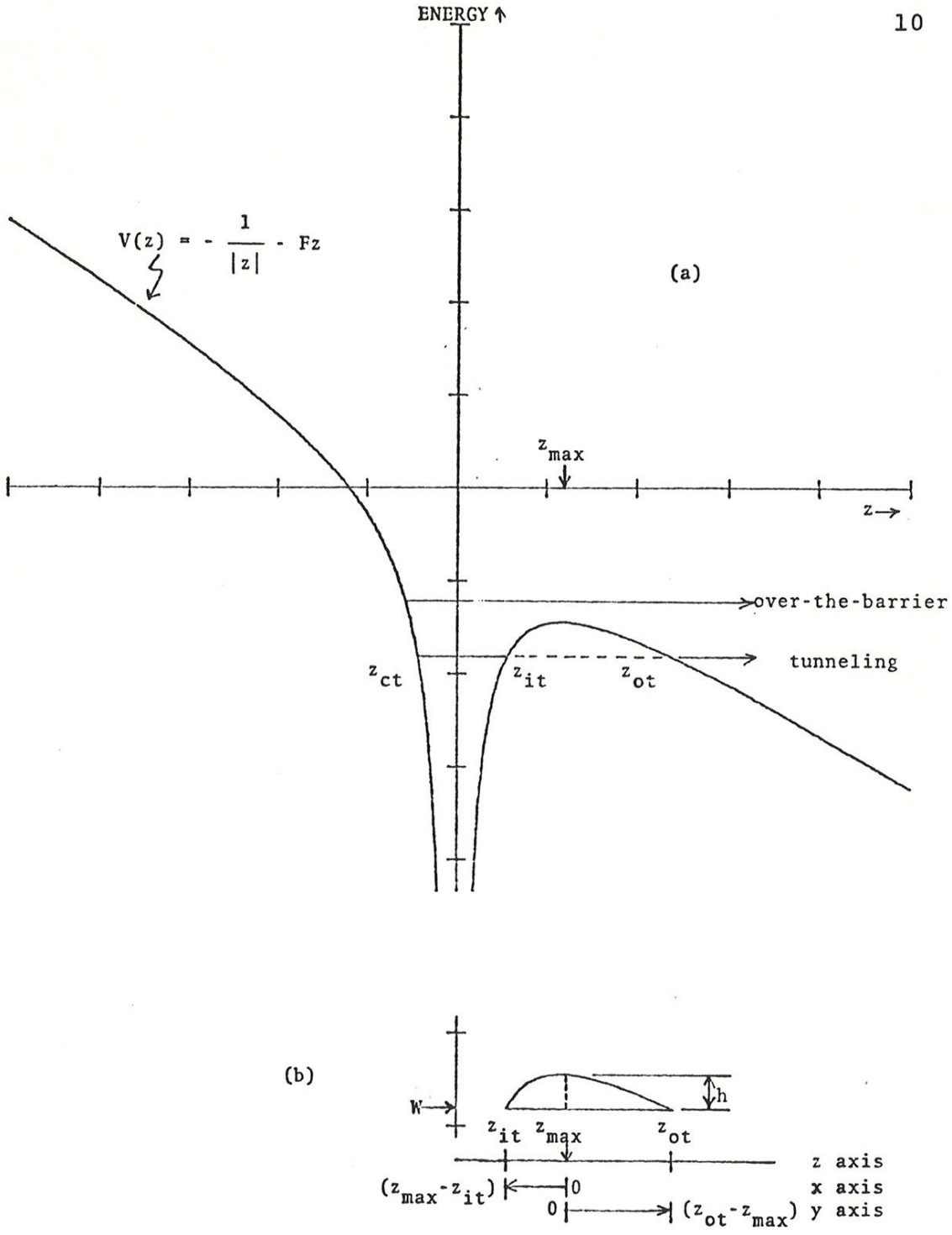

FIGURE I.1-1

(a) One-dimensional hydrogen potential in a static electric field.
(b) Parabola approximation to potential in regions, $z_{it} < z < z_{max}$ and $z_{max} < z < z_{ot}$.

increases monotonically toward the cathode, but that toward the anode the curve has a local maximum at $z=z_{max}$. The location of the potential maximum is determined by the condition,

$$\left.\frac{dV(z)}{dz}\right|_{z=z_{max}} = 0 \quad ,$$

which is satisfied when $z_{max}=1/\sqrt{F}$. The maximum value for the potential is $V(z_{max})=-2\sqrt{F}$.

We now examine the classical solution for an electron which is initially located at the turning point toward the cathode, $z=z_{ct}$. When released, this electron will proceed toward $z=+\infty$ unless $W<V(z_{max})$, in which case it will oscillate between z_{ct} and z_{it} as indicated in Fig. I.1-1a. For a given field the condition for "classical" over-the-barrier ionization is $W>-2\sqrt{F}$, or alternatively, for a given energy the condition is $F>F_o$, where $F_o=W^2/4$. We estimate F_o by taking W to be the familiar zero field hydrogen value, $-1/2n^2$, and obtain, $F_o=1/16n^4$. Thus, a field of 300 MV/cm (1/16 au) is needed to ionize the ground state, while a mere 3 V/cm ($1/16 \times 10^{-8}$ au) is sufficient to ionize the n=100 state.

It is well known that the electron can escape via tunneling for fields below F_o. To determine the ionization rate for this process, we use the WKB method. The rate is given by the product of the transmission probability (T) through the barrier and the frequency with which the paricle oscillates in the well. For this discussion we will make the assumption that the oscillation frequency is independent of the field and is equal to the classical value, $1/2\pi n^3$. The WKB expression for the transmission probability is [BOH 51,sect. 12.10],

$$T \approx \exp\left\{ - \int_{z_{it}}^{z_{ot}} 2\sqrt{2(V(z)-W)}\, dz \right\} \quad (I.1.1)$$

where z_{it} and z_{ot} are the inner and outer turning points (see Fig. I.1-1a). To evaluate the integral in this equation we approximate the quantity V(z)-W in the region between these two turning points by parabolas (see Fig. I.1-1b),

$$h\left[1-\left(\frac{x}{z_{max}-z_{it}}\right)^2\right] \quad ; \quad z_{it}<z<z_{max}$$

$$h\left[1-\left(\frac{y}{z_{ot}-z_{max}}\right)^2\right] \quad ; \quad z_{max}<z<z_{ot} \quad .$$

Here h, the height of the barrier, is $-2\sqrt{F}-W$ and z_{it}, z_{ot} satisfy the equation,

$$W = -\frac{1}{|z|} - Fz$$

which gives,

$$z_{it,ot} = \frac{-W \pm \sqrt{W^2-4F}}{2F}$$

Using these expressions, we obtain the following value for the transmission probability,

$$T \approx \exp\left\{-\frac{h^{3/2}}{F}\right\} . \qquad (I.1-2)$$

To examine this expression for fields near F_o we let $F=F_o-\delta F$, which gives,

$$T \approx \exp\left\{-\frac{(\delta F)^{3/2}}{F_o^{3/4}}\right\} .$$

Observe that levels ionize by tunneling at rates that increase exponentially as fields are raised near the "classical" value, that is, when δF approaches zero. A graph of ionization rate versus field according to eq. I.1-2 for levels having n=6-23 is given in Fig. I.1-2. It will be shown in sect. I.5 that these results are in qualitative agreement with those of the more precise analysis presented in that section.

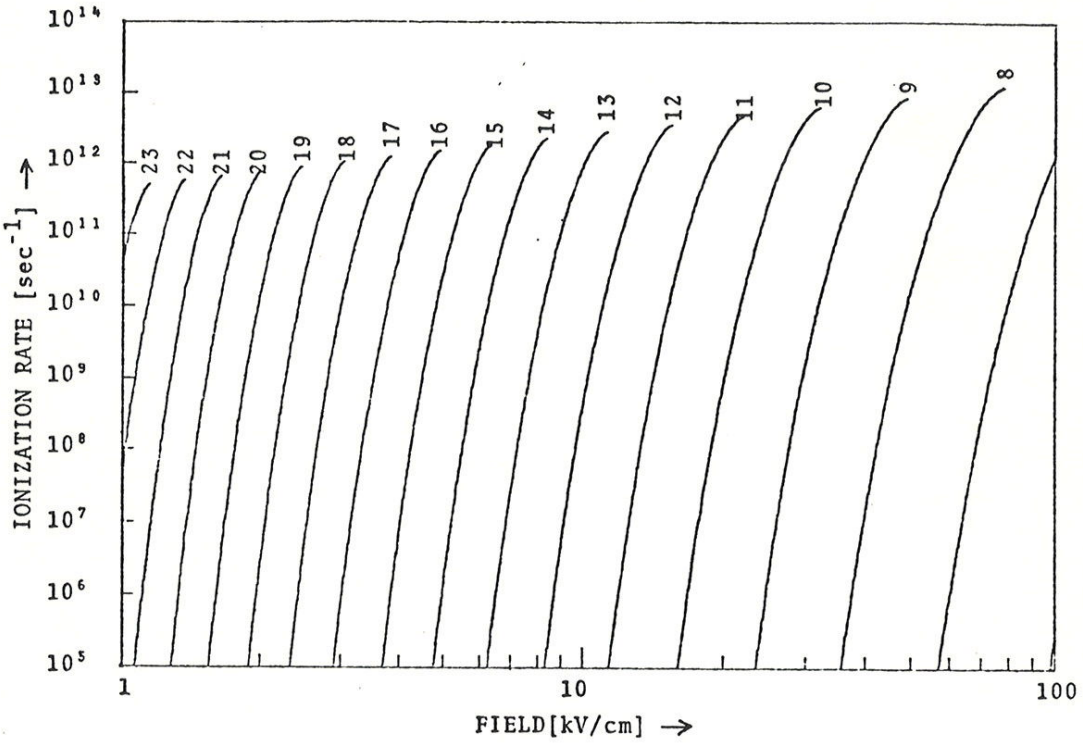

FIGURE I.2-1

Ionization rate versus field according to WKB one-dimentional potential approximation for n=6-23 (ignoring Stark effect). Lines terminate at classical threshold field, F_o (see text).

I.2 Separation of Hamiltonian in Parabolic Coordinates

If we neglect the effects of reduced mass and internal magnetic interactions (eg. fine structure), Schroedinger's equation for hydrogen in a static electric field is given in atomic units by [BET 57, sect. 51],

$$\left[-\tfrac{1}{2}\nabla^2 - \frac{1}{r} + Fz\right]\psi(\vec{r}) = W\,\psi(\vec{r}) \quad ,$$

where F, the field, is along the z axis. This equation is separable in parabolic coordinates (ξ, η, φ) where φ is the azimuthal angle about the z axis; the ξ and η coordinates are defined by $\xi = r + z$ and $\eta = r - z$ and can have values between 0 and $+\infty$. The surfaces ξ = const. and η = const. are paraboloids of revolution about the z axis with the focus located at the origin (see Fig. I.2-1). The volume element is $d\tau = (\xi + \eta)/4\, d\xi d\eta d\varphi$. We assume that the wavefunction has the form,

$$\psi(\vec{r}) = u_1(\xi)\, u_2(\eta)\, e^{im\varphi} \quad ,$$

and note that ∇^2 in parabolic cordinates is,

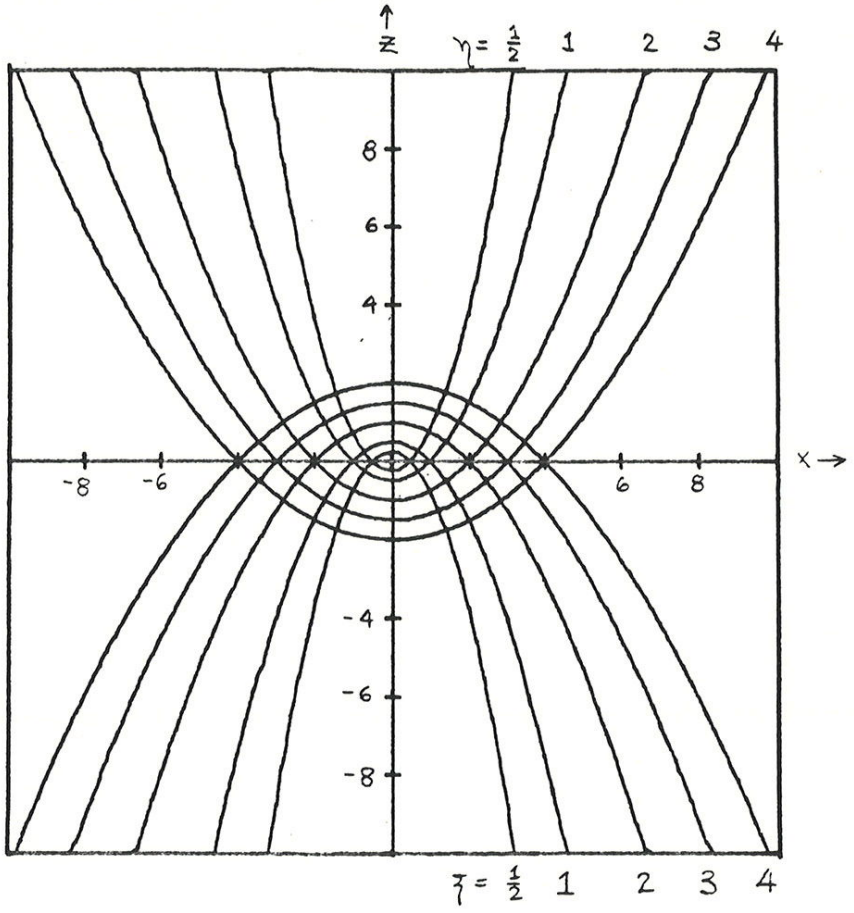

FIGURE I.2-1

Lines of constant ξ and η (as indicated) in the x - z plane.

$$\frac{4}{\xi+\eta}\frac{d}{d\xi}\left(\xi\frac{d}{d\xi}\right)+\frac{4}{\xi+\eta}\frac{d}{d\eta}\left(\eta\frac{d}{d\eta}\right)+\frac{1}{\xi\eta}\frac{d^2}{d\varphi^2}\,.$$

The functions $u_1(\xi)$ and $u_2(\eta)$ satisfy the following differential equations,

$$\left\{\frac{d}{d\xi}\left(\xi\frac{d}{d\xi}\right)+\frac{1}{2}W\xi-\frac{m^2}{4\xi}-\frac{1}{4}F\xi^2\right\}u_1(\xi)=-Z_1u_1(\xi)\qquad\text{(I.2-2a)}$$

$$\left\{\frac{d}{d\eta}\left(\eta\frac{d}{d\eta}\right)+\frac{1}{2}W\eta-\frac{m^2}{4\eta^2}+\frac{1}{4}F\eta^2\right\}u_2(\eta)=-Z_2u_2(\eta)\qquad\text{(I.2-2b)}.$$

Here Z_1 and Z_2 are separation parameters (or eigenvalues) which are subject to the conditon that $Z_1 + Z_2 = 1$. This requirement and the fact that both Z_1 and Z_2 depend upon W couples eqs. I.2-2a and I.2-2b.

The equation in φ is independent of the field and is identical to the familiar spherical equation. Thus m is a "good" quantum number for all values of the applied field. Note also that the +m and -m levels are degenerate, since only terms in m^2 appear in the ξ and η equations. This is reasonable, since the electric dipole interaction with the external field is not sensitive to the direction of electron

circulation.

To obtain additional quantum numbers we must first consider the zero field solutions. Here we expand $u_1(\xi)$ and $u_2(\eta)$ in a power series and obtain recursion relations for the coefficients under the condition that the total wavefunction is finite at the origin. As in the spherical case, where one must have positive integral values for the quantum number n, we find that the quantum numbers n_1 and n_2 associated with the ξ and η equations must also have positive integral values to ensure that the wavefunction is everywhere finite [BET 57, sect. 6]. These quantum numbers are related to the eigenvalues as follows,

$$n_1 = \frac{Z_1}{\sqrt{-2W}} - \tfrac{1}{2}(|m| + 1) \qquad (I.2\text{-}3a)$$

$$n_2 = \frac{Z_2}{\sqrt{-2W}} - \tfrac{1}{2}(|m| + 1) \qquad (I.2\text{-}3b) \quad .$$

Since $Z_1 + Z_2 = 1$, we can invert these equations to obtain,

$$W = -\frac{1}{2(n_1+n_2+|m|+1)^2} \quad .$$

This result can be compared with the energy relation in the spherical case,

$$W = -\frac{1}{2n^2} \quad .$$

We recognize the correspondence condition $n_1 + n_2 + |m| + 1 = n$. Here n is the familiar principle quantum number. n_1 and n_2 can have values between 0 and $n-|m|-1$ for a given n and $|m|$. Since m ranges from $-(n-1)$ to $+(n-1)$, we can easily verify that the total number of states for a given n is,

$$\sum_{m=-(n-1)}^{n-1} (n-|m|-1) = n^2$$

as required.

We now examine the problem when F is non-zero. It is helpful to rewrite eqs. I.2-2 in a form with no first derivatives. This is accomplished by introducing functions $f_1(\xi)$ and $f_2(\eta)$ defined by,

$$f_1(\xi) = \sqrt{\xi}\, u_1(\xi)$$

$$f_2(\eta) = \sqrt{\eta}\, u_2(\eta) \quad ,$$

that satisfy,

$$\left[\frac{d^2}{d\xi^2} - \Phi_1(\xi)\right] f_1(\xi) = 0 \qquad (I.2\text{-}4a)$$

$$\left[\frac{d^2}{d\eta^2} - \Phi_2(\eta)\right] f_2(\eta) = 0 \qquad (I.2\text{-}4b)$$

where,

$$\Phi_1(\xi) = -\frac{W}{2} - \frac{Z_1}{\xi} + \frac{(m^2-1)}{4\xi^2} + \frac{1}{4}F\xi \qquad (I.2\text{-}4c)$$

$$\Phi_2(\eta) = -\frac{W}{2} - \frac{Z_2}{\eta} + \frac{(m^2-1)}{4\eta^2} - \frac{1}{4}F\eta \qquad (I.2\text{-}4d) \quad .$$

The function Φ can be viewed as a one-dimensional potential well for a given energy and separation parameter. The wave-function oscillates when Φ is less than zero and is damped exponentially when Φ is greater than zero. Φ_1 and Φ_2 are

plotted in Fig. I.2-2 for various |m| values. For F>0 the negative energy ξ solutions always consist of bound states, and the η solutions correspond to tunneling or continuum states since the wavefunction oscillates for large η.

Because the Hamiltonian is Hermitian, we expect that the energy eigenvalues for the problem are real. The outer boundry condition for the η equation has been significantly changed from the zero field case, however, so that the eigenvalues are not discrete. (Note that the wavefunction, in this case, is not square integrable, and the large η solution corresponds to a linear superposition of ingoing and outgoing waves.) Even though W is continuous, the probabil-

FIGURE I.2-2

Typical potential energy functions, Φ_1 and Φ_2, for a tunneling state (see eq. I.2-4) [from HIR 71].

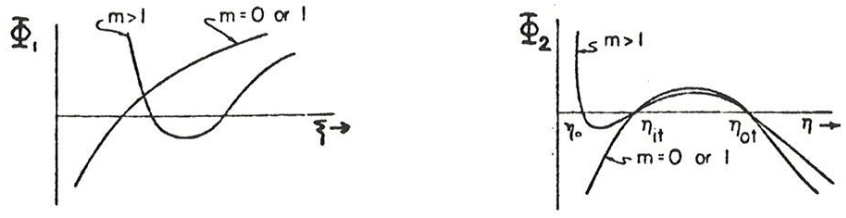

ity of finding the electron inside the surface defined by $\eta=\eta_{ot}$ (η_{ot} is the outer turning point) is large only when W is near specific energies, E_r. At F=0, these energies are equal to the zero field discrete eigenvalues. In practice, the dense band of continuum states near E_r cannot be distinguished from a bound states of energy E_r until the barrier separating the two oscillatory regions is small. An approximation which is often made when the barrier is large is to consider discrete solutions to the eigenvalue problem and to relax Hermiticity by adding an imaginary part to the energy such that the amplitude of the wavevector decreases exponentially in time. Physically this is equivalent to allowing only outgoing wave solutions to the η equation beyond $\eta=\eta_{ot}$. The conventional notation for the energies of these "quasi-stationary" states is,

$$W = E - \frac{i}{2}\Gamma \ ,$$

where E is a discrete eigenvalue and Γ is a decay rate which also characterizes the breadth of the levels [LAN 74, sect. 38]. Methods for calculating E and Γ, given F, are presented in the following sections.

I.3 Perturbation Results for E

To solve for the real energy eigenvalues, we follow the procedure outlined by Bethe and Salpeter [BET 57, sect. 51] and apply Rayleigh-Schroedinger perturbation theory separately to eqs. I.2-2a and I.2-2b to determine how the eigenvalues Z_1 and Z_2 are altered by the field. A perturbation expansion for Z_2 has been obtained in this manner by Herrick HER 76. The result to third order in the field is,

$$Z_2 = \sqrt{-2E}\left\{\tfrac{1}{2}(n+k) - \frac{x}{8}\left[3(n+k)^2 - m^2 + 1\right]\right.$$
$$- \frac{x^2}{32}(n+k)\left[17(n+k)^2 - 9m^2 + 19\right] \qquad \text{(I.3.1)}$$
$$\left. - \frac{x^3}{256}\left[375(n+k)^4 - 258m^2(n+k)^2 + 918(n+k)^2 + 11m^4 - 142m^2 + 131\right]\right\}$$

where $x = F/(-2E)^{3/2}$ and $k = n_2 - n_1$. The first term is the zero field expression for Z_2 (see eq. I.2-3b), the second term is the lowest order perturbation result, that is,

$$-\sqrt{-2E}\,\frac{x}{2}\left[3(n+k)^2 - m^2 + 1\right] = \int_0^\infty u_2^*(\eta)\left(-\tfrac{1}{4}F\eta^2\right)u_2(\eta)\,d\eta$$

where $u_2(\eta)$ is the solution to eq. I.2-2b for F=0, and so on. A similar expression for Z_1 is obtained by letting

$k \to -k$ and $x \to -x$. The condition that $Z_1 + Z_2 = 1$ (see sect. I.2) requires that,

$$E = -\frac{1}{2n^2} + \frac{3}{2} n(n_1 - n_2)F - \frac{1}{16} n^4 (17n^2 - 3k^2 - 9m^2 + 19)F^2$$

$$- \frac{3}{32} n^7 k (23n^2 - k^2 + 11m^2 + 39)F^3 \quad .$$

(Note that the states in the field are labelled by the zero field quantum numbers, n_1 and n_2.) The fourth order correction to the energy has been obtained using the WKB method [BEK 69; the corrected expression appears in HIR 71],

$$E^{(4)} = -\frac{n^{10}}{1024} \left[5487n^4 + 35182n^2 - 1134m^2k^2 + 1806n^2k^2 \right.$$

$$-3402n^2m^2 - 3093k^4 - 549m^4 + 5754k^2$$

$$\left. -8622m^2 + 16211 \right] F^4 .$$

should be $+147k^4$ according to: S P Alliluev & I.A. Malkin JETP 39, 627(1974) [see also H Silverstone]

The energies of all of the $|m| = 0$ and 1 levels for the $n = 12$, 13 and 14 manifolds, to fourth order in the field, are shown graphically in Fig. I.3-1.

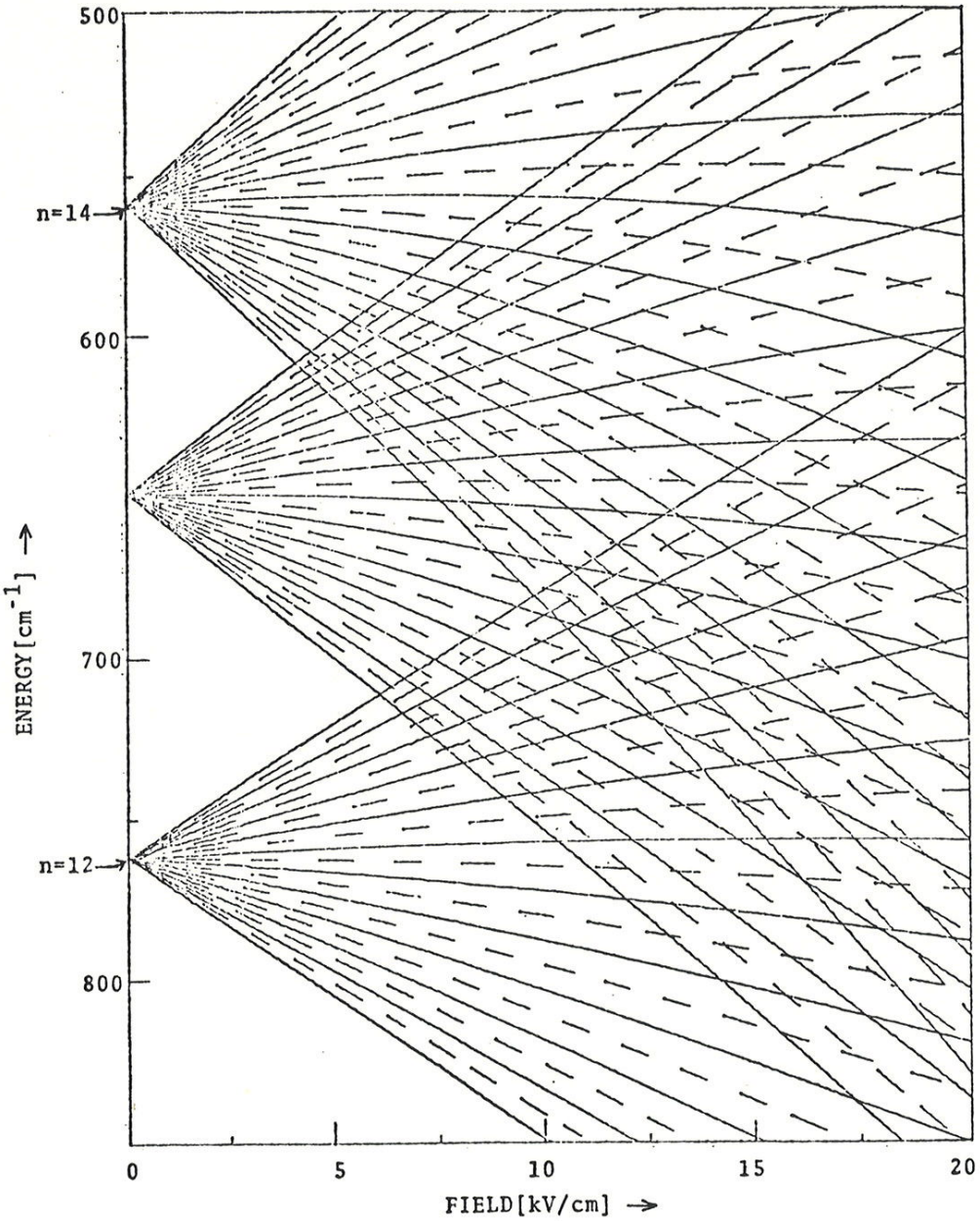

FIGURE I.3-1

Stark structure map of the n=12,13 and 14 levels according to fourth order perturbation theory. Energy is measured from the ionization limit. The solid lines correspond to the m=0 states and the dashed lines correspond to the |m|=1 states.

I.4 Field for "Classical" Ionization

Before discussing the quantum mechanical calculation for the ionization rate, Γ, it is instructive to examine the problem "classically" along the lines used in sect. I.1. We assume that the electron exists only where the kinetic energy is positive, that is when, $\bar{\Phi}_1$ and $\bar{\Phi}_2 < 0$ (see Fig. I.2-2). Ionization occurs for fields larger than the "classical" threshold field, F_{cl}. F_{cl} is defined as the field for which the two oscillatory regions in the η equation merge, or, in other words, when $\bar{\Phi}_2(\eta_{max.}) = 0$, where η_{max} is the local maximum. η_{max} satisfies the cubic equation,

$$\frac{d\bar{\Phi}_2(\eta)}{d\eta} = 0$$

and is given by,

$$\eta_{max} = 4\sqrt{\frac{Z_2}{3F}}\cos\frac{\theta}{3}$$

$$\cos\theta = \frac{(1-m^2)}{8F}\left[\frac{Z_2}{3F}\right]^{-3/2} .$$

Due to the complexity of the defining relations, graphical

or iterative methods must be used to find F_{cl} for a given state. In the special case where $|m| = 1$, the equations greatly simplify and one finds that,

$$\eta_{max} = 2\sqrt{Z_2/F}$$

so that,

$$\Phi_2(\eta_{max}) = \frac{E}{2} + \sqrt{Z_2 F} = 0$$

which may be re-written as the condition,

$$F_{cl} = \frac{E^2}{4 Z_2} .$$

We have solved for F_{cl} for the n=7, $|m|=1$ states using the third order perturbation results for E and Z_2 given in sect. I.3. The values are listed in Table I.4-1. For comparison, according to the naive analysis of sect. I.1, the critical field for n=7, assuming no Stark shift, is 134 kV/cm. The critical fields mark the boundaries between quasi-stationary regions (ie. tunneling solutions) and pure continuum regions, for given states. As a result, F_{cl} is useful for indicating when levels lie completely in the continuum.

n	n_1	n_2	m	$F_{c\ell}$ [kV/cm]
7	0	5	1	275
7	1	4	1	296
7	2	3	1	321
7	3	2	1	355
7	4	1	1	401
7	5	0	1	475

TABLE I.4-1

The classical threshold field for all $m=1$ sublevels of the n=7 term.

I.5 Tunneling Rate Calculations

It was shown in sect. I.1 that electrons can tunnel at fields below the "classical" threshold. No exact analytic solution to the tunneling problem has been obtained, so one must resort to approximate or numerical methods for calculating the tunneling rate. In this section we review the major approaches that have been applied.

Oppenheimer was the first to examine this problem in detail [OPE 28]. He calculated the ionization probability for the ground state in hydrogen by computing the transition probabilities between the unperturbed bound state (ie. no external field) and an unperturbed continuum state of the same energy in the applied field (ie. no Coulomb field) using Fermi's golden rule. To our knowledge this method has not been applied to excited states.

Lanczos used the WKB approximation to determine ionization rates for excited states [LAN 31]. He evaluated the WKB expression,

$$\Gamma = \frac{\exp\left\{-2\int_{\eta_{it}}^{\eta_{ot}} \sqrt{|\Phi_2(\eta)|}\, d\eta\right\}}{4\int_{\eta_o}^{\eta_{it}} [\Phi_2(\eta)]^{-\frac{1}{2}}\, d\eta} \quad ,$$

where $\Phi_2(\eta)$ is given by eq. I.2-4d. Using third order perturbation results for Z_1, Z_2 and E, the field value was determined where the tunneling rate was equal to the radiative decay rate for each of the extreme components of the n=5-8 manifolds. These field values agreed quite well with the experimental results of Traubenberg and colleagues [TRA 29,30,31], which are described in the next section.

Rice and Good (RG) used the WKB method to derive expressions for the ionization rates, energies and separation parameters [RIC 62]. This is in contrast to the Lanczos method, in which perturbation theory was used to obtain values for the last two quantities. The RG method is superior to the Lanczos method, since it allows for the possibility that ionization can affect the coupling between the ξ and η equations. Bailey, Hiskes, and Riviere (BHR) tabulated ionization rates for selected Stark states up to n=25 using the

RG method [BAI 65]. Their results are given in Fig. I.5-1. (The BHR tables, which are the standard references on ionization rates in hydrogen, have been widely used.) In addition BHR have calculated rates for all of the sublevels for the n=7 manifold using both the Lanczos and the RG methods. The results of these calculations are given in Figs. I.5-2a and I.5-2b.

A semi-analytic approach has been used by Smirnov and Chibisov (SC) to obtain an expression for the ionization rate [SMI 66]. This expression was derived by omitting certain small terms in the η equation (see eq. I.2-2b) and using the WKB approximation to obtain,

$$\Gamma = \frac{(-2E)^{3/2}\left[\frac{4(-2E)^{3/2}}{F}\right]^{2n_2+|m|+1}}{n_2!\,(n_2+|m|)!}\exp\left\{-\frac{2}{3}\frac{(-2E)^{3/2}}{F}\right\}$$

(corrected by Koch [KOC 74, p.35]). This expression is applicable when $F << 2E^2/x$ where $x = \max(Z_1, Z_2)$. The fourth order perturbation results for E are used to obtain the ionization rates for the n=7 levels, which are given in

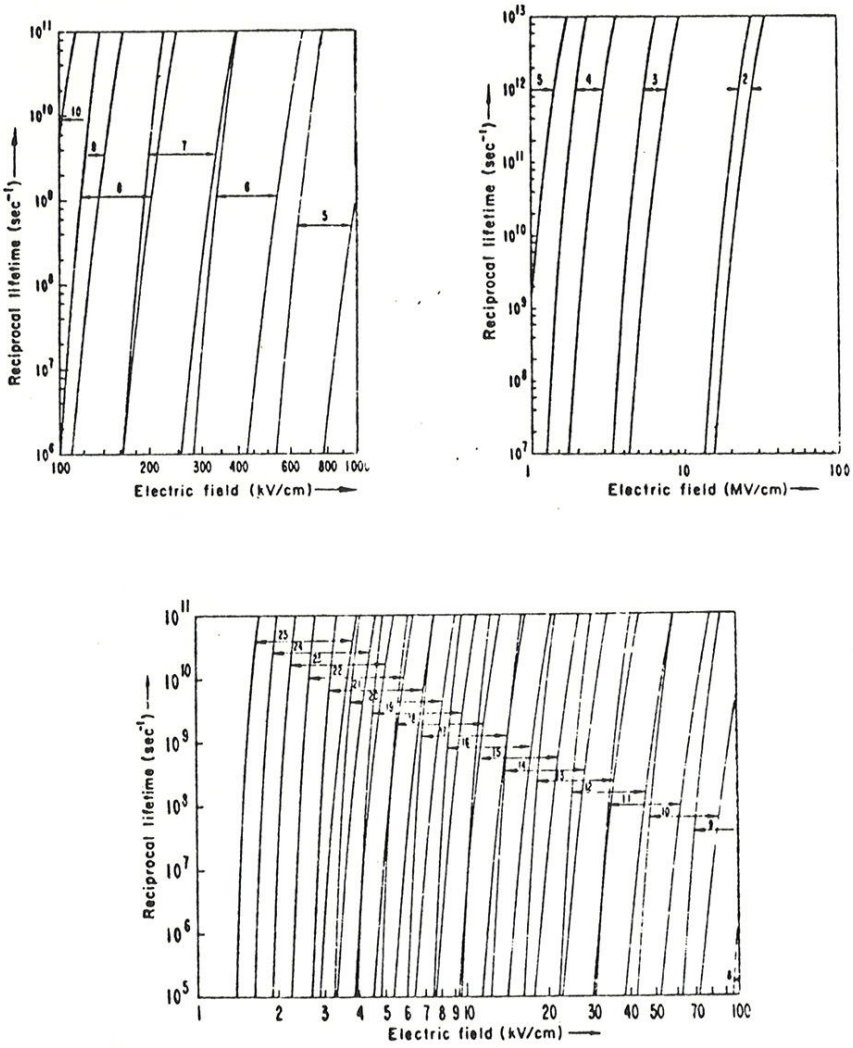

FIGURE I.5-1

Ionization probabilities versus electric field for the extreme components of levels n=2-25, by the RG method.

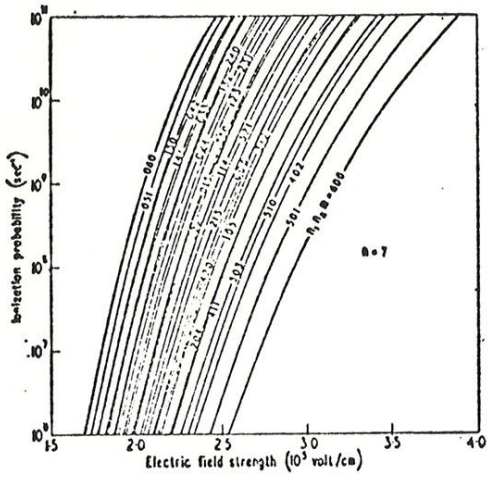

(a)

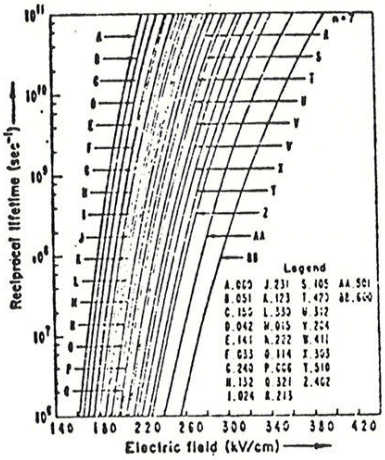

(b)

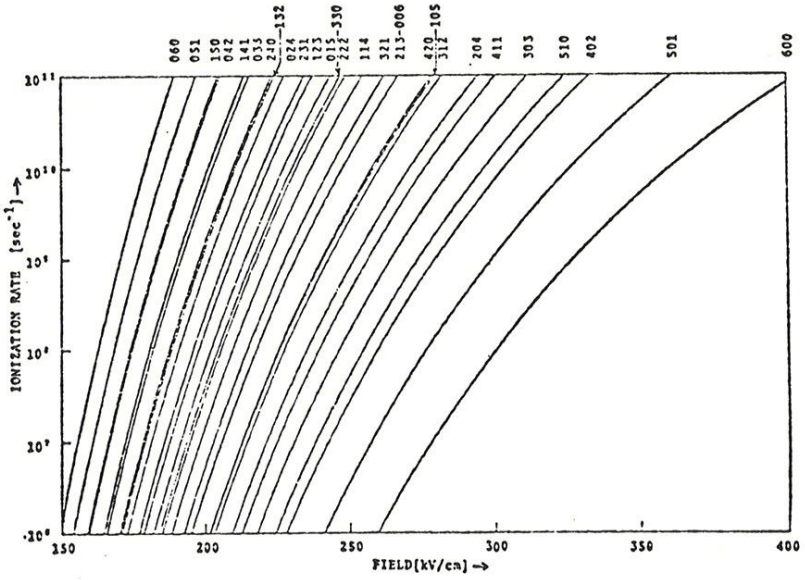

(c)

FIGURE I.5-2

Ionization probabilities versus electric field for the different Stark states n n m belonging to the n=7 level:

(a) by the Lanczos method in third order [from BAI 65];

(b) by the RG method [from BAI 65];

(c) by the SC method in fourth order.

Fig. I.5-2c. The SC results exhibit the same trends as the rates calculated by the RG and Lanczos methods, and agreement is generally good.

Alexander used a numerical iterative procedure to solve the coupled equations for the ground state of hydrogen in a static field [ALE 69]. For a given E, he examined the coefficients of the power series for the function $f_1(\bar{\eta})$ (see sect. I.2). The condition that f_1 is zero at $\bar{\eta} = \infty$ allows one to set an upper and lower bound on the value of Z_1. The η equation was then solved using the WKB form for $f_2(\eta)$,

$$f_2(\eta) \propto \frac{1}{\Phi_2(\eta)} \cos\left[\int_{\eta_{ot}}^{\eta} \sqrt{|\Phi_2(\eta')|}\, d\eta' - \tfrac{1}{4}\pi + \delta(E) \right],$$

and it was observed that δ was essentially constant, except near specific values of E, where it changed by π. This is similar to the scattering case where a change of π in the phase shift indicates the location of a bound state. The analogy to the scattering case was applied further to determine the resonance width (ionization rate) by using the Breit-Wigner expression,

$$\Gamma = \left[\frac{1}{2} \frac{d\delta(E)}{dE} \Big|_{E=E_r} \right].$$

Hirshfelder and Curtiss (HC) [HIR 71] used Alexander's method to solve for Z_1, given E and F, and solved the equation numerically using the Numerov method [HAM 62, p.165] to determine the exact wavefunction, $f_2(\eta)$ (see sect. I.2). By examining the amplitude of the outgoing wave at the outer turning point, η_{ot}, they were able to determine the ionization rate. It was found that at the resonance energy the wavefunction had a node at η_{ot}. HC calculated the rate of ionization for the ($n=5$, $n_1=3$, $n_2=0$, $|m|=1$) state as a function of field. The results are given in Fig. I.5-3. Both the RG method results (calculated by BHR) and the classical threshold results are given for comparison. As one might expect, the HC results agree with those of RG except at large Γ, since the WKB approximation is not valid when the barrier is small. Recently, Guschina and Nikulin (GN) calculated rates for the same level using virtually the same procedure [GUS 75]. Their results are also plotted in Fig. I.5-3. The agreement between the GN and HC methods is poor for large fields, and no explanation is given for this

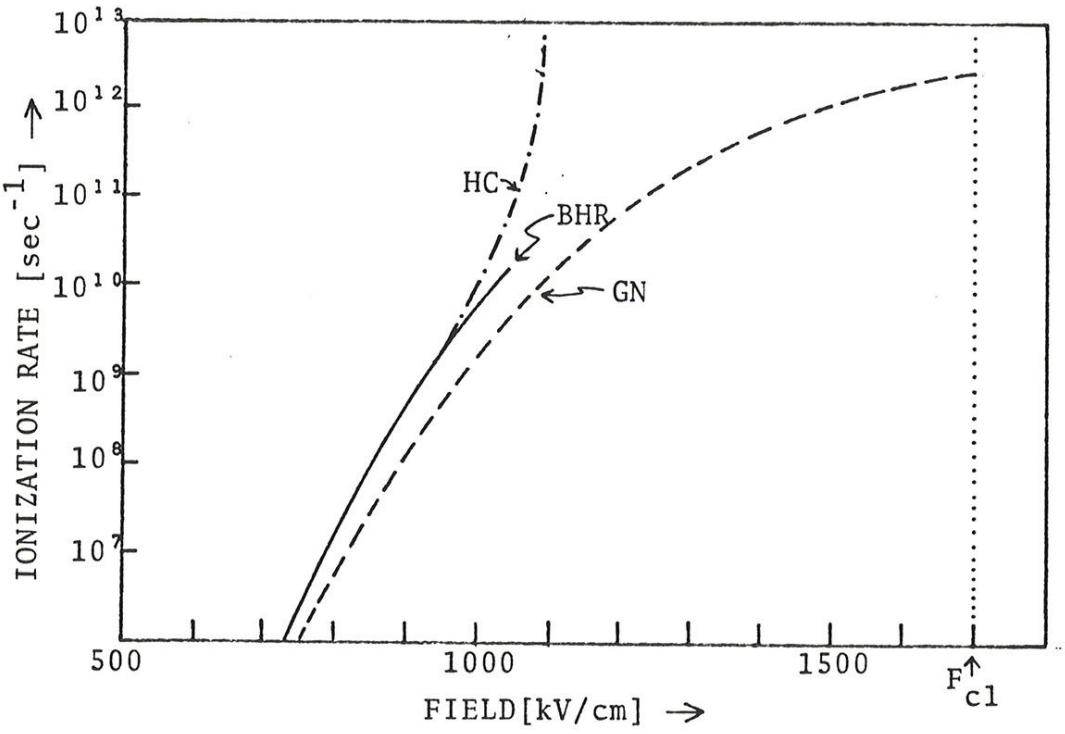

FIGURE I.5-3

Ionization rate versus field for the n=5, n_1=3, n_2=0, |m|=1 state according to the methods of BHR, GN, and HC. The classical threshold field, obtained by the method that is described in sect. I.4, is indicated by the dotted line.

in their paper. (In GUS 75 the calculation for the (5,3,0,1) level is incorrectly compared with the BHR tabulation for the (5,4,0,0) level.)

For the sake of completeness we note two recent calculations for the ionization rate of the ground state of hydrogen and a recent calculation of the order in which various Stark sublevels ionize as the field increases. For the ground state ionization determination, Larsen [LAR 76] used a method based upon Oppenheimer's procedure, and Hehenberger [HEH 74] used a method based upon Weyl's theory for solving Sturm-Liouville problems with continuous eigenvalues. It remains to be shown that either of these methods is applicable to excited states. For excited states, Herrick [HER 76] has used Catastrophe theory to determine the order in which various sublevels of a given manifold ionize, and has obtained reasonable agreement with the BHR results.

We have presented a survey of methods that have been used to calculate the ionization rates for excited states of hydrogen in a static electric field. The list is rather long, and the methods which have been used are quite varied.

The numerical approach of HC is the only one which gives exact results. Unfortunately, this approach is difficult to apply to highly excited states. Thus we will compare our experimental results for the ionization rates of hydrogenic Stark states in sodium with the BHR calcuations (RG method) for Γ.

I.6 Review of Field Ionization Experiments

Perhaps the earliest and certainly one of the most elegant experiments on field ionization was performed by Traubenberg and colleagues, who observed the effect of spontaneous ionization on the Balmer emission spectrum of hydrogen [TRA 29,30,31]. They used a discharge lamp with an internal field that varied monotonically with position, decreasing from a value of 1.1 MV/cm at one end of the lamp to nearly zero at the other end. The resonance fluorescence was imaged on the slits of an optical spectrometer and a photograph of the spectrum was taken. The photographic plate is reproduced in Fig. I.6-1. The various groups of lines cor-

FIGURE I.6-1

Stark effect on some of the Balmer lines. The electric field strength increases from the bottom of the picture upwards. The maximum field value (a little below the top of the picture) is 1.14 MV/cm. The horizontal white lines are lines of constant field strength [from BET 57].

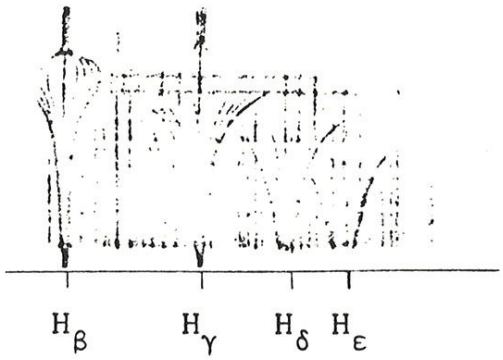

respond to transitions from the n=4-7 states to the common n=2 state for increasing field values. The abrupt end to some of the lines indicates where spontaneous ionization competes with radiation as a means for depopulating levels. Perhaps the most striking feature of the data is the fact that the components which are furthest from the ionization limit for a given n disappear first as the field increases. Note that at these values of n, the levels ionize before they cross with states from adjacent manifolds. (According to the BHR results, states having n>9cross before the ionization rate exceeds the radiative decay rate.) Unfortunately this spectroscopic method gives no information when ionization rates are large, in which case radiative decay is negligable.

An important advance was made by Riviere, who suggested using ion detection to measure the ionization rate directly [RIV 63]. This method consists of creating excited state hydrogen atoms by charge exchange in a fast proton beam, subjecting the excited atoms to an external field, and monitoring the production of ions. For experimental convenience the derivative of the signal with respect to field is measured using lock-in detection to minimize noise. Data obta-

ined using this method is shown in Fig. I.6-2. When a wide distribution of sublevels of a given term are present, the signal which results appears as a bell-shaped curve as a function of the field. Unfortunately, the charge exchange excitation method excites all sublevels for many n values which results in overlapping ionization curves at large n. To compare this data with theory one must sum the contributions to ionization from all of the populated levels and must assume some distribution of states. This makes detailed testing of ionization rate calculations exceedingly difficult. The reader is referred to two excellent review articles by Il'in and Riviere for a more extensive survey of these fast beam methods [ILI 73 and RIV 68].

Spectroscopic studies of ionization have been made and qualitative agreement between theory and experiment has been obtained for the lower n manifolds. A detailed comparison between theory and experiment has been difficult for higher states, since the only information about ionization has come from fast beam experiments in which many terms contribute to the net ionization signal.

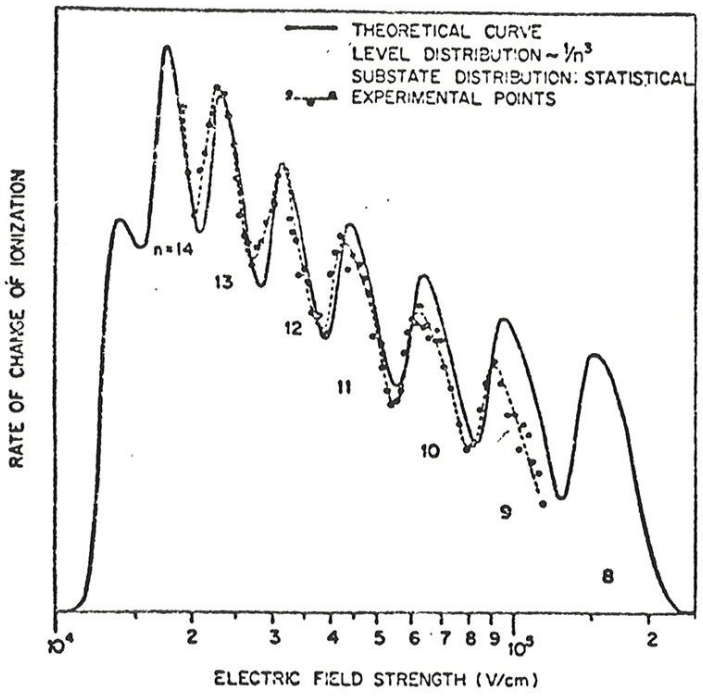

FIGURE I.6-2

Comparison of the calculated differential ionization rates with experimental results [from RIV 63]. The relative population of the levels was assumed to vary as n^{-3} and the calculated curve has been normalized in amplitude to agree with the experimental points at n=12 [from KOC 74].

CHAPTER II

DISCUSSION OF ENERGY LEVEL STRUCTURE AND EXCITATION OF SODIUM

II.1 Introduction

The best atom to use for testing hydrogenic tunneling theory is hydrogen. Unfortunately, however, hydrogen cannot be excited to selected high Rydberg states by visible lasers since the principle transition ($1s \rightarrow 2p$) is in the vacuum ultraviolet. Alkali atoms provide the next best choice because they are, for many purposes, similar to hydrogen. Alkalis consist of a nucleus of Z protons surrounded by a core of Z-1 electrons and a single valence electron. The core electrons form a closed shell rare gas configuration, with zero total angular momentum and a spherically symmetric charge distribution. Outside the core the potential is, to a good approximation, Coulombic. For high angular momentum states the electron does not appreciably penetrate the core, so that many physical observables such as the binding energy and the fine structure splitting are nearly identical with those of hydrogen.

Sodium was chosen for this study because it is a light alkali with a relatively small core (10 electrons in a 1s(2)2s(2)2p(6) configuration) and consequently is more hydrogenic than the heavier alkalis. Also, Rydberg states of this alkali can be populated readily by using tunable lasers. In the next section we examine the energy levels of sodium in the absense of external perturbations. For completeness we include the effects of the fine and hyperfine interactions, although they play no significant role in this work. In the following section the effect of an external electric field on the level structure of the Rydberg states is calculated. Finally, in the fourth section we consider the selection rules for excitation of Stark levels for various laser polarizations.

II.2 Sodium Energy Level Structure -- Zero Field Case

The energy level diagram of the observed levels for sodium is given in Fig. II.2-1. Angular momentum increases to the right [MOO 49]. Hydrogen term energies are included for comparison.

Traditionally the energies of the states are expressed in the hydrogen-like form,

$$E_{n\ell} = -\frac{1}{2(n-\delta_\ell)^2} \qquad (II.2-1),$$

where δ_ℓ is called the quantum defect. δ_ℓ is essentially independent of n and decreases with increasing l. Evidence of this is shown in Fig. II.2-2 for several alkali atoms (for sodium, $\delta_0 = 1.35$, $\delta_1 = 0.85$, and $\delta_2 = 0.014$). The fact that the quantum defect is non-zero and independent of n has been qualitatively explained by Parsons and Weisskopf by assuming that the core is impenetrable, so that the wavefunction is zero at the core surface (ie. $r=r_c$) PAR 67. For $r>r_c$ the potentials of sodium and hydrogen are the same. The core radius of a given alkali is determined by requiring that

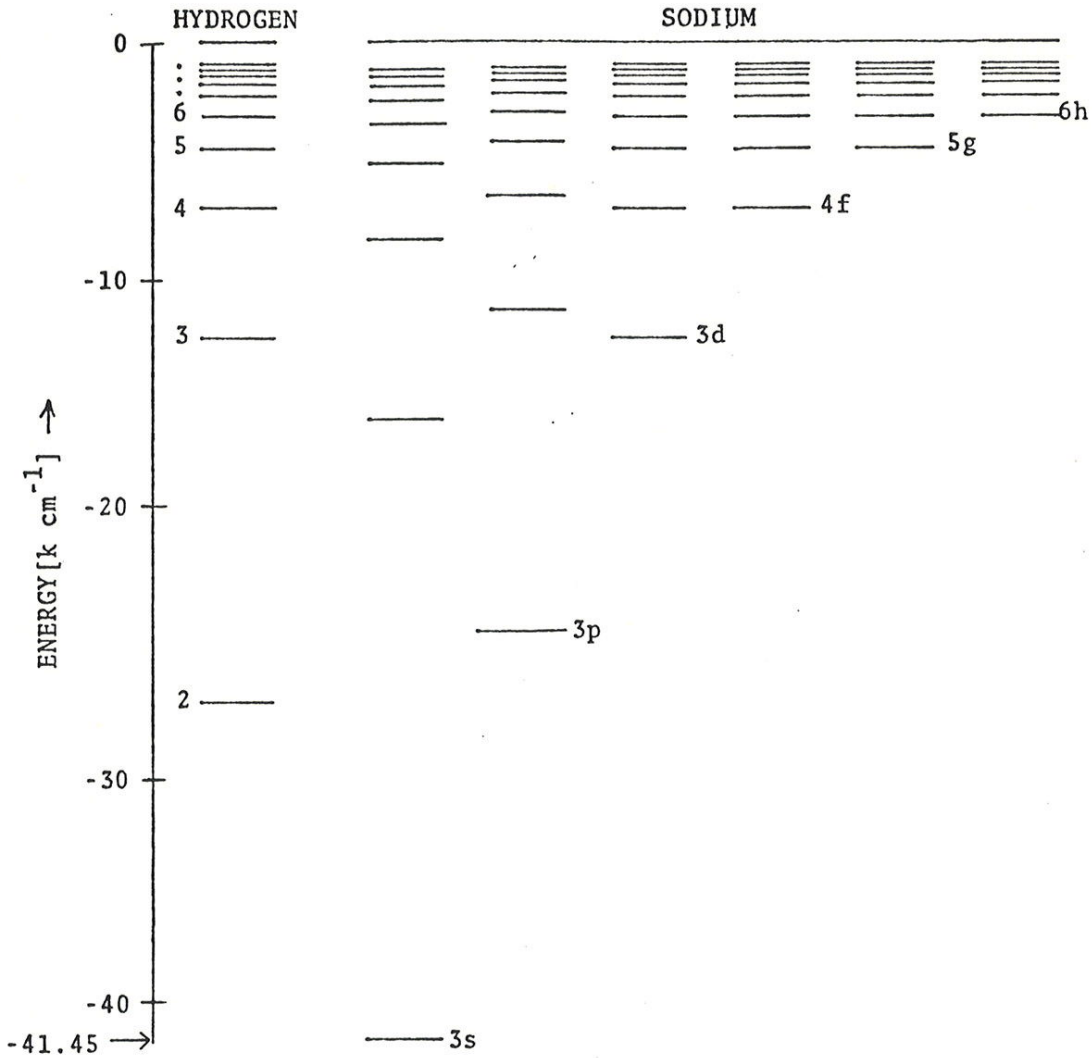

FIGURE II.2-1

Energy level diagram for sodium. At left, hydrogen energies are shown. The zero of energy is the one elctron ionization limit.

(a)

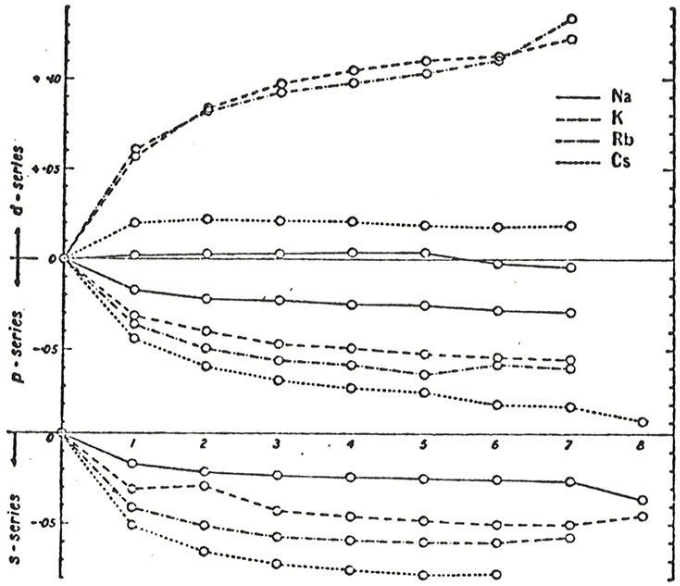

(b)

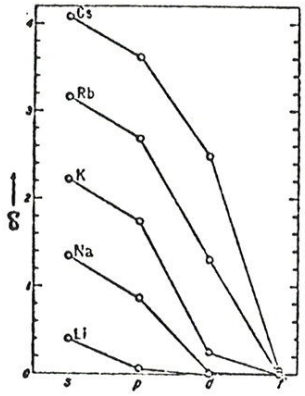

FIGURE II.2-2

(a) Variation with n of the quantum defect δ in alkali spectra. The difference between the quantum defect of each term and that of the lowest term of the series to which it belongs is plotted against the difference between the total quantum numbers of these terms [from CON 70].

(b) Variation with l of the quantum defect δ for alkali atoms [from CON 70].

the theoretical ground state energy match the observed energy. (For sodium this radius is 0.91 bohr.) The condition that the wavefunction be zero at $r=r_c$ is easy to justify since the classical velocity of the electron ($v=\sqrt{2(E-V(r))}$) is large when it is inside of the core. (Here V(r) is the effective (shielded) nuclear Coulomb potential.) The fact that little time is spent at $r<r_c$ is reflected in the small amplitude of the atomic wavefunction. Good agreement has been obtained between quantum defects calculated according to this model and observed values for all of the alkalis.

For $l \geq 3$, the energies of sodium are virtually indistinguishable from those of hydrogen. This is expected since these states do not penetrate the core appreciably. There is, however, a slight deviation from the hydrogenic energies, largely due to the induced polarization interaction between the valence electron and the core [FRE 76]. According to Freeman and Kleppner the quantum defects due to the polarization energy for the high l states are less than 0.005.

Assuming δ_l can be treated as a constant, we can con-

struct a universal local energy level diagram (Fig. II.2-3) which is applicable for large n. The unit of energy in this diagram is the hydrogen term separation,

$$\Delta_o(n) = -\frac{1}{2n^2} - \left(-\frac{1}{2(n-1)^2}\right) \approx \frac{1}{n^3} .$$

The difference between the energy of a sodium level of given n and l, and the hydrogenic energy of the same n is,

$$E_n(H) - E_{nl}(Na) = -\frac{1}{2n^2} - \left(-\frac{1}{2(n-\delta_l)^2}\right) \approx \frac{\delta_l}{n^3} ,$$

so that in units of $\Delta_o(n)$, the sodium level lies below the hydrogen level by an amount δ_l.

Fine and Hyperfine Structure

For the most part fine structure arises from the interaction between the magnetic dipole moment of the electron ($\vec{\mu} = g_s \mu_o \vec{S}$) and the magnetic field induced by its orbital motion [CON 70, sect. 5.4]. The interaction energy is proportional to $\vec{L} \cdot \vec{S}$, where $\vec{L}$ is the orbital angular momentum and $\vec{S}$ is the spin angular momentum. Each state with $l > 0$ is

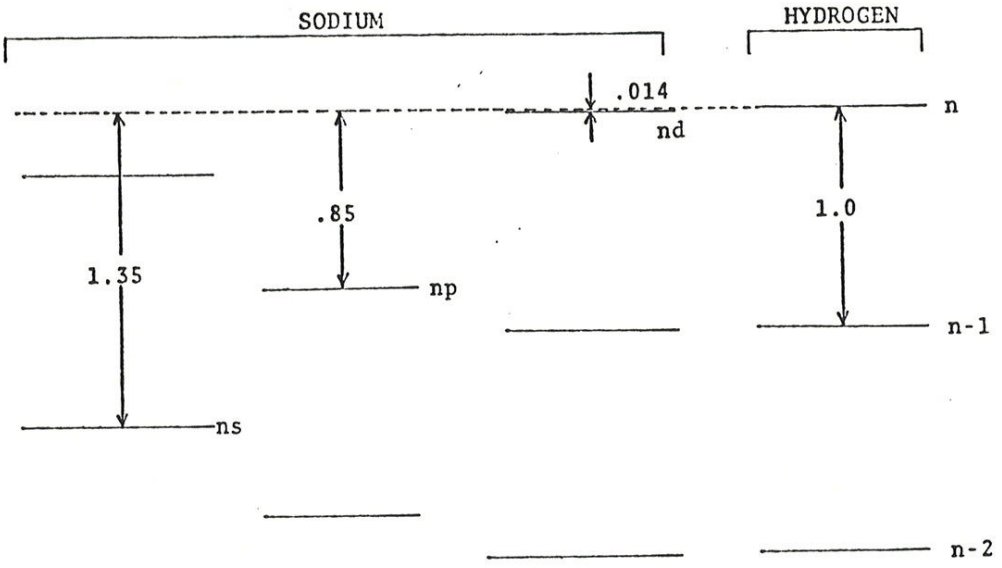

FIGURE II.2-3

Local energy level diagram for the l=0,1 and 2 states in sodium. The unit of energy is taken to be the hydrogen term separation which is shown at right.

split into a doublet with a splitting given by $\Delta E_{fs}(nl)$.

Hyperfine structure is mainly due to the interaction of the nuclear dipole moment ($\vec{\mu}_I = g_I \mu_0 \frac{m}{M} \vec{I}$) and the magnetic field produced by the valence electron [KOP 58, sect. 26]. The interaction energy has the form $a_{nlj}\ \vec{I}\cdot\vec{J}$, where $\vec{I}$ is the nuclear spin angular momentum and $\vec{J}$ is the total electronic angular momentum (i=3/2 for sodium). States having j=1/2 are split into two components, and levels with $j > 1/2$ are split into four components. Both a_{nlj} and the leading term to ΔE_{fs} are proportional to $\langle r^{-3} \rangle$, so that to a first approximation the fine and hyperfine splittings are proportional to one another [RAM69, p.75]. We shall later use this fact to infer the size of a_{nlj} for states where no hyperfine measurements have been made.

For low l states a semi-classical approach has been used with moderate success to determine ΔE_{fs} and a_{nlj} [GOU 33]. According to Goudsmit, both quantities scale as $(n-\delta_l)^{-3}$. To illustrate the scaling law we list ΔE_{fs} for numerous levels in sodium in Table II.2-1. Data on the hyperfine splittings of the sodium states is somewhat sparse

since the size of the hyperfine interaction is generally so small. The ground state hyperfine separation has been accurately measured using atomic beam techniques. The two components are separated by 1772 MHz [RAM 69, p.255]. (The separations between the four components of the $3^2P_{3/2}$ state have been measured by level crossing techniques and have values 60, 40 and 20 MHz.)

For large l (ie. $l \gg 3$), the fine structure splitting for sodium has been observed to be the same as for hydrogen [GAL 76a, LIA 76] and is given by the following expression to order α^2 [BET 57, sect. 17.2],

TABLE II.2-1

Fine structure separations of p and d states in sodium.

	ΔE_{fs}(np) [cm^{-1}]		ΔE_{fs}(nd) [MHz]		
n	xl	$x(n-0.85)^3$	xl	$x(n-0.014)^3$	
3	17.20[1]	171	-1482(5)[2]	-39400	references:
4	5.63[1]	176	-1025(6)[3]	-64900	1. [MOO 49]
5	2.52[1]	180	-690(50)[2]	-85500	2. [MEI 37]
6	1.25[1]	171	-372(50)[2]	-79800	3. [PRI 74]
7	0.74[1]	172			4. [HAR 74]
8	0.47[1]	172			5. [HIL 76]
9			-124.5(15)[4]	-90300	
10			-91.5(10)[4]	-91100	
11			-71.6(13)[5]	-95000	
12			-54.0(14)[5]	-93000	
13			-44.0(12)[5]	-96300	
14			-34.9(5)[5]	-95500	
15			-26.1(10)[5]	-87800	

$$\Delta E_{fs} = \frac{\alpha^2}{2n^3}\left(\frac{3}{4n} - \frac{1}{j+\frac{1}{2}}\right).$$

No measurements of the hyperfine structure have been made for these high l states. However, because of the relationship between the fine and hyperfine structure, we are fairly safe in assuming that a_{nlj} is given by the hydrogenic expression,

$$a_{nlj} = \frac{\alpha}{2n^3(l+\frac{1}{2})j(j+1)} \frac{m}{M} g_I$$

We see from this equation that the hyperfine splittings are smaller than the fine structure splittings by an amount on the order of $\mu_o/\mu_I \approx 800$, where μ_I is the sodium nuclear moment.

Radiative Lifetimes

Lifetimes (τ) of the low l states in sodium for $n<14$ have recently been measured by Gallagher and colleagues [GAL 75,76d]. Their results are listed in Table II.2-2. Within experimental error, τ is found to scale as n^{-3}, which is

expected according to quantum defect theory. The lifetimes of the low l states in sodium are larger than the corresponding hydrogen values, since ω^3 for the sodium principle transitions is smaller. For states with large l we expect that the decay rates are the same for sodium as for hydrogen. The hydrogen decay rates have been tabulated by Green et al [GRE 57].

TABLE II.2-2

Radiative lifetimes of s, p and d states in sodium.

	Lifetimes [nsec]		
n	τ(ns)	τ(np)	τ(nd)
3		16.1	
4		125(12)	
5		345(43)	120(14)
6		890(90)	206(24)
7	276(14)	1450(100)	324(32)
8	465(40)		502(39)
9	713(76)		720(67)
10	1024(49)		971(35)
11	1270(130)		
12			1650(150)
13	2270(170)		2120(400)

II.3 Stark Structure of Sodium

Here we consider the effect of an external electric field on the Rydberg states of sodium. For the moment we ignore the fine and hyperfine interactions.

Unlike the hydrogen case discussed in chapter I, the sodium Stark problem does not separate in parabolic coordinates, because the potential is not Coulombic. (The condition for separability is that $r \cdot V(r)$ can be expressed as a function of ξ plus a function of η .) The azimuthal part of the Hamiltonian separates, as before, so that m is a "good" quantum number in the field.

To determine the energy eigenvalues we have chosen to diagonalize the Hamiltonian matrix using zero field sodium wavefunctions in a spherical representation. The total Hamilitonian is,

$$\mathcal{H} = \mathcal{H}_o + Fz$$

$$\mathcal{H}_o |n\ell m\rangle = E_{n\ell} |n\ell m\rangle .$$

here $\mathcal{H}_o$ is the zero field sodium Hamiltonian, $|n\ell m\rangle$ are its eigenfunctions, and $E_{n\ell}$ are the eigenvalues which are known (see eq. II.2-1). To construct the energy matrix we must evaluate the matrix elements,

$$\langle n\ell m| \mathcal{H} |n'\ell'm'\rangle = \langle n\ell m|\mathcal{H}_o|n'\ell'm'\rangle + \langle n\ell m| Fz |n'\ell'm'\rangle .$$

The first term is diagonal and has the value $E_{n\ell}\delta_{nn'}\delta_{\ell\ell'}\delta_{mm'}$. The second term is off-diagonal in l because z is an odd function which can only couple states of different parity. Fortunately, many of the off-diagonal z matrix elements are not present due to the fact that the angular integration over $z = r\cos\theta$ gives zero for all cases except when $m=m'$ and $l=l'\pm 1$. The condition on m is especially helpful because it means that one can diagonalize each $|m|$ case separately. Thus the dimensionality of our matrix increases only by $n - |m|$ for each n manifold we wish to include, instead of by n^2 as it would in the general case.

To calcuate the non-zero matrix elements, we use a procedure derived by Zimmerman (see appendix A). The method determines the wavefunction for the known energy by expanding the Coulombic wavefunction in a power series which satisfies the outer boundary condition. The wavefunction is only valid for $r > r_c$. Fortunately the major contribution to $\langle nlm|z|n'l'm'\rangle$ is at large r, where the method is most applicable. (Conversly, one would not expect the matrix element of $\langle r^{-q}\rangle$ for $q>0$ to be accurate, since this quantity depends strongly on the behaviour of the wavefunction near the origin.) Zimmerman's method is similar to the Bates-Damgaard technique [BAT 49], which has been widely used for alkalis. For states having l and $l' \geq 3$ the dipole matrix elements were evaluated by letting E_{nl} equal the hydrogen energy in Zimmerman's procedure. The low l dipole matrix elements for sodium obtained with this method are significantly different from those for hydrogen (see Table II.3-1).

To diagonalize the energy matrix the familiar Jacobi method was used to obtain eigenvalues and eigenvectors [NEU 62, chap. 7]. The largest square matrix that we could diagonalize on our laboratory computer was 75 x 75, which set a

	10p	10d	10f	11s	11p	11d	11f	12s	12p	12d	12f
10s	149. (91.)				40. (-12.)				-15. (5.)		
10p	147. (63.)			31. (92.)		46. (-19.)		-11. (-14.)		-17. (10.)	
10d	143. (143.)			27. (140.)		51. (49.)		-10. (7.)		-13. (-13.)	
10f				23. (25.)					-8. (-9.)		
11s	181. (113.)				48. (-15)						
11p	178. (75.)			38. (114.)		54. (-23.)					
11d	175. (175.)			33. (171.)		60. (57.)					
11f	29. (31.)										
12s	215. (136.)										
12p	213. (89.)										
12d	209. (209.)										

TABLE II.3-1

Radial matrix elements between various low l states in hydrogen and sodium. The values for hydrogen appear above those for sodium in each box. All quantities are in atomic units (bohrs).

limit to the number of manifolds which could be included. For example, if one were interested in the $|m|=0$ case near n=15 then the largest number of nearby terms that could be considered would be four, namely, two manifolds above and two below (ie. 13+14+15+16+17=75).

Results of the diagonalization for the $|m| = 0$, 1 and 2 cases for sodium near n = 15 are given in Fig. II.3-1. For comparison the hydrogen results for these same states are also presented. (On this scale and for the levels shown, there was no observable difference between the hydrogen diagonalization and the fourth order perturbation results.) The diagonalization was carried out in steps of 250 V/cm; the curves in the field region between calculations were generated by interpolation. The linear Stark shifts exhibited by the bulk of the levels is the familiar effect that one observes for degenerate systems or for cases when Stark perturbations are large compared with the zero field separations. In sodium, the s and p states are not degenerate in low field and display a second order Stark shift. The $|m| = 0$ and 1 cases in sodium exhibit large repulsions between states of the same $|m|$, whereas the hydrogen states appear to cross. The higher $|m|$ states in sodium rapidly approach hy-

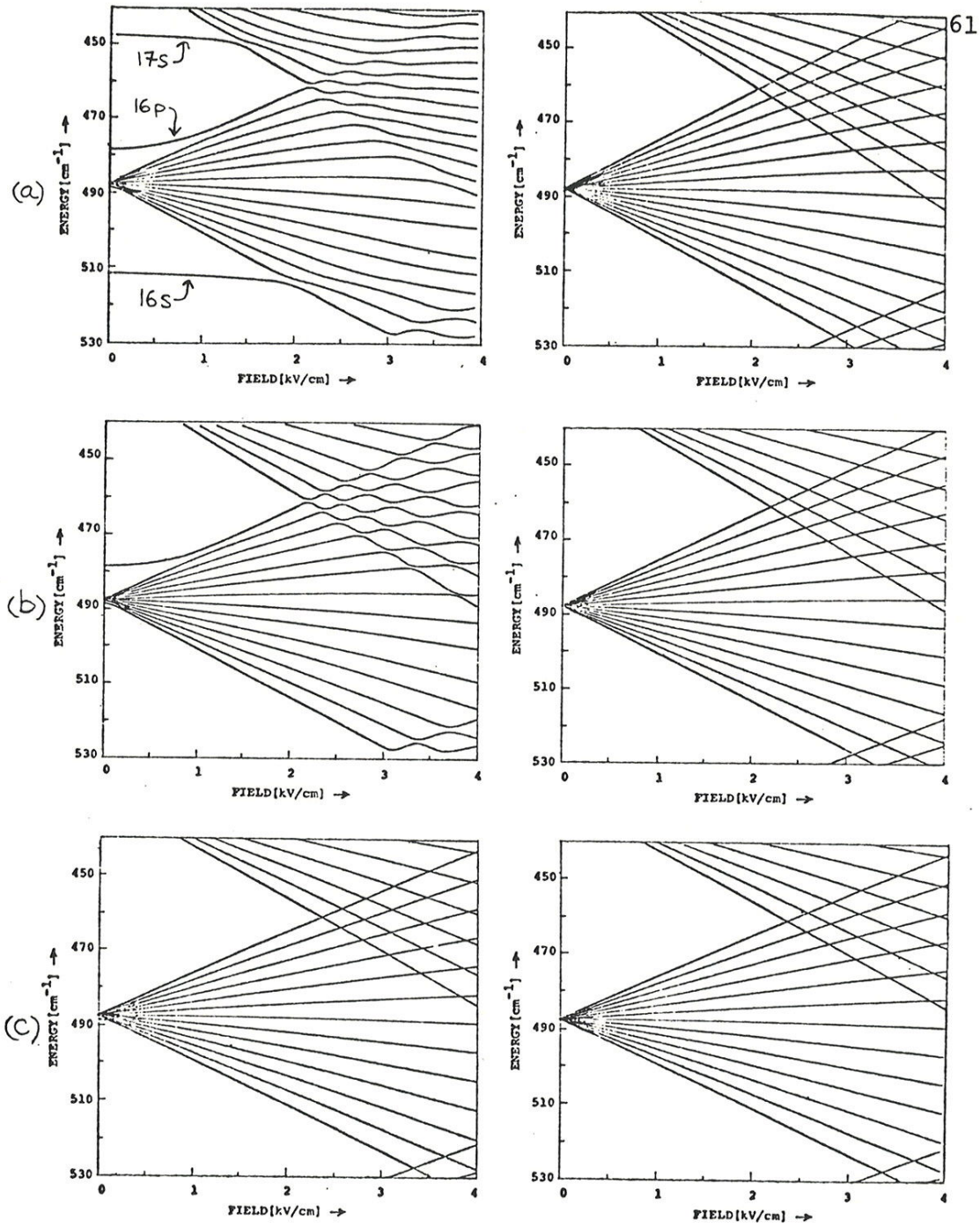

FIGURE II.3-1

Energy diagonalization results for Stark states near n=15 in sodium and hydrogen.

(a) the m=0 case

(b) the m=1 case

(c) the m=2 case

drogenic behaviour making them good candidates for testing hydrogenic tunneling theory.

Fine and Hyperfine Structure

Now we consider the effect of the fine and hyperfine interaction on the sodium Stark structure. These terms, proportional to $\vec{L}\cdot\vec{S}$ and $\vec{I}\cdot\vec{J}$ respectively, can be expressed in terms of raising and lowering operators,

$$\vec{L}\cdot\vec{S} = L_z S_z + \tfrac{1}{2}(L_+ S_- + L_- S_+)$$

$$\vec{I}\cdot\vec{J} = I_z(L_z + S_z) + \tfrac{1}{2}(I_+(S_- + L_-) + I_-(S_+ + L_+)) \quad ,$$

where $L_z|n\ell m\rangle = m|n\ell m\rangle$ & $L_\pm|n\ell m\rangle = \sqrt{(\ell \mp m)(\ell \pm m + 1)}\,|n\ell\, m\pm 1\rangle$, etc. Since the hyperfine interaction is so much smaller than the fine structure, we shall ignore it for the present. Because s = 1/2, the total number of states has doubled. The "z" projection operators do not change either m_s or m so that they appear on the diagonal of the energy matrix. The size of this term is determined by the overall coefficient

of $\vec{L}\cdot\vec{S}$, b(nl), which is largest for the p states. For example, the diagonal term corresponding to the 12p state is 0.0833 cm^{-1} where we have taken b(12p) to be 0.166 cm^{-1}. The two different spin states are shifted in opposite directions. The raising and lowering terms couple states of different m and m_s (same l and s), which means that we can no longer diagonalize each m case separately. The size of the terms off-diagonal in m and m_s are also determined by b(nl), which for all of the states near n=12 are less than 0.166 cm^{-1}. One effect of the fine structure term is to remove the degeneracy between the +m and -m states by an amount proportional to b(nl). Another effect is that levels of different m anticross due to the coupling between the m and m $\pm$ 1 manifolds, but the size of the level repulsion, which is twice the coupling matrix element (see appendix E), is small. Since the energy shifts and splittings are so much smaller than the Stark shifts of the levels, we are justified in ignoring them in the first stages of the analysis. As we shall see later, however, a minute amount of level mixing can have a significant effect on the ionization behaviour of levels, and therefore these terms must be included in a thorough treatment of ionization.

The Earth's magnetic field also affects the level structure. The interaction energy is $-\vec{\mu}\cdot\vec{H}$, so that the size of the interaction is roughly equal to $\mu_o H$. For a field of 1 gauss, $\mu_o H = 10^{-4}$ cm^{-1}, which is negligable compared with the fine structure energy, and so may be ignored.

II.4 Optical Excitation of Sodium Rydberg States

In the work that follows Rydberg states are excited stepwise in a static electric field ($F < 50$ kV/cm), which serves to mix the high n states but does not markedly perturb either the $3^2S_{1/2}$ ground state or the $3^2P_{3/2}$ intermediate state. To illustrate this we estimate the size of the Stark shift of the m=0 component of the 3p level using perturbation theory. The major terms which contribute to the shift are due to the nearby 3s, 4s and 3d levels. The shift to lowest order is given by,

$$\Delta E \approx F^2 \left\{ \frac{|\langle 3s|z|3p\rangle|^2}{E_{3s}-E_{3p}} + \frac{|\langle 4s|z|3p\rangle|}{E_{4s}-E_{3p}} + \frac{|\langle 3d|z|3p\rangle|^2}{E_{3d}-E_{3p}} \right\} .$$

We evaluate this expression using matrix elements from Zimmerman's method (see appendix A) and energies from the NBS energy level tables [MOO 49] to obtain a shift of 0.048 Hz/V^2. At 50 kV/cm the shift is 120 MHz. The Stark shift is much smaller than the fine structure separation of this level, 17.2 cm^{-1}, so that $\vec{L}$ and $\vec{S}$ are not decoupled and m is not a good quantum number. The stationary states of the system are thus mixtures of the m values 0 and ± 1. (Note that for the Rydberg states, m is a good quantum number

since $\vec{L}$ and $\vec{S}$ are decoupled by the field.) The Stark shift is also smaller than the laser width, 0.5 cm^{-1}, so that the frequency of the yellow laser does not need to be adjusted when the field is varied. (The yellow laser is tuned to 16980 cm^{-1} and causes transitions from the $3^2S_{\frac{1}{2}}$ ground state to the $3^2P_{3/2}$ intermediate state.)

Only final states having certain m values can be populated, depending upon both the polarization of the laser which causes transitions from the $3^2P_{3/2}$ state (hereafter called the blue laser), and upon which m sublevels are present in the intermediate state. To determine the composition of the $3^2P_{3/2}$ state, we first ignore the hyperfine interaction so that the stationary states are $|j\, m_j\rangle$. We can express these states in terms of product states $|\ell m\rangle|s\, m_s\rangle$ according to the expression,

$$|j\, m_j\rangle = \sum_{m, m_s} a(m, m_s\,;\, \ell, s)\, |\ell m\rangle |s\, m_s\rangle$$

where the a's are the familiar Clebsch-Gordon coefficients. The expressions for each of the four sublevels of the $3^2P_{3/2}$ state are shown in Fig. II.4-1. The excitation is schematically represented for the cases of π and $\sigma^{\pm}$ polarization

$$\begin{array}{cccccccc} j & m_j & & \ell & m & s & m_s \\ \downarrow & \downarrow & & \downarrow & \downarrow & \downarrow & \downarrow \end{array}$$

$$|3/2 \quad 3/2\rangle = |1 \quad 1\rangle|1/2 \quad 1/2\rangle$$

$$|3/2 \quad 1/2\rangle = \sqrt{\frac{2}{3}}|1 \quad 0\rangle|1/2 \quad 1/2\rangle + \sqrt{\frac{1}{3}}|1 \quad 1\rangle|1/2 \quad -1/2\rangle$$

$$|3/2 \quad -1/2\rangle = \sqrt{\frac{1}{3}}|1 \quad -1\rangle|1/2 \quad 1/2\rangle + \sqrt{\frac{2}{3}}|1 \quad 0\rangle|1/2 \quad -1/2\rangle$$

$$|3/2 \quad -1/2\rangle = |1 \quad -1\rangle|1/2 \quad -1/2\rangle$$

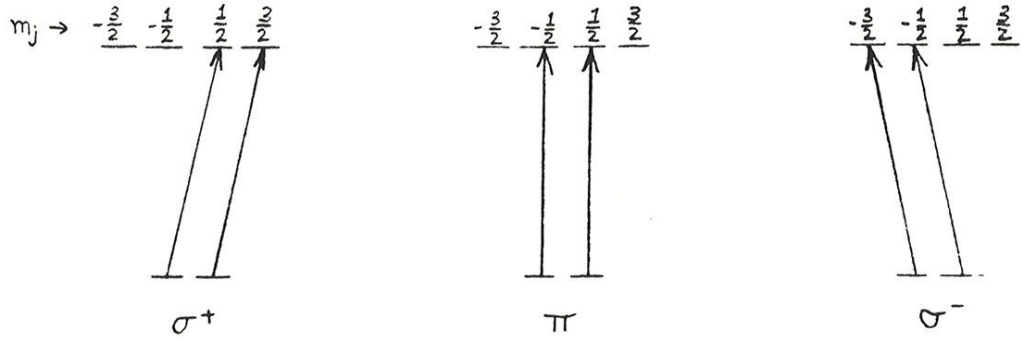

FIGURE II.4-1

Excitation diagram for the $3^2S_{1/2} \rightarrow 3^2P_{3/2}$ transition in sodium.

of the yellow laser according to the selection rules $\Delta m_j = 0$ and ± 1. We observe that regardless of the yellow polarization the $|m| = 0$ and 1 cases are present. The selection rules to the final Rydberg states are $\Delta m = 0$ or ± 1 for π or $\sigma^{\pm}$ polarization of the blue laser (the selection rule is for m since $\vec{L}$ and $\vec{S}$ are decoupled for these highly excited states). Thus if this laser is polarized along the field axis (π), then the $|m| = 0$ and 1 states are excited and if it is polarized perpendicularly to the field axis ($\sigma^+ + \sigma^-$), then the $|m| = 0$, 1 and 2 levels are excited.

The analysis is altered slightly if we include the effect of the hyperfine coupling in the intermediate state. The stationary states of the system are $|f\, m_f\rangle$, where $\vec{F} = \vec{I} + \vec{J}$. To determine the final state population we must consider the contribution to excitation from all 16 hyperfine sublevels (ie. f = 0, 1, 2, and 3). To make matters even more complicated, the relative phase of the sublevels plays a role since pulsed excitation results in a coherent superposition of sublevels [FRA 61]. (The condition for coherence is important when excitation takes place in a time shorter than $2\pi/\Delta\omega$, where $\Delta\omega$ is the splitting between levels.) In principle these coherence effects can alter the selection

rules (see appendix B). Fortunately, the general discussion of m composition is not changed, since there is no coherence between fine structure levels. If, however, one wished to determine absolute quantities such as oscillator strengths from knowledge of the final state population, it would be necessary to perform this complicated analysis. Since we only want to determine which $|m|$ states are excited the detailed analysis is not required.

We conclude that the $|m|$ values of the final states do not depend upon the yellow laser polarization. $|m| = 0$ and 1 Rydbergs are excited for linear polarization of the blue laser parallel to the field axis, and $|m| = 0$, 1 and 2 Rydbergs are excited for linear polarization of the blue laser perpendicular to the field axis.

CHAPTER III

APPARATUS

III.1 Lasers and Atomic Beams -- A New Technology

Recently there has been renewed interest in Atomic Spectroscopy due in large part to the development of the tunable dye laser. It is possible with this device to perform experiments that previously were inconceivable. This work is a good example. We have merged new laser technology with atomic beam techniques in order to study atoms in highly excited states.

We start with ground state sodium atoms which come from an effusive thermal source and form an atomic beam. The atoms are excited stepwise to Rydberg states by two pulsed tunable dye lasers. The intermediate state is resonant. The process is selective, in that by appropriate choice of laser frequencies, all of the excited atoms can be prepared in a particular quantum state. To study ionization we excite the atoms between electric field plates, which allows

us to apply large electric fields after, or in some cases during, excitation. The result of applying these large fields is the ionization the highly excited atoms, producing Na^+ ions and electrons. The Na^+ ions are accelerated by the field and escape the interaction region through a hole in the negative field plate, which is at ground potential. The Na^+ ions then strike a highly sensitive low noise ion detector. The ion formation is monitored as a function of parameters such as electric field strength and laser frequency. In this chapter we describe the equipment and calibration procedures used to carry out experiments on field ionization.

III.2 The Lasers

The blue and the yellow lasers which were used in this work are of the Hansch design [HAN 72]. A schematic diagram of the laser system is given in Fig. III.2-1. The components are identified in the caption. Both lasers were side-pumped by a common pulsed nitrogen laser (3371 Å, 100 kW peak power) which assured synchronization of the two visible lasers. The UV pump laser (AVCO model C950) operated with a repetition rate of 50 Hz. The yellow laser peak power was 1 kW using Rhodamine 6G dye (Molectron #70360). The peak power of the blue laser was 3 kW using either 4,4-diphenylstilbene dye (Molectron #70353) for accessing $n>26$ (4087 - 4112 A), or 1,4-bis-(2-methylstyryl)benzene dye (Molectron #70354) for accessing n=10-30 (4105 - 4277 Å). The pulse duration of the lasers was 5 nsec. The linewidth, the value of which was a sensitive function of the focussing of the cavity beam expander, was typically 0.5 cm^{-1}. To tune the laser the angle of the echelle grating (Bausch and Lomb model 35-63-05-460), which also served as end mirror for the cavity, was changed. Initially the grating position was manually adjusted using a mirror positioner (Oriel model 1450). Later we added a servo controller, described in ap-

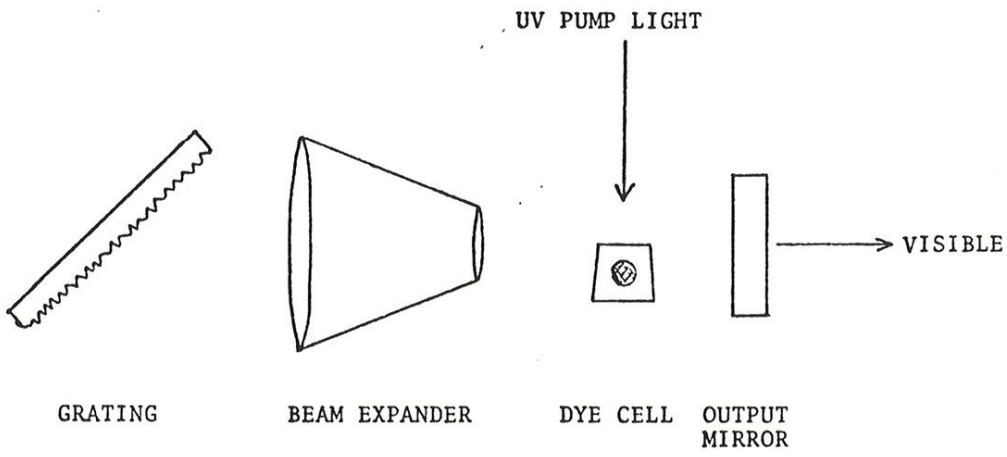

FIGURE III.2-1

Schematic of the pulsed dye laser. One of two lasers which are used to perform field ionization experiments in sodium.

pendix C, to allow positioning of the blue grating under computer control. The resetability of the laser for both manual and computer operation was better than the linewidth. The net drift for an eight hour period under average laboratory conditions was less than 1 cm^{-1}.

To calibrate the computer scan of the blue laser we used a flat Fabry-Perot interferometer (Burleigh model RC-40) with dielectric mirrors coated for use in the blue. The interferometer was used as a narrow-band tunable filter with the free-spectral-range (FSR) set to about 10% of the full scale tuning range of the blue laser. The throughput of the interferometer was monitored with a photodiode (Monsanto model MD1). (The transmission function of the interferometer is peaked and repeats every FSR as the input frequency is varied.) By noting the location of the transmission peaks with respect to the grating controller voltage we were able to calibrate the scan. The linearity was measured to be better than 2% except for the first 10% of the sweep, which was affected by mechanical lash in the mirror positioner.

III.3 Atomic Beam and Interaction Region

The nearly colinear laser beams intersected a collimated (3 mm dia.) sodium atomic beam at right angles inside the vacuum chamber, which was maintained at an ambient pressure of 10^{-6} torr (see Fig. III.3-1a). The lasers, focussed to approximately 1 mm spots, overlapped at the interaction region. A conventional effusive oven source with nozzle aperature of 80μ was operated at 450°C. The atomic flux was monitored by means of a surface ionization detector using a hot tungsten filament (0.01 cm dia. x 1 cm) [RAM 69, sect. XIV.3.3] located 30 cm from the nozzle. The current from the detector was about 1 na for the source conditions indicated, which corresponds to a density at the interaction region (midway between the nozzle and the detector) of 10^9 atoms/cm^3 . The average atomic velocity in the beam is given by [RAM 69, sect. II.3.2],

$$\langle v \rangle = 1.33 \sqrt{\frac{2 k_B T}{M_{Na}}} \approx 1 \text{ mm}/\mu\text{sec},$$

where M_{Na}, the sodium mass, is 23 AMU, and T, the temperature, is taken to be 450°C. A 5 gram charge of sodium (MSA Research corp) provided about 150 hours of beam time.

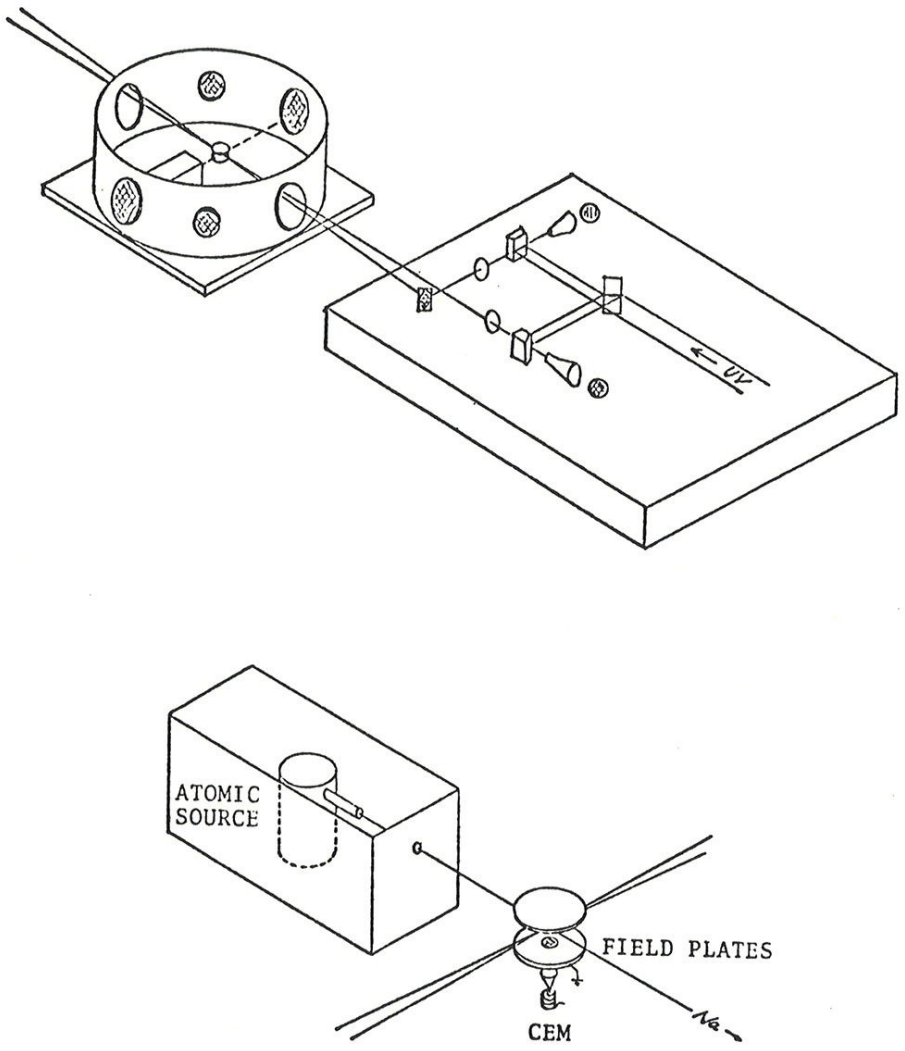

FIGURE III.3-1

(a) Experimental arrangement showing vacuum chamber (uncovered) and the two dye lasers.
(b) Interaction region where the atomic source, field plates and CEM are shown.

The interaction volume was located midway between two electric field plates, seperated by three 0.500(8) cm Delrin spacers, and held together by nylon machine screws. The lower plate was at ground potential and had a 1 cm hole on center which was covered with a fine wire mesh so that positive ions, accelerated by the field, could escape. The ions impinged upon the cone shaped cathode (1 cm dia.) of the channel electron multiplier (CEM -- Gallileo Electro-Optic corp model 4039 EIC), which was kept at a potential of about -2.5 kV. These energetic ions caused electrons to be ejected on impact which were, in turn, multiplied by cascades and collected at the anode of the CEM. The CEM was so sensitive that individual ions could be detected with ease. A single ion resulted in a pulse of 10 nsec duration and 3 mV peak amplitude into a 50Ω termination. A schematic of the interaction region is given in Fig. III.3-1b.

III.4 Timing and Electronics

The six experiments that are described in the next chapter used either of two detection modes, namely, the PULSED FIELD mode in which excited atoms were ionized by a large electric field pulse soon after excitation, or the FIXED FIELD mode in which ionization occurred spontaneously in the static field. The pulsed field mode was used to study the excitation spectrum of Rydberg states. The fixed field mode was used to measure excited state ionization rates in strong static fields.

Pulsed Field Mode

In the pulsed field mode, Rydberg atoms are ionized about 1 μsec after laser excitation by application of a 15 kV/cm field pulse of 3 μsec duration. (For most efficient operation the pulse should be applied as soon after excitation as possible to minimize loss of signal due to radiation, and in any case it must be applied before the excited atoms drift out of the interaction region, which takes about

10 μsec.) The laser excitation takes place either in zero field or in a static electric field. The field is applied by a HV power supply (Ortec model 456) connected to the upper field plate through a 100 kΩ resistor which protects the supply from voltage transients. The pulsed field is derived from a HV trigger module (EG&G model TM-11) which is coupled to the plate through a 0.1 μf capacitor. The effective pulse risetime is approximately 500 nsec. A timing diagram is shown in Fig. III.4-1a. In this mode the integrated output of the ion detector (CEM) is proportional to the number of excited atoms that exist at the moment when the pulsed field is applied. The method for integrating the CEM output is described towards the end of this section.

Fixed Field Mode

In the fixed field mode, Rydberg atoms formed in a dc field are observed to decay exponentially in time from the moment that they are excited, provided that the field is sufficiently large that the primary decay mechanism is field ionization. The ion production is directly monitored by the CEM. The timing for this mode of detection is illustrated

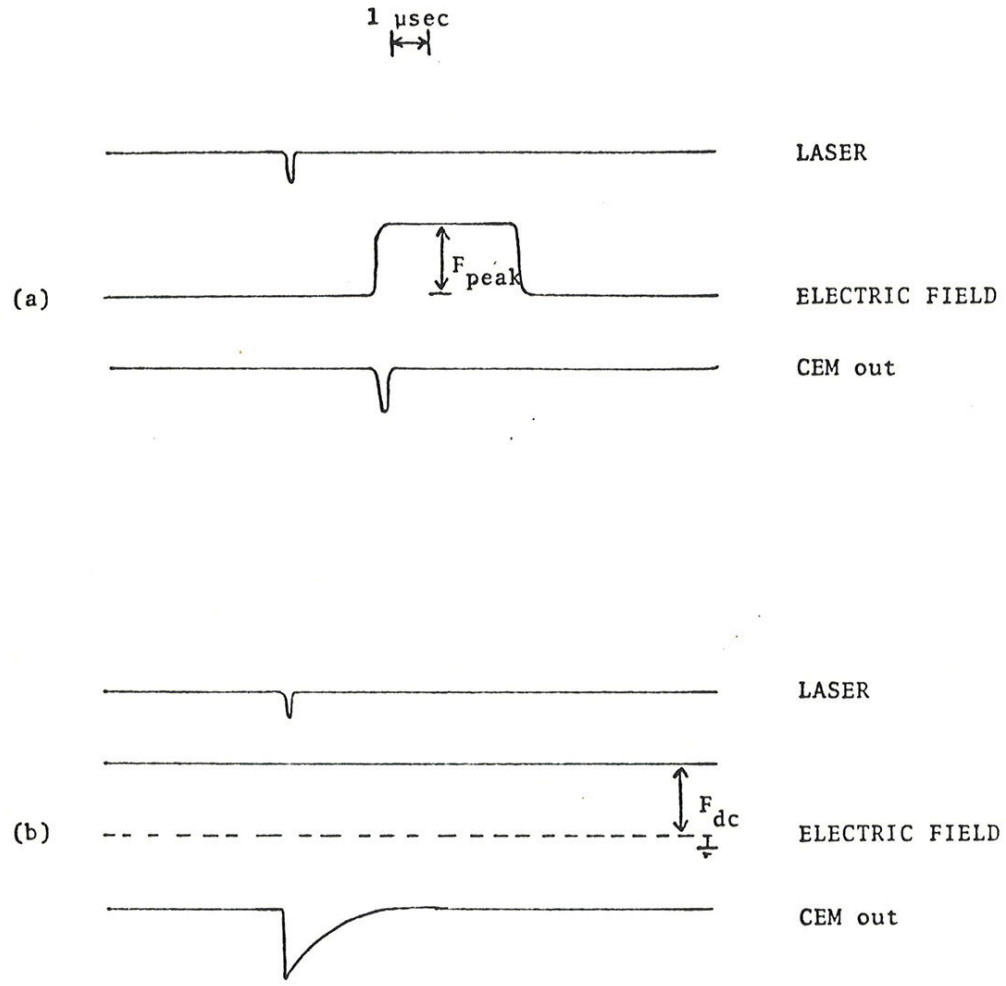

FIGURE III.4-1

(a) Timing diagram for PULSED FIELD detection.
(b) Timing diagram for FIXED FIELD detection.

in Fig. III.4-1b. The CEM signal that is sketched corresponds to large numbers of detected ions for each laser excitation pulse. The CEM can also be used for observing single ions which are detectable as individual pulses after electron multiplication. To accurately measure decay rates the CEM gain must be independent of the position at which the ion stikes the cathode surface, because the motion of the atoms maps a spread in ion creation time into a spread in space. Unfortunately the gain of the CEM is not uniform over the cathode surface [HIR 76]. The particle detection efficiency (analogous to the quantum efficiency for photomultipliers), however, is uniform over the surface. Thus as long as one counts single ions, where each pulse is assigned the same weight regardless of pulse height, no corrections to the detected signals are required.

Single Event Timing Spectrometer

In the experiment described in sect. IV.4.A of the following chapter, ionization rates were determined by fitting to an exponential function the decaying distribution of first ion arrival times obtained with a single event timing

method. The fit to the exponential was performed using a general linearized least squares algorithm [WIN 70], sect. 4.2. Each data point was assigned a weight according to a Poisson distribution. The distribution of arrival times of the first ion detected after excitation was determined in the low ion production limit. For the case where only one event is observed for each excitation pulse, the arrival time distribution is proportional to the population of the excited state in time [POU 72]. To determine this distribution we used a CAMAC time-to-digital converter (TDC -- LeCroy Research Systems model 2228). The laser trigger was used to start the TDC timer and the detected single ion pulse was used to stop it. A CAMAC scaler (Ortec model S424B) counted how many stops occurred after each laser pulse and the software vetoed cases that had more than one stop for a given start. (The pulse pair resolution of the scaler is 7 nsec. To minimize the multiple pulsing error we made sure that the total stop rate was less than 10% of the start rate for decay rate measurements greater than 10^7 sec^{-1}.) Each acceptable event was recorded by incrementing the data channel that was associated with a given time interval (in this case the computer emulated a multichannel analyser). A schematic of this setup is given in Fig. III.4-2.

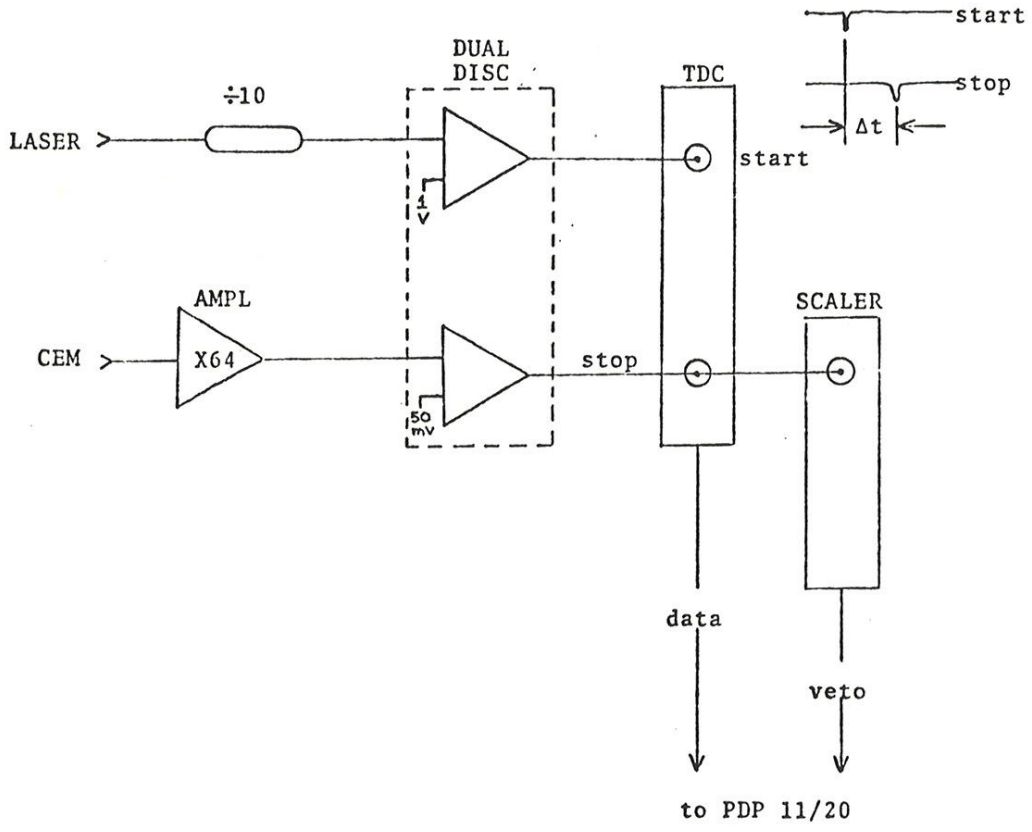

FIGURE III.4-2

Schematic of the SINGLE EVENT TIMING SPECTROMETER.

The TDC was calibrated to better than 0.5% using a precision oscillator and discriminator to provide pulses separated in time by a known amount [LIT 74]. The resolution was measured by timing ions formed promptly with laser excitation (eg. by exciting rapidly ionizing continuum states, that is, photoionization) and then observing the ion arrival time spread which, in this case, is due entirely to instrumental dispersion. The overall timing resolution, including the response of the CEM and the transit time dispersion of ions was measured to be better than 10 nsec for applied fields in excess of 10 kV/cm (total transit time to the detector is less than 200 nsec).

Boxcar Integrator

For several experiments it was necessary to linearly integrate the CEM output over a specified time interval which we shall call the integration window (IW). To accomplish this we constructed a boxcar integrator using state-of-the-art fast electronic modules (see Fig. III.4-3). The integration window was determined by a gate and delay generator (Berkeley Nucleonics corp model 8010) triggerred

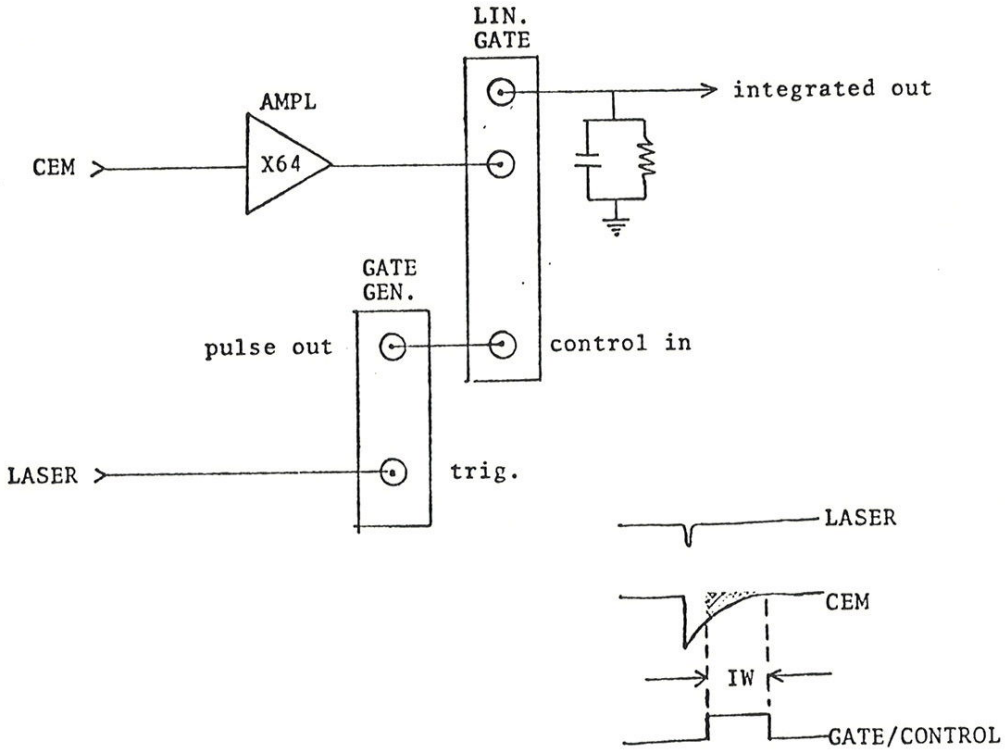

FIGURE III.4-3

Schematic of the BOXCAR INTEGRATOR.

by the laser, which switched a linear gate (Ortec model LG 101/N) through its control input. The linear gate allowed only a portion of the signal from the CEM, as determined by the output from the gate and delay generator, to be integrated by an RC network (30 msec holding time) which was connected to the linear gate output. Using this boxcar integrator it was possible to detect single ions with a signal-to-noise ratio of better than 10. In a typical case the integrated signal was digitized using a CAMAC analog-to-digital converter (ADC -- Kinetic Systems corp model 3520) while some parameter (eg. blue laser wavelength, static field,etc.) was slowly stepped every 10 or so laser flashes. The entire process was under computer control and the information was stored on line.

CHAPTER IV

EXPERIMENTS ON FIELD IONIZATION

IV.1 Introduction

The aim of this thesis is to investigate field ionization in one electron atoms. In order to measure ionization rates it is necessary to develop methods for exciting, detecting and identifying particular Stark states of the atom. The first section of this chapter describes techniques developed for exciting and detecting Rydberg states of sodium. The second section deals with excitation and identification of selected Stark sublevels in electric fields up to values where spontaneous ionization starts to be significant, and in the final section we describe two experiments where field ionization rates for selected Stark states are determined.

IV.2 Excitation and Detection of Rydberg States

IV.2.A Spectroscopy of ns and nd States of Sodium

We describe here the method used to excite and detect Rydberg levels of sodium. The techniques which were developed to carry out this experiment are also used in the later stages of our studies.

At time zero the two pulsed lasers simultaneously illuminate ground state sodium atoms in the atomic beam. The yellow laser is tuned to the $3^2S_{1/2} \rightarrow 3^2P_{3/2}$ transition at 16980 cm^{-1} ; its power is sufficient to saturate the transition. (A calculation of the excitation rate is presented in appendix D.) The blue laser is tuned to a frequency which, for the moment, we assume is in resonance with the $3^2P_{3/2} \rightarrow n^2S_{1/2}$ transition. (The second step of excitation is below saturation for the states that we work with, that is, $n > 13$.) At $t=1\ \mu sec$, before the majority of the highly excited atoms have either radiatively decayed or drifted out of the interaction region, a large electric field is applied which ionizes the Rydberg atoms and accelerates the positive ions towards the "ground" electric field plate. The ions pass

through a grid in this plate and then strike the cathode of the channel electron multiplier (CEM). Typically hundreds of ions are detected for a single laser pulse. The CEM signal is integrated by the fast boxcar integrator described in section III.4. For a laser scan the frequency is under computer control by means of the grating positioning mechanism. At each frequency the laser is fired several times and the total signal is stored by the on-line computer. The grating is then advanced to the next channel and the process is repeated.

The result of one scan, 256 channels, is presented in fig. IV.2.A-1. A timing diagram is also included to indicate the integration window. A peak occurs whenever the blue laser is in resonance with either an ns or nd level. With this method we have been able to identify s and d states in the range n=23-38. (Above n=38 we were not able to resolve s and d states given the laser width of 0.5 cm^{-1} and below n=23 we could not ionize the excited atoms since the largest pulsed field that we could attain, at that time, was 1.2kV/cm.) The wavelengths for excitation were measured using a SPEX monochrometer model 14018. The results were used to determine the quantum defects for the s and d states

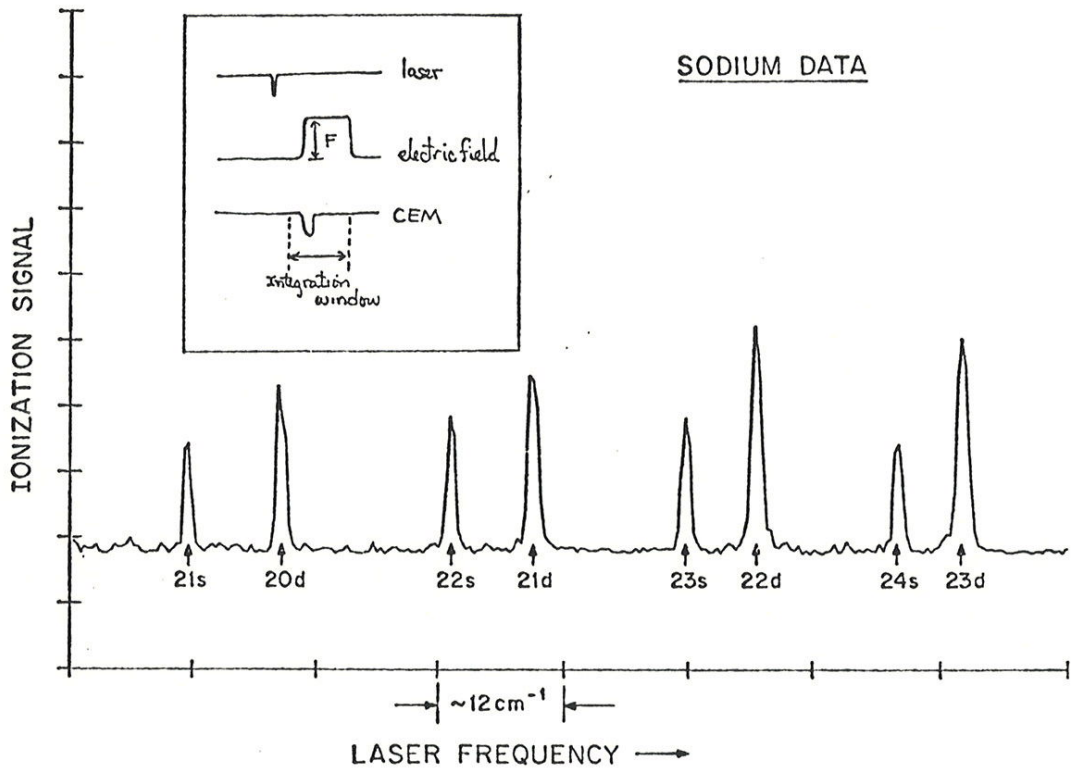

FIGURE IV.2.A-1

Ionization signal versus blue laser frequency using pulsed ionization detection. Energy is increasing to the right.

(the values for the ionization limit and the $3^2S_{\frac{1}{2}} \rightarrow 3^2P_{3/2}$ separation were taken from the NBS tables [MOO 49]). For s states we found that $\delta_0 = 1.35(4)$ and for d states $\delta_2 = 0.00(4)$. The quoted deviation represents the limit of error of these quantities. This data is plotted in Fig. IV.2.A-2 in a manner such that the function,

$$E = -\frac{\alpha}{(n-\beta)^2}$$

is represented by a straight line where the slope is $\sqrt{\alpha}$ and the n axis intercept is β. For α we used the Rydberg constant for sodium and for β we used the quantum defects which best fit our data. In this plot the lower ns and nd state energies (NBS tables MOO 49) are also included for comparison. Our results are consistent with the NBS values.

In principle one could determine relative oscillator strengths from the amplitudes of the excitation curves, however, we could not do so for two reasons. First, the blue laser power is not uniform over the entire 100 cm^{-1} range, and we did not normalize the data to account for this variation. Second, the CEM is easily saturated (due to "pileup") so that the ionization signal scale is not linear.

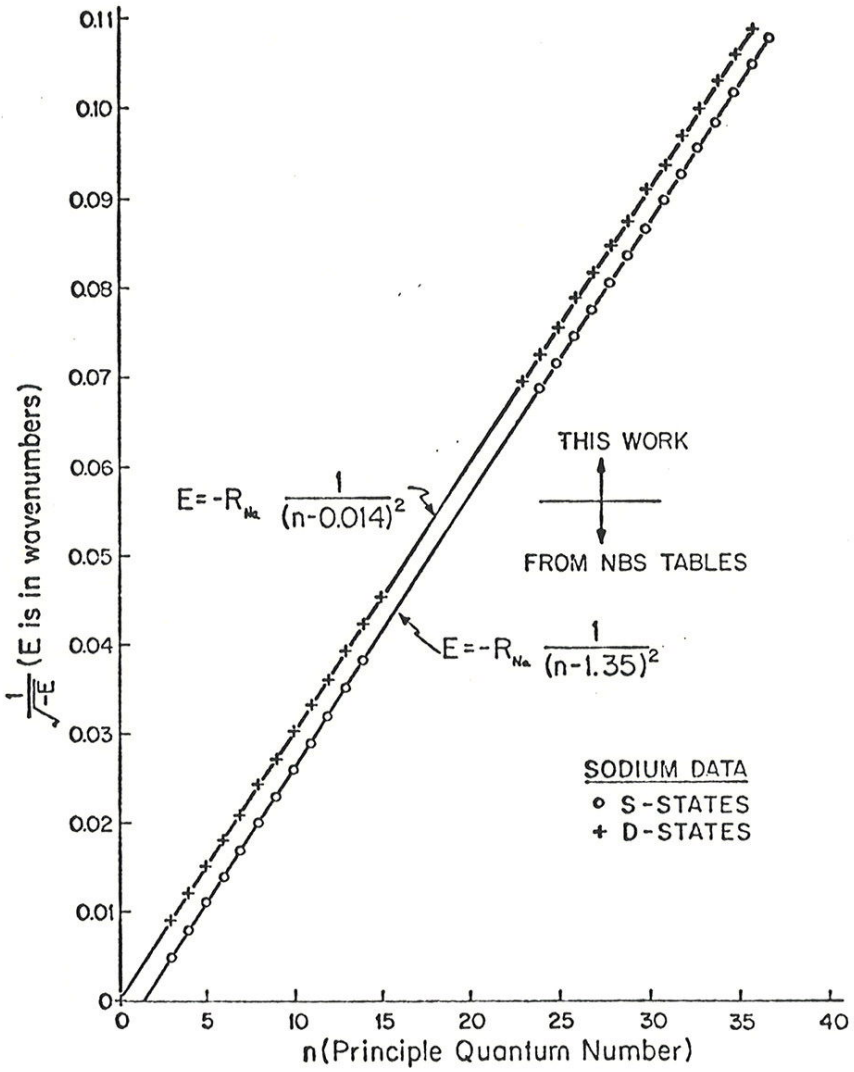

FIGURE IV.2.A-2

Plot of $1/\sqrt{-E}$ versus n for s and d states of sodium. The n axis intercept is the quantum defect.

This later problem could have been avoided by using a discrete dynode electron multiplier instead of the CEM.

IV.2.B Ionization Efficiency vs. Pulsed Field Strength

The problem here is to investigate how the ionization signal strength varies as the peak amplitude of the electric field pulse is changed. The pulsed field was monitored by means of an oscilliscope coupled to the field plates through a x10 voltage probe (Tektronix model P6008). The lasers were set to excite either an ns or nd level and the integrated output was measured as a function of the field pulse amplitude.

For s states (n=25-38) the ionization signal exhibits a sharp threshold. Above the threshold field there is no variation in the signal strength, which suggests that all of the excited atoms are ionized. Below the threshold field, virtually no ions are observed. The d states (n=25-38) also exhibit a rapid change in the ionization signal, however, it is not as abrupt as that for the s states. These features are illustrated by the experimental ionization curves for the 30d and 31s levels displayed in Fig. IV.2.B-1. Timing information is given in the inset.

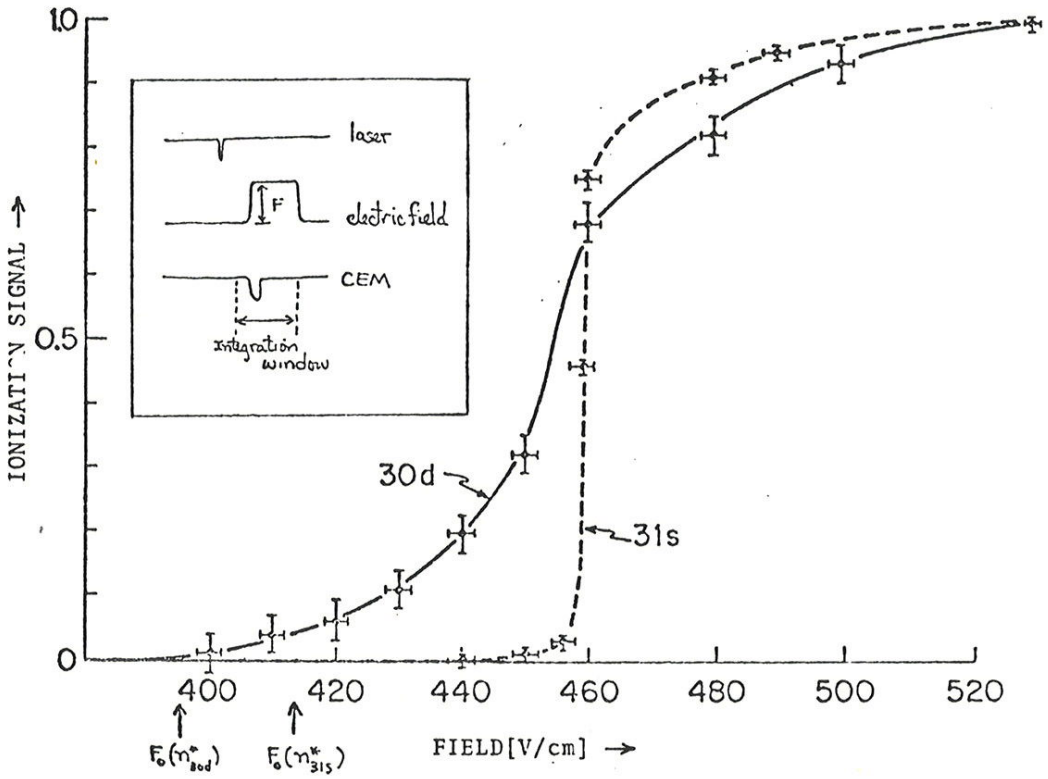

FIGURE IV.2.B-1

Ionization signal versus amplitude of the pulsed field. Curves correspond to ionization of 30d and 31s levels which are excited in zero field. The classical threshold fields according to the discussion of sect. I.1 are indicated [from DUC 75].

In Fig. IV.2.B-2 we have plotted the threshold fields for ns states. For comparison the classical value, $F_o = E_{n\ell}^2/4$ (see sect. I.1) is also included where we use the zero field expression for the energy. It is evident that the threshold fields scale as $(n - \delta_o)^{-4}$ and are about 10% larger than those predicted by the crude classical treatment. (The fact that ionization starts at fields above the classical values does not mean that the atoms are ionizing in an over-the-barrier sense, rather it means that the classical estimate is in error.)

The ionization curves for d states are not as sharp as those for s states (see Fig. IV.2.b-1). We attribute this to the fact that both $|m|=0$ and 1 levels are excited and since $|m|$ components are expected to ionize at different field values, the curves are smeared. This hypothesis has recently been tested by Gallagher et al [GAL 76b] for nd states with n ranging from 15 to 20. They found steps in the ionization curves as the pulse amplitude was varied, and identified the steps as being due to the different ionization critical fields for the $|m| = 0$, 1 and 2 sublevels of the nd state. The fact that different $|m|$ sublevels ionize at different fields was used by the SRI group to detect transitions

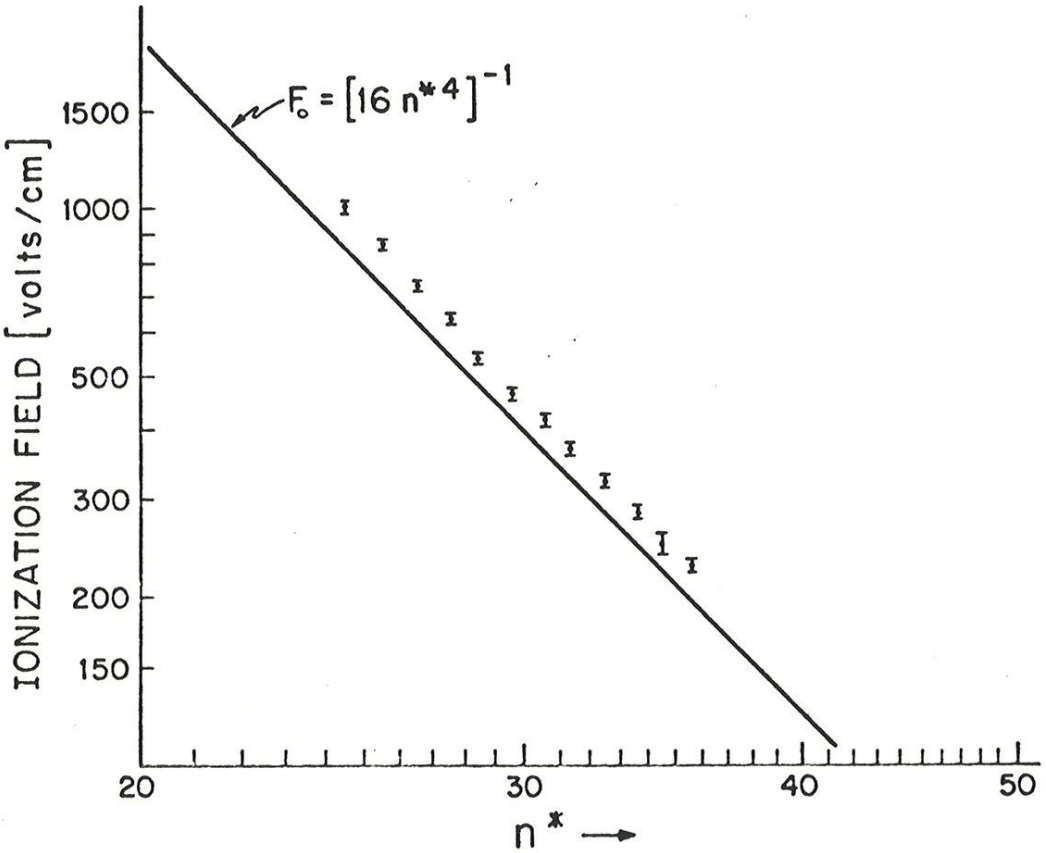

FIGURE IV.2.B-2

Threshold fields for ns levels. The solid line is the classical result according to the discussion in sect. I.1 where we have taken the energy to be the zero field value. The effective quantum number, n^* , is equal to $n-\delta_\ell$, where δ_ℓ is the quantum defect. In this case, $n^* = n-1.35$ [from DUC 75].

between the two fine structure levels allowing them to make radio frequency measurements of the nd fine structure for the first time [GAL 76c].

The sharp threshold reflects the property that the ionization rate varies rapidly as a function of field. In principle one could use detailed information about the ionization characteristics to infer the ionization rate, however, the analysis would be complicated by the fact that the final state or states of the system would depend upon how rapidly the field is applied. (If the rate of change of the field is slow compared with the smallest separation between adjacent levels then the passage to high field is adiabatic [ZEN 32, LAN 32]. The SRI experiment on pulsed field ionization demonstrated that while some states pass to high field adiabatically others do not [GAL 76b].) Also the field must be applied in a time short compared with the decay lifetime in order to measure it. To determine decay rates we have chosen another method, described in sect. IV.4.A, where one does not vary the field after excitation thus simplifying the measurement process.

Even though pulsed ionization is not especially useful for ionization rate studies the threshold behaviour provides a means for selectively detecting excited states of the atom. This important property can be used to advantage in high resolution spectroscopy to detect transitions between nearby levels as the SRI workers did and also can be used to perform final state anaysis when many Rydberg levels are present.

IV.3 Stark Structure Maps

The problem here is to explore photo-excitation in the presense of an external electric field with two questions in mind. First, is the transition probability to the Stark states sufficiently large to excite a detectable population of atoms? . And second, can we calculate of the Stark structure well enough to identify a given resonance with a particular quantum state? The next two experiments were designed to answer these important questions.

In deciding which Stark states are to be singled out for study, we require that two conditions be met, namely, that the spacing between Stark levels must be sufficiently large that individual levels can be resolved, and that the excited levels must be capable of being ionized by the 15 kV/cm pulsed field that we apply. The first condition requires n to be less than 20 while the second condition requires that n be greater than 11. As a rule we have tried to work with as low a value of n as is possible since the smaller the number of levels, the easier the task of comparing theory and experiment.

IV.3.A Stark Spectrum -- Fixed Frequency Method

There are two ways to make an experimental map of the Stark structure. One can sweep the electric field with the laser frequency fixed, or one can sweep the laser while keeping the field fixed. We chose field-scanning as the first method to try since it is easier to scan the field than to scan the laser.

The blue laser is tuned into resonance with either the ns or nd level in zero field so that the energy is known. As before, pulsed ionization is used for detection. The ionization signal is integrated and stored as the electric field is stepped. (To step the field, the DAC output is connected to the remote voltage programming of the Ortec model 456 HV power supply). The process is illustrated graphically in the Stark structure diagram, Fig. IV.3.A-1a, for levels near 19d. The laser was narrowed by use of an intercavity etalon. The width, 0.1 cm^{-1}, is indicated in Fig. IV.3.A-1a.

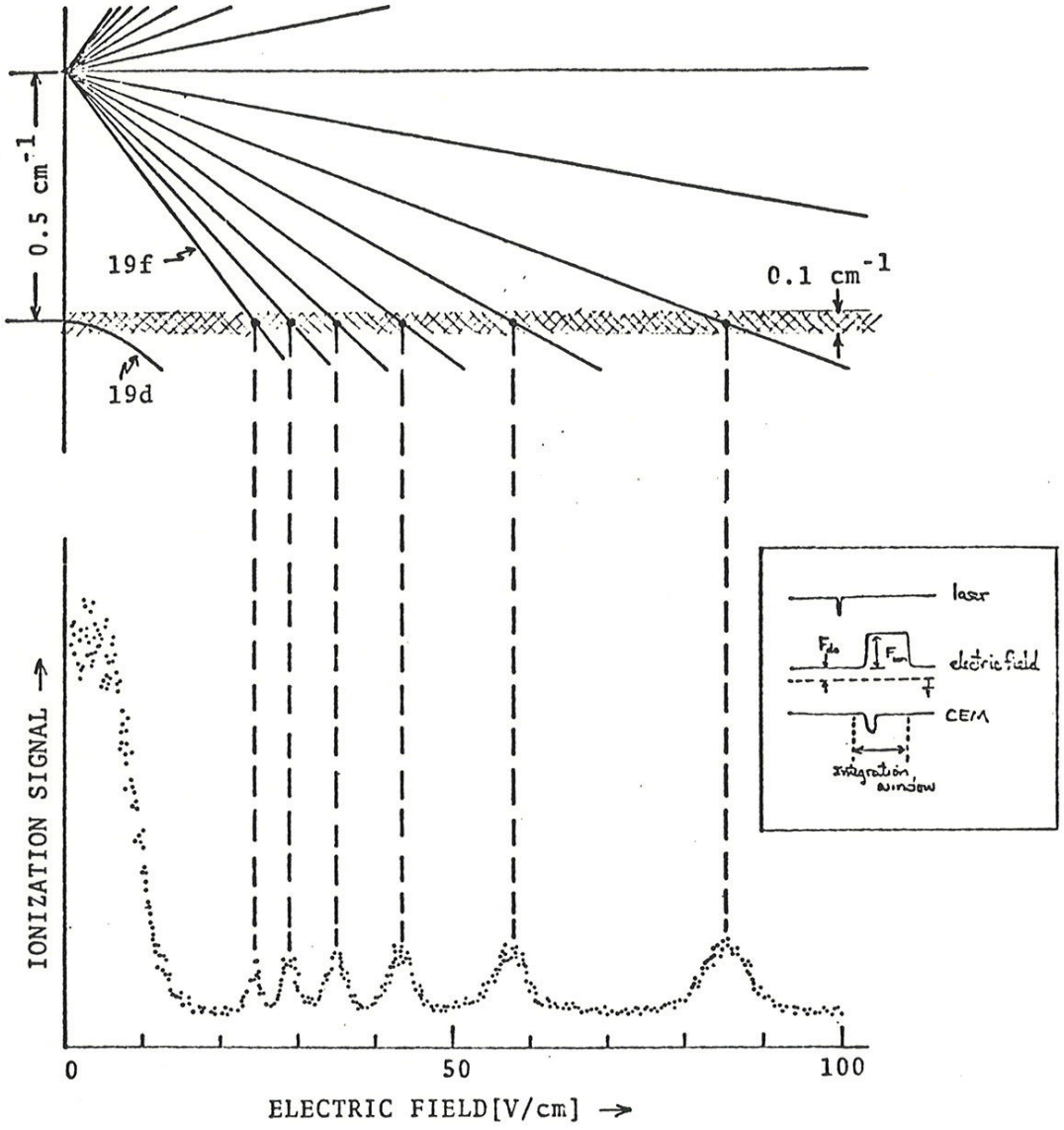

FIGURE IV.3.A-1

(a) Stark structure result for $|m|=0$ and 1 cases according to sect. II.3. The fixed laser frequency and width are shown.
(b) Data obtained by sweeping the dc field.

The theoretical curves, shown in Fig. IV.3.A-1a, were obtained by diagonalizing the energy matrix for the $|m| = 0$ and 1 cases with n = 18, 19 and 20 (see sect. II.3). The data is shown in Fig. IV.3.A-1b. Timing information is included in the inset. The apparent width of these peaks reflects the slope of the levels at the resonance energy for a given laser linewidth. Thus the lowest level of the n=19 manifold (ie. 19f in zero field), which has a large slope is narrow, and the 19d level which has no first order shift in field, is broad. The calculated field values for the locations of the peaks are indicated in the figure. In every case theory and experiment agree to within the 3% absolute uncertainty in the applied field. The peak amplitude is a measure of excited state population and in principle, could be used to determine the oscillator strengths for the various transitions. We, however, have not performed this analysis. Note that electric dipole selection rules forbid transitions in zero field to all of the levels shown in Fig. IV.3.A-1a, save 19d. These forbidden states can be excited in the field because of Stark mixing, chiefly with the nearby 19d level [ZIM 74].

The field-scanning method, sometimes called Stark spec-

troscopy, has advantages of simplicity of excecution, and is the only method available if the laser is fixed. (Ducas and Zimmerman have used this technique to observe IR transitions (10s - n=17) in sodium using a 10μ cw CO_2 laser [DUC 77].) The laser-scanning method is better suited for mapping complex level structure and so we now turn to this method.

IV.3.B Stark Spectrum -- Fixed Field Method

The method is similar to that of the previous experiment except that the field is fixed while the blue laser is scanned. The full scale scanning range of the laser is 100 cm^{-1}. To investigate the region near the n=15 manifold the scan is centered at 23994 cm^{-1} (4167 Å). The laser is π polarized so that only $|m|=0$ and $|m|=1$ levels are excited. For n=15 the threshold field is 6 kV/cm. We restrict ourselves to fields below this value so that spontaneous ionization is not important.

Fig. IV.3.B-1a shows a scan in zero field. The peaks correspond to the 17s, 15d and 16s levels. The scan in Fig. IV.3.B-1b is identical except that excitation takes place in a static field of 92 V/cm. The two s peaks are virtually unshifted by the field, the 15d level appears to have broadened, and a new peak has appeared. The new peak is identified as the 16p state which was inaccessible in zero field according to the electric dipole selection rules. In the presence of an electric field it can be excited because of Stark mixing, predominantly with the nearby 15d

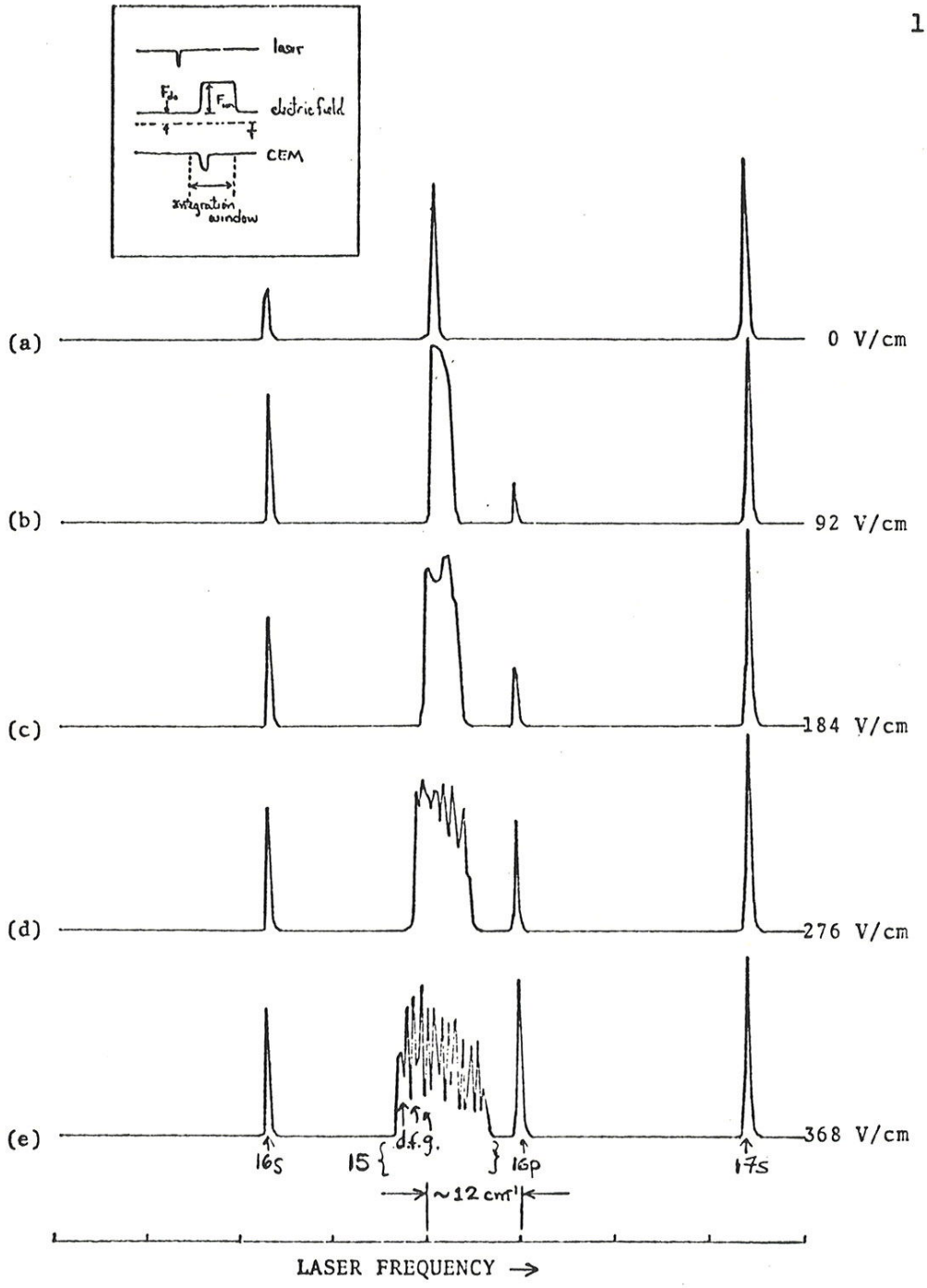

FIGURE IV.3.B-2

Laser scans for the region near n=15.

(a) The zero field excitation curve is shown.

(b-e) Excitation curves taken in a static field, the value of which is noted at right.

level. The broadening of the 15d level can similarly be understood as due to the emergence of the higher angular momentum states (ie. $l \geq 3$) in the spectrum which like the 16p level were inaccesible at zero field. This hypothesis is dramatically verified as the field is increased and we begin to resolve these states as shown in Figs. IV.3.B-1c,d&e. In the scan for 368 V/cm the states are identified. (It is of course incorrect in a strict sense to describe any of these states by their angular momentum, because l is not a good quantum number in the field. When we indicate that a level in the field is the nl state we mean that it connects with the nl state when the field is adiabatically reduced to zero.) Scans were taken for increasing field values in steps of 92 V/cm and are displayed in Fig. IV.3.B-2a.

Calculated energies are given in Figs. IV.3.B-2b ($|m| = 0$) and IV.3.D-2c ($|m| = 1$). The curves were computed along the lines described in sect. II.3 including the n = 14, 15, 16 and 17 manifolds in the diagonalization.

Many features are to be noted in Fig. IV.3.B-2a. First is that all of the levels in the theoretical diagram are ob-

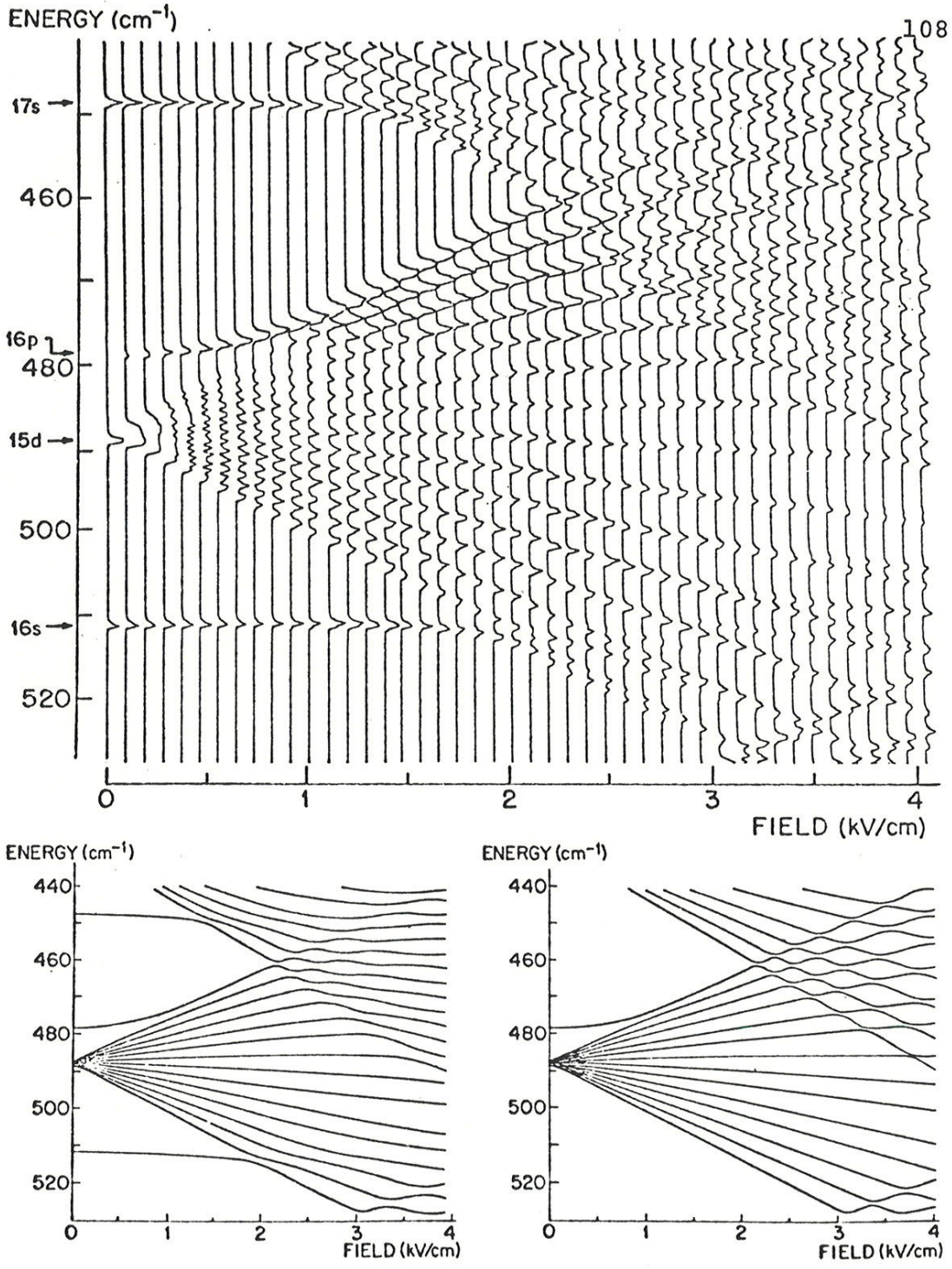

FIGURE IV.3.B-?

(a) Experimental excitation curves for Rydberg states of sodium in the vacinity of n=15. A tunable laser was scanned across the energy range displayed (vertical axis). The zero of energy is the ionization limit. A signal, generated by ionizing the excited atoms, appears as horizontal peaks. Scans were made at increasing field strengths and are displayed at the corresponding field values. Both $|m|=0$ and 1 states are present.
(b) Calculated energies for the m=0 states displayed above.
(c) Calculated energies for the $|m|=1$ states displayed above.

served, or in other words, none of the transitions from the $3^2P_{3/2}$ intermediate state to the numerous Stark levels is forbidden. (This is markedly different from the situation in zero field.) As predicted, the s and p levels, which are far removed from the manifold of states, are unshifted in low fields. The linear Stark states of the $|m| = 0$ and 1 cases nearly overlap in low field and appear degenerate up to fields where level anticrossings become important. Level anti-crossing with the 16s state is responsible for the apparent branching of the lowest Stark level at 2 kV/cm where the $|m|=0$ state is repelled. The $|m|=1$ state is unaffected. A number of similar branch points which collectively break the near degeneracy of the $|m| = 0$ and 1 levels can be seen in Fig. IV.3.B-2a. The observed level structure agrees with the theoretical predictions to within the 3% absolute field uncertainty and the 2% linearity of the frequency scan.

The motivation for understanding the Stark structure was to be able to relate ionization behaviour of sodium states to corresponding hydrogen states for which extensive ionization rate calculations have been made. In sect. II.3 we noted the difference between the sodium and hydrogen Stark structures. Unfortunately, the non-hydrogenic sodium

s and p states radically affect the level structure at both high and low field for the $|m| = 0$ and 1 cases. For this reason we chose to study the $|m| = 2$ case which we believe is more easily described in terms of a hydrogen model. The $|m|=2$ Stark structures of the sodium and hydrogen systems are virtually identical except for narrow field regions near level anti-crossings.

Summarizing, we have conducted a survey of the Stark structure of the sodium case near n = 15 and have discovered that all Stark levels having $|m| = 0$, 1, and 2 can be excited (the $|m|=2$ case was investigated by polarizing the blue laser perpendicular to the field axis. These results have not been presented). We also found that, within experimental error, the energies of the $|m| = 0$, 1 and 2 levels can be accurately predicted by means of the theory which was described in sect. II.3. We conclude that because of the differences between the sodium and hydrogen Stark structures of the m = 0 and 1 states, that they are not especially useful for testing hydrogen ionization theory. We have decided to concentrate on the $|m|=2$ case which more closely resembles hydrogen.

IV.4 Tunneling Rate Measurements

We have used two methods for measuring ionization rates: the DIRECT TIMING METHOD in which the decay lifetime of the excited level is determined, and the LINE BROADENING METHOD where the excitation linewidth is measured.

With the DIRECT TIMING METHOD one measures the ion production rate as a function of time after instantaneous excitation. The ionization signal decays exponentially, where the decay rate is the sum of the radiative rate, Γ_{rad}, and the spontaneous ionization rate, Γ_{ion}. We generally operate in a region where $\Gamma_{ion} >> \Gamma_{rad}$ so that Γ_{rad} does not need to be known accurately. For n=13 the radiative decay rate is about 10^5 sec^{-1} [HIS 64], thus total decay rates exceeding 10^6 sec^{-1} may be interpreted as due dominantly to ionization. This method is restricted to rates below about 10^6 sec^{-1} because of timing resolution. (In principle one can do better by at least an order of magnitude using state-of-the-art timing techniques.) Sect. IV.4.A describes measurements obtained for the sodium $|m|=2$ levels near n=12 using this technique. The results are compared with hydro-

genic tunneling theory for certain Stark levels.

The LINE BROADENING METHOD offers an alternative approach for measuring ionization rates. In atomic absorption or emission spectroscopy, if the decay of a level is exponential then the spectrum is Lorentzian with linewidth (fwhm) equal to $\Gamma/2\pi$ [HEI 54, chapt. 18]. (Note that this is smaller by a factor of 2 than the linewidth if the spectral power density of the electric field is measured.) The lineshape is determined by scanning the frequency of the exciting laser and monitoring the net ionization signal. This method is applicable when the natural width is large compared with the laser width. (Doppler broadening does not play a role here since the experiment is carried out in an atomic beam with transverse excitation.) The linewidth of the laser is 0.5 cm^{-1}, which means that rates in excess of about 10^{11} sec^{-1} can be measured. Sect. IV.4.B describes an experiment in which the line broadening method has been used to determine ionization rates for several $|m| = 0$ and 1 levels and to provide an upper bound to the decay rates of $|m|=2$ levels.

IV.4.A Direct Timing Measurements of Decay Rates

Having developed techniques for selectively populating Stark sublevels (see sect. IV.3), we turn to the problem of measuring ionization rates in strong electric fields. In this section measurements made with the direct timing method are discussed.

Our interest is in the field dependence of the ionization rate so that we must be able to distinguish a given Stark level, from the complex spectrum, for many different values of the field. To accomplish this we made a Stark map of a region near the n = 12 manifold in a similar manner to that described in sect. IV.3.B. The blue light is polarized perpendicular to the field axis so that the $|m|=2$ levels, as well as $|m| = 0$ and 1 levels, can be excited. An experimental map is shown in Fig. IV.4.A-1b for the region indicated by the box in Fig. IV.4.A-1a. Note that instead of using pulsed ionization detection, we monitor the total number of ions formed for all times after laser excitation. In regions where the field ionization rate is small (ie. the principle decay mechanism is radiation) we still observe a

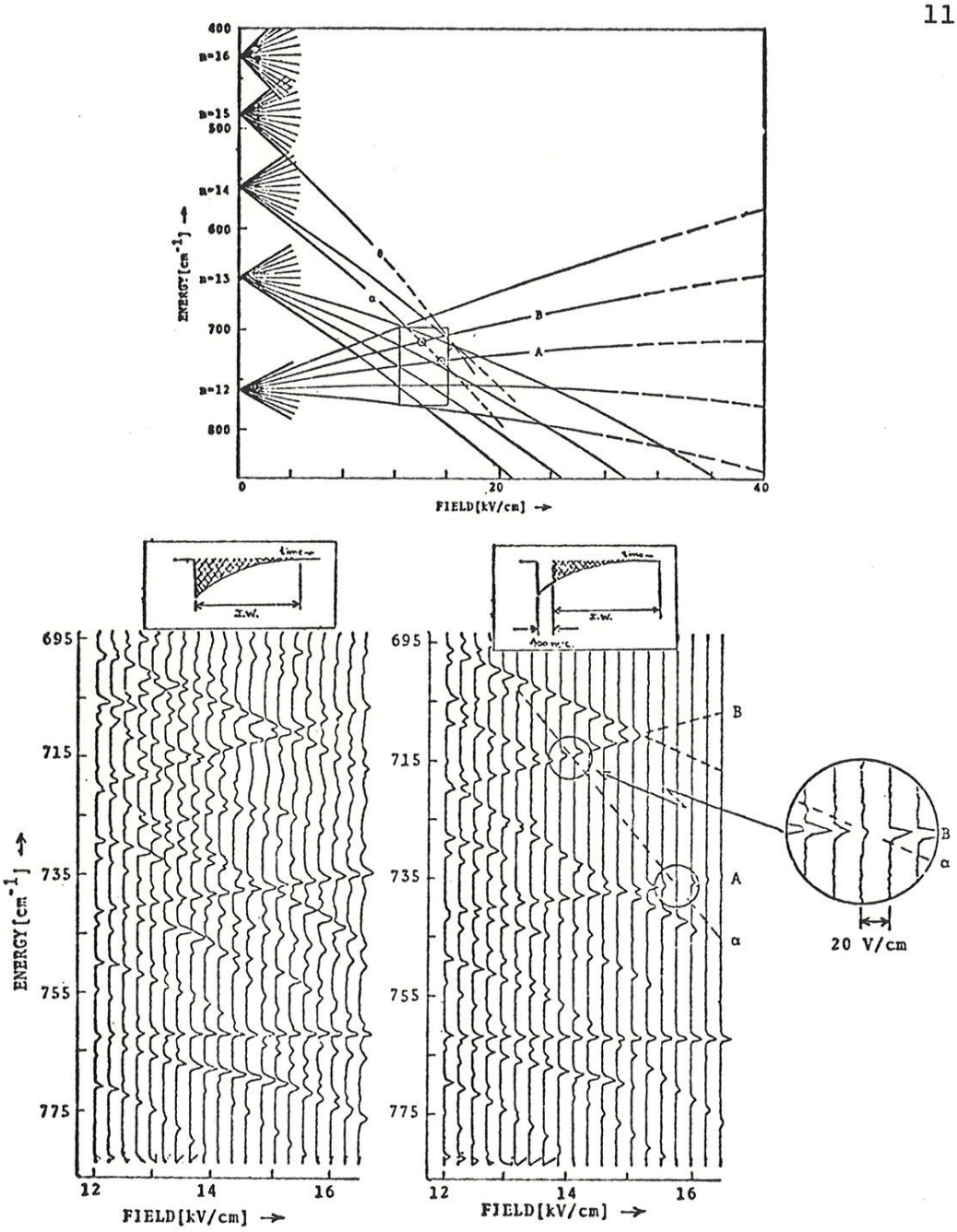

FIGURE IV.4.A-1

(a) Stark structure of the $|m|=2$ states in sodium. The quantum numbers of the states are: A(12,6,3,2); B(12,7,2,2); α(14,0,11,2); θ(15,0,12,2). The dashed lines indicate when levels ionize at rates greater than 10^7 sec^{-1} according to BHR.

(b) Experimental excitation curves for the boxed region above obtained by integrating the ionization signal for all time.

(c) The same as (b) except that the integration window (IW) begins 400 nsec after excitation. The disappearance of a level indicates that the decay rate exceeds 10^7 sec^{-1}.

(d) a scan of the circled region in (c) using finer field steps.

few ions per laser pulse which, we suspect, are produced by Rydberg - Rydberg collisions in the beam. (This is strongly suggested by the fact that the ion signal scales as the square of the blue laser intensity.) The collisionally-produced ions represent only a small fraction of the total excited state decay since the ion signal increases by at least 100-fold when the field is increased to the region where ionization decay predominates. This increase does not show up in the Stark maps, however, since the detector is operated at a gain where only a few ions per excitation pulse results in saturation. The map in Fig. IV.4.A-1b is somewhat more confused than that of the previous experiment because the broadening $|m| = 0$ and 1 levels form a bumpy quasi-continuum background. We have, however, suceeded in identifying the $|m| = 2$ levels and associating them with the hydrogenic parabolic Stark states.

In Fig. IV.4.A-1c the scans of the boxed region in Fig. IV.4.A-1a have been repeated but now we integrate the ion signal starting 400 nsec after excitation. Levels that decay in times less than about 100 nsec do not appear in the data. The map shows directly the field strength at which the ionization rate for a given Stark level exceeds about

10^7 sec^{-1} (ie. the field at which the level disappears). The dashed lines in the data show the position of levels when their decay rates are greater than this value.

The first state that we consider is the lowest $|m| = 2$ component of the $n = 14$ manifold, labelled $\propto$ in Figs. IV.4.A-1a and -1c. The corresponding hydrogenic state is (14, 0, 11, 2) where the level indices are the parabolic quantum numbers n, n_1, n_2, and $|m|$. As we see from the data, peaks which correspond to this state begin to disappear at about 12 kV/cm. After locating the peak which corresponds to the $\propto$ level we used the Stark map to aid in carefully advancing the laser (grating) to the proper channel so that only this particular level was excited. Once the laser was in position the single ion timing spectrometer was used to monitor the decay (see sect. III.4).

A typical timing spectrum is given in Fig. IV.4.A-2. Within experimental error, the observed decay is indeed exponential. The process was repeated for several field values (care was taken to select fields at which no other levels were close enough to be excited). The results are plot-

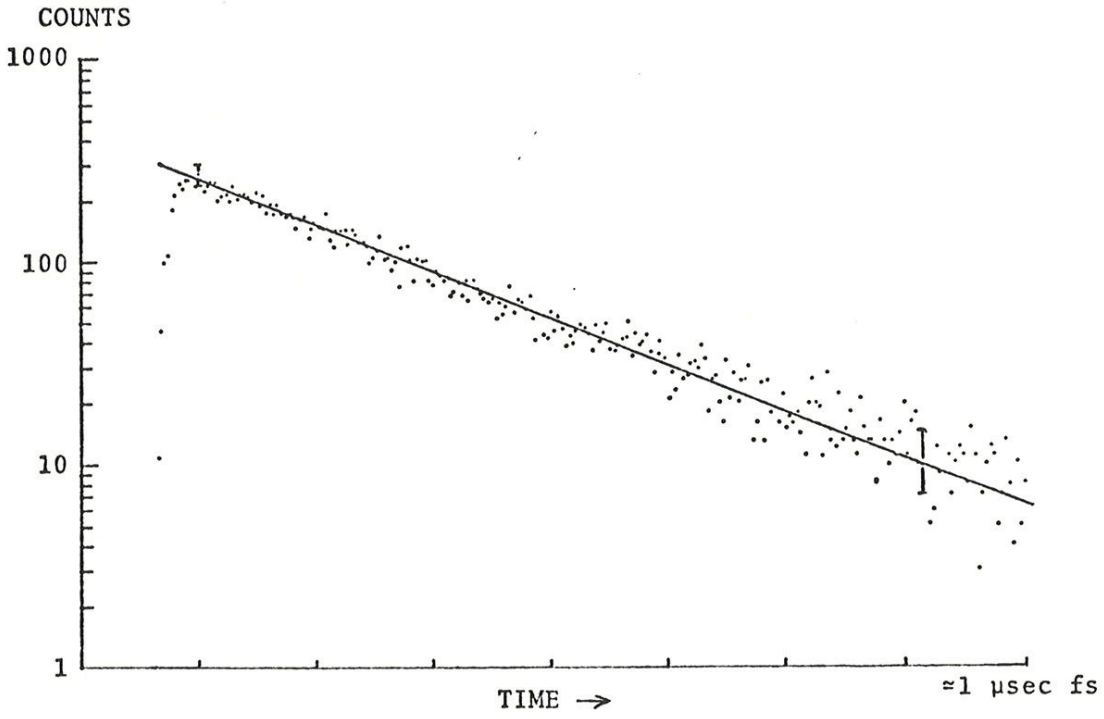

FIGURE IV.4.A-2

Typical timing spectrum illustrating exponential decay.

ted in Fig. IV.4.A-3. The calculations of Bailey, Hiskes and Riviere (BHR) for this level (solid line) are included for comparison (the curve was extrapolated from the published results for the two extreme $|m| = 0$ levels [BAI 65] and the central $|m| = 1$ level [RIV 68]). The slopes of the theoretical and experimental curves agree, and, within the 3% uncertainty in the field calibration, they coincide. To our knowledge, this is the first measurement of the decay rate for a resolved hydrogenic level.

The question arises as to whether our agreement for the ionization rate of the α (14, 0, 11, 2) level of sodium with BHR's results for hydrogen may be simply fortuitous. To investigate the possible role of level mixing, we projected the sodium wavefunction onto a hydrogen basis set for a field of 15.75 kV/cm. The fractional composition of the sodium level in terms of a particular hydrogen level (n, n_1, n_2, 2) is just the square of the overlap integral,

$$\langle n, n_1, n_2, m; F, Na \mid n', n_1', n_2', m; F, H \rangle$$

The hydrogen functions were determined by diagonalizing the hydrogen problem using the same procedures as for sodium.

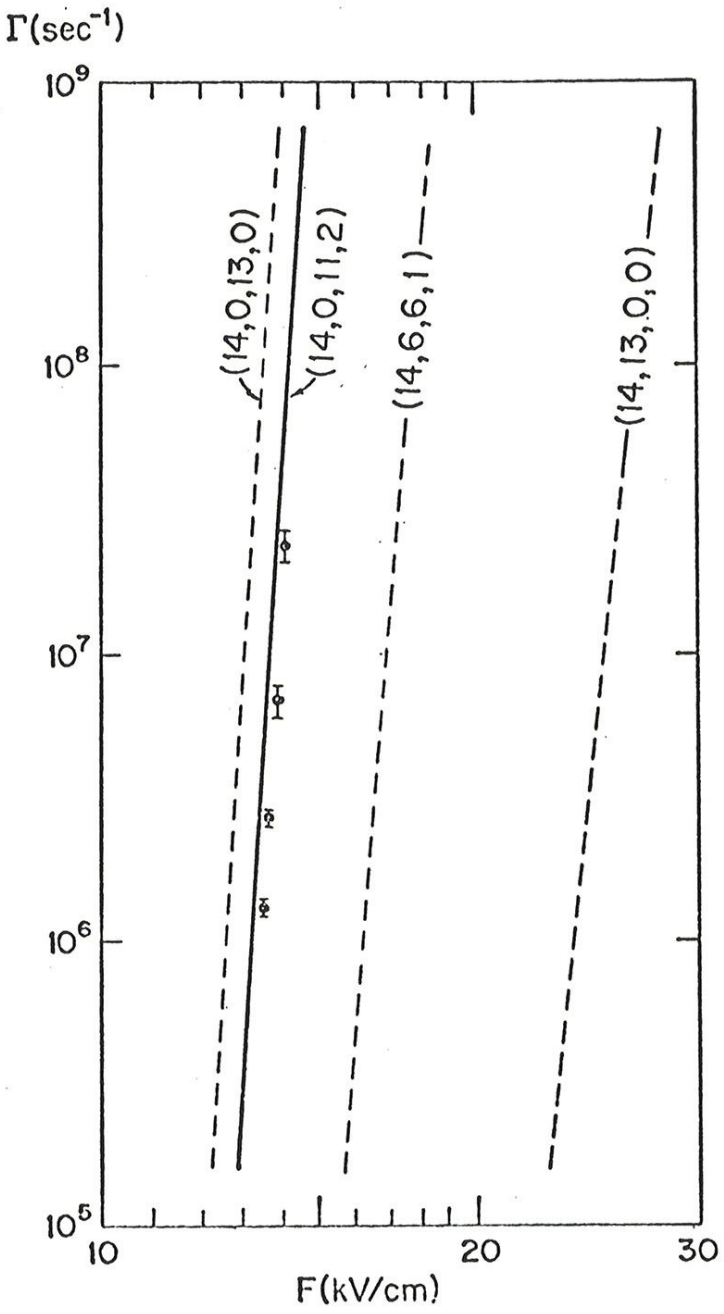

FIGURE IV.4.A-3

Measured ionization rates for the state ∝. The theoretical curve for ∝ (solid) was obtained by extrapolation from rates calculated by BHR for nearby Stark levels (dashed).

Listed in Table IV.4.A-1 is the fractional makeup of the $\propto$ level at a field of 15.75 kV/cm. Because of their large ionization rates the contributions of the higher n states are most likely to lead to differences between the sodium and hydrogen systems. The effect of these terms, however, is negligable since levels with $n \gtrsim 15$ decay at rates $\lesssim 10^{12}$ sec^{-1} (see sect. I.1) and this leads us to believe that the (14, 0, 11, 2) state in sodium is indeed suitable for testing hydrogenic theory.

Our observations of ionization rates for many of the other components of the $|m|=2$ manifold are, however, in serious disagreement with BHR's calculations. The difficulty

TABLE IV.4.A-1

Fractional composition (in %) of the $\propto$(14,0,11,2) sodium level in terms of $|m|=2$ hydrogenic Stark levels.

n_1	n = 10	n = 11	n = 12	n = 13	n = 14	n = 15
00	.000003	.000002	.000034	.000005	99.8942	.000028
01	.000004	.000007	.000017	.000124	.000113	.000033
02	.000006	.000013	.000041	.002713	.000042	.000027
03	.000009	.000020	.000093	.001199	.000022	.000020
04	.000010	.000026	.000223	.000203	.000013	.000013
05	.000010	.000032	.000799	.000078	.000009	.000008
06	.000008	.000034	.092720	.000038	.000005	.000005
07	.000004	.000031	.000759	.000019	.000003	.000003
08		.000020	.000164	.000009	.000002	.000002
09			.000018	.000004	.000001	.000001
10				.000001	.000001	<.000001
11					<.000001	<.000001
12						<.000001

can be seen by comparing the points at which theory predicts rates should exceed 10^{7} sec^{-1}, indicated by dashed lines in Fig. IV.4.A-1a, and where most levels in Fig. IV.4.A-1c actually ionize faster than this rate. It is apparent that most levels ionize at substantially lower fields than expected.

A clue to this early onset of ionization is provided by the circled feature in Fig. IV.4.A-1c. The level A (12, 6, 3, 2) momentarily disappears at a field of 15.75 kV/cm. We ascribe this behaviour to level mixing with the rapidly ionizing state α (14, 0, 11, 2) at the A - α crossing. When the decay rates of the two crossing levels are significantly different, as is the case here, the long lived state is quenched, even if the amount of level mixing is minute (see appendix E). Quenching phenomena of this type have been discussed by Lamb [LAM 52]. Fig. IV.4.A-4 shows data for the ionization rate of state A in the vicinity of the crossing. The theoretical curve in Fig. IV.4.A-4 is calculated using the following expression for the complex energy of the two interacting levels (a derivation of the expression is given in appendix E),

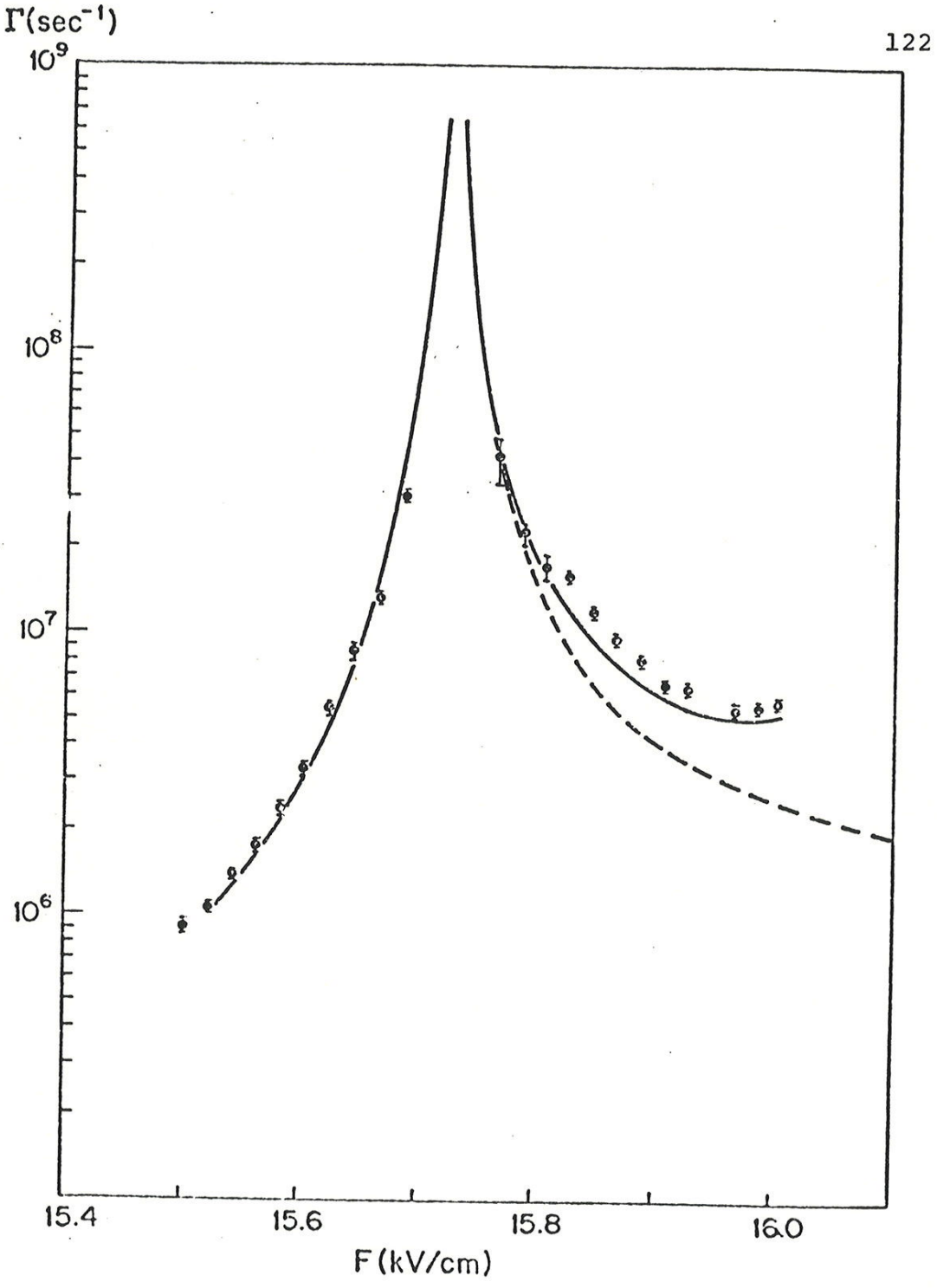

FIGURE IV.4.A-4

Ionization rates for the level A in the region of the A - α crossing. The solid line is the theoretical curve described in the text. The dashed line is calculated neglecting the A - θ crossing at 17.3 kV/cm.

$$E - \tfrac{i}{2}\Gamma = \tfrac{1}{2}\left\{ E_A + E_\alpha - \tfrac{i}{2}(\Gamma_A + \Gamma_\alpha) \pm \sqrt{(E_A - E_\alpha - \tfrac{i}{2}(\Gamma_A - \Gamma_\alpha))^2 + 4|V_{A\alpha}|^2} \right\}.$$

E_A and E_α are the unperturbed energies for the levels, Γ_A and Γ_α are their decay rates, and $V_{A\alpha}$ is the matrix element of $\vec{F} \cdot \vec{r}$ which couples the two states. We have determined $V_{A\alpha}$ by diagonalizing the energy matrix for $|m|=2$ with n ranging from 10 to 15 as discussed in sect. II.5. Its value is 0.05243 cm^{-1}. Note that the minimum separation between the two adiabatic levels is equal to twice $V_{A\alpha}$ (see appendix E). Γ_α, which varies rapidly with F was determined from the results of BHR. At the A - α crossing $\Gamma_\alpha = 10^{10}$ sec^{-1}. (Γ_A, due primarily to radiation, was experimentally determined to be 3×10^5 sec^{-1}. Since $\Gamma_A \ll \Gamma_\alpha$ its value does not need to be known precisely.) A second ionizing level, θ (15, 0, 12, 2) (see Fig. IV.4.A-1a), crosses level A at 17.3 kV/cm and was included in the calculation, assuming that the A - α and A - θ crossings were independent.

Another instance of quenching is to be found at the B - α crossing. Careful examination of this crossing, however, in Fig. IV.4.A-1c reveals no evidence of quenching. By rescanning this region (see Fig. IV.4.A-1d) and using a finer

field step, the quenching effect becomes evident. As before, the level disappears due to level mixing, but since the ionization rate of the rapidly ionizing level (Γ_α = 10^9 sec^{-1}) is much less than that at the A - α crossing while the coupling matrix element between the Stark levels is about the same as at that crossing, the quenching is much less pronounced.

The sharp increase in the ionization rate at level crossings offers insight into the premature ionization of the other levels in Fig. IV.4.A-1c. If crossings occur with a series of broad levels and if the coupling matrix elements are large then the ionization rate never returns to the value for the isolated level. Levels are effectively coupled into the continuum in a manner similar to that of autoionizing states.

Current hydrogenic tunneling theory does not predict quenching at level anti-crossings. Approximation methods which treat this problem by expansion techniques (such as the Lanczcs and RG methods) are not substantially improved by carrying out expressions to higher orders in the field

since the energy relation does not converge at the point of closest approach between levels. (At the point where the levels would cross in the absense of coupling the identity of the states is exchanged thus causing the energy to be discontinuous.) One method which has been proposed to account for the level quenching requires that one diagonalize the complex energy matrix where the ionization rates of the basis states at a given field are included phenomenologically with the energy before the matrix is diagonalized. This method would allow one to include the coupling effects of many nearby levels without having to make the assumption that crosssings are independent. In this manner one could predict the ionization rates for systems where the coupling is sufficiently strong that many levels contribute to the quenching, as is the case for the $|m| = 0$ and 1 levels in sodium. The main problem that must be solved before this method can be implemented is, how to calculate the ionization rates corresponding to the unperturbed basis states in a given field. More theoretical work on this problem is warranted.

A question that has emerged is, what does all this mean in terms of ionization in hydrogen? For the

non-relativistic problem it remains to be determined whether different Stark levels anti-cross (ie. mix) or not. According to our diagonalization procedure, Stark levels in hydrogen have been found to exhibit avoided crossings (eg. for n=12, $|m|=2$ the size of the repulsion is on the order of 0.001 cm^{-1} or less), however, this may be an artifact of the truncated basis set used in the diagonalization [HAT 76, HER 76]. Although non-relativistic hydrogenic Stark states may actually cross, the spin-orbit coupling and other relativistic effects serve to break the l degeneracy which results in avoided crossings. As a result the observed quenching phenomenon in sodium are also expected to be present in hydrogen.

IV.4.B Line Broadening Measurements of the Decay Rate

Here we use the line broadening method for determining ionization rates. As described earlier, the decay rate of a given level can be inferred from the excitation linewidth provided that the level width is larger than the laser width, 0.5 cm^{-1}. The experimental procedure is straightforward. We scan the laser over a 100 cm^{-1} range and record the total ionization signal. The process is repeated with different applied fields so that the functional dependence of the ionization rate with field can be determined. Using this method, we have mapped the region indicated in the box in Fig. IV.4.B-1a. The results are shown in Fig. IV.4.B-1b. The blue laser is polarized perpendicularly to the field axis and the $|m|=2$ levels are identified by their parabolic quantum numbers. At these fields all of the levels ($|m| = 0$, 1, and 2) ionize at rates greater than 10^8 sec^{-1} so that the direct timing method cannot be applied. At 17 kV/cm one observes that the (15, 6, 6, 2) level disappears from view, presumably because it has become broad. (Note that the level disappearance here is not due to the manner in which we integrate the ion signal, as was the case in the preceeding experiment.)

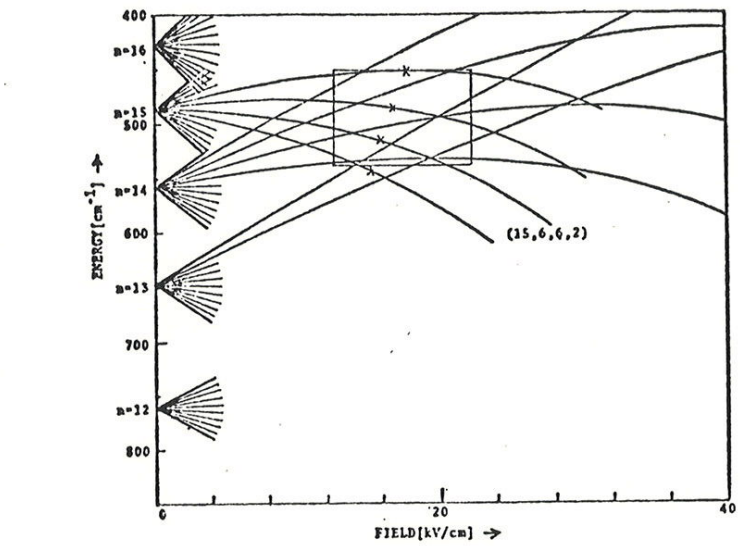

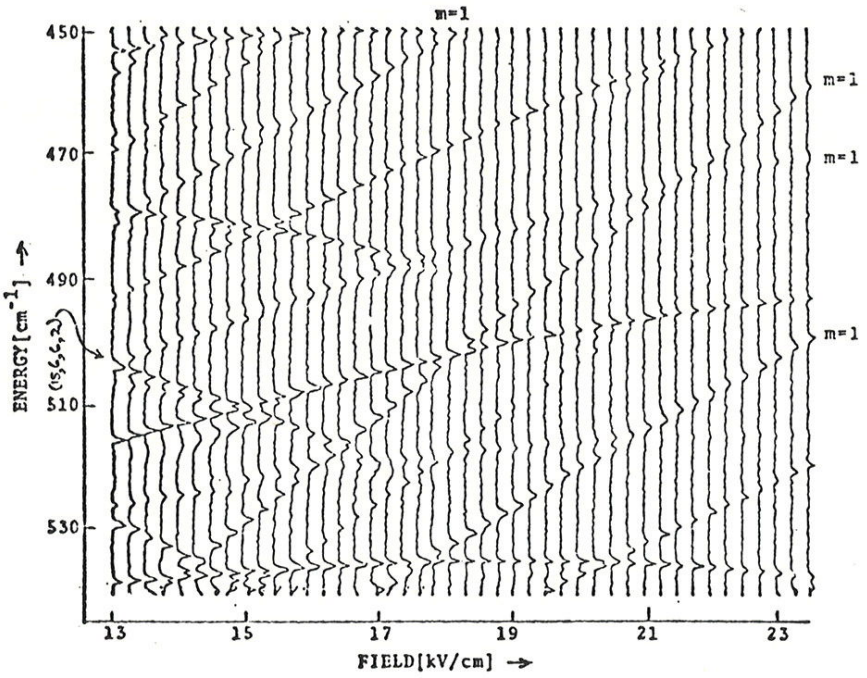

FIGURE IV.4.B-1

(a) Stark structure of the $|m|=2$ levels in sodium.
(b) Experimental excitation curves for the boxed region above obtained by scanning the blue laser and integrating the ionization signal for all time. The $|m|=1$ levels are indicated to avoid confusion with the levels of interest (ie. $|m|=2$).

We tried unsuccessfully to observe line broadening of of the (15, 6, 6, 2) level as the applied field was increased. Unfortunately the quasi-continuum background, due to the $|m| = 0$ and 1 states, obscured the level enough that only a decrease in amplitude was observed. Many attempts were made to examine the narrow field region where other $|m|=2$ levels disappear, but we were unsuccessful in obtaining any clear evidence of level broadening. Even though we were not able to obtain a measurement of the ionization rates of $|m|=2$ levels the mere fact that the linewidths are less than or equal to the laser width up to the field at which they disappear, sets an upper limit as to their ionization rate, $\Gamma_{ion} \lesssim 10^{11}$ sec^{-1}. It is interesting to note that the levels disappear at fields near those predicted by BHR for a decay rate of 10^{11} sec^{-1} (indicated by crosses in Fig. IV.4.B-1a). While this suggests crude verification of BHR's calculations for large ionization rates it is still far from conclusive and more experimental work on this problem is warranted.

To verify that levels do indeed broaden, we include data taken in a field region where m = 0 levels are rapidly ionizing (see Fig. IV.4.B-2). The rate at which the level, that is indicated by an arrow, ionizes is about 5×10^{11}

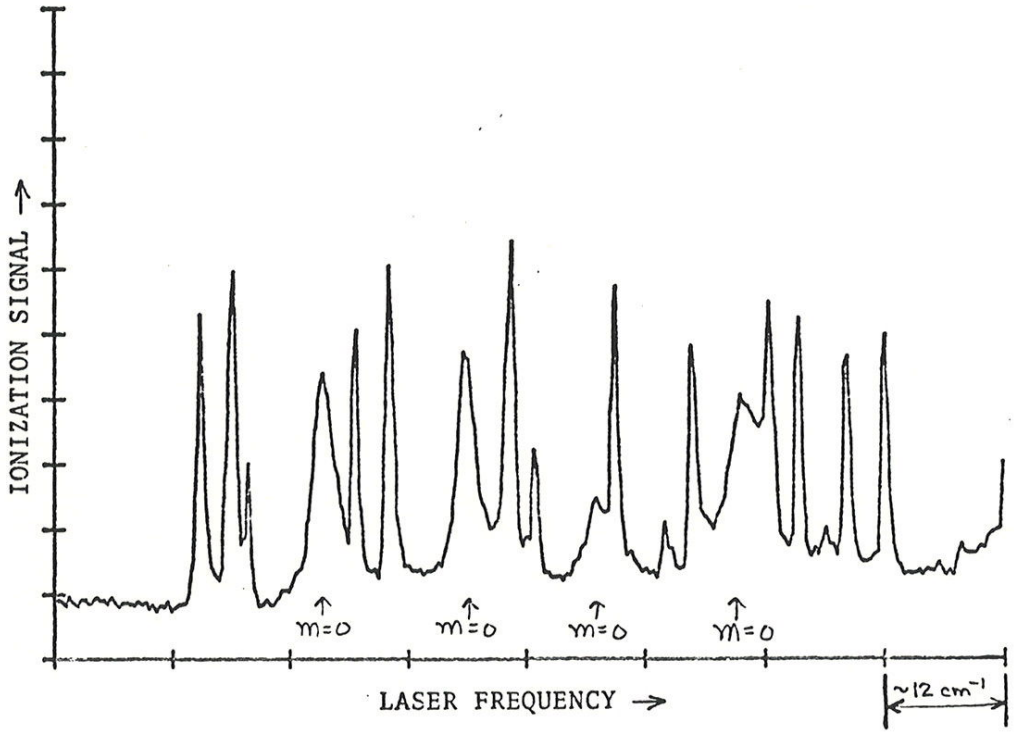

FIGURE IV.4.B-2

Excitation curves taken in a strong static field showing broadening of the m=0 levels. The $|m|=1$ and 2 levels have a width equal to that of the laser. The ionization rates of the broad levels are about 5×10^{11} sec^{-1}.

sec^{-1}. At higher fields these levels are so broad that they do not appear to be resonant.

The line broadening technique has great potential for permitting measurements of ionization rates if narrower linewidth lasers are used. For example, by using currently available cw lasers (10 MHz nominal linewidth) rates greater than 10^8 sec^{-1} could be measured, thus greatly extending the the usefulness of this method.

CONCLUSION

Here we review some of our more important findings. First, it has been demonstrated that by means of stepwise laser excitation, all Stark levels can be populated providing that excitation is permitted by the m selection rules. Second, field ionization has been found to be an efficient and sensitive method for detecting excited state atoms. Third, pulsed field ionization was observed to be characterized by a threshold behaviour which suggests that transitions between different Stark levels can be detected by differential ionization (ie. only one of the two levels is ionized) and also suggests that final state analysis can be performed where many Stark levels are present. Fourth and most important, ionization rates of selected high Rydberg ($|m|=2$) levels have been measured for the first time and quite unexpectedly we found that most Stark levels spontaneously ionize at much lower fields than predicted by hydrogen theory. The discrepancy has been traced to level mixing with rapidly ionizing states. This last result is particularly surprising since the energies of the $|m|=2$ sodium Stark levels are, for most purposes, identical with those of hydrogen. Evidently the minute amount of level mixing, which has been

ignored in earlier works, can actually dominate the field ionization process.

If there is a moral to this work, it is that care should be exercised when theory is extended beyond its region of validity, and, when possible, such extentions ought to be thoroughly checked by experiment.

APPENDIX A

A.1 Evaluation of Dipole Matrix Elements for Sodium

In this section we evaluate matrix elements of the form,

$$\langle n\ell m | z | n'\ell'm' \rangle$$

$$|n\ell m\rangle = R(r)\, Y_{\ell m}(\theta, \varphi)$$

where $|n\ell m\rangle$ are the sodium wavefunctions, $Y_{\ell m}$ are the spherical harmonics, and R(r) is the radial wavefunction. Since $z = r\cos\theta$ we can simply perform the angular integrations [BET 57, p. 253],

$$\left.\begin{aligned} z^{n'l+1m}_{nlm} &= \sqrt{\frac{(l+1)^2-m^2}{(2l+3)(2l+1)}}\, R^{n'l+1}_{nl}, \\ z^{n'l-1m}_{nlm} &= \sqrt{\frac{l^2-m^2}{(2l+1)(2l-1)}}\, R^{n'l-1}_{nl}, \\ z^{n'l'm}_{nlm} &= 0 \quad \text{for all other } l', \end{aligned}\right\}$$

$$R^{n'l'}_{nl} = \int R_{n'l'}(r)\, R_{nl}(r)\, r^3\, dr.$$

where $R^{n'l'}_{nl}$ is the radial integral. To determine R(r) we begin by examining the equation that it must satisfy [BET 57, eq. 2.5],

$$R(r) = e^{-\epsilon r} f(r)$$

$$\epsilon = \sqrt{-2E_{nl}}$$

$$f'' + 2\left(\frac{1}{r} - \epsilon\right) f' + \left[2\left(\frac{1-\epsilon}{r}\right) - \frac{l(l+1)}{r^2}\right] f = 0 \qquad (A\text{-}1).$$

Note that since the potential outside of the core is Coulombic we solve the hydrogen equation in the region $r > r_c$. Unlike the hydrogen problem, however, the energies of the sodium states are known so that E_{nl} cannot be treated as a free parameter. We follow the procedure used by Zimmerman and express f in terms of a series expansion,

$$f(r) = r^{\lambda} \sum_{\nu=0}^{\infty} a_{\nu} r^{-\nu}$$

The expression for f differs from the usual one in that as the index increases, the power of r decreases. This is done with the knowledge that for Coulombic wavefunctions the series expansion must terminate for some power of r to ensure that the wavefunction be finite at $r = +\infty$. We substitute the expression for f into eq. A-1 and obtain the following recursion relation for the coefficients,

$$a_{\nu+1} = - a_{\nu} \frac{\left(\frac{1}{\epsilon} - \nu - 1\right)\left(\frac{1}{\epsilon} - \nu - 2\right) + 2\left(\frac{1}{\epsilon} - \nu - 1\right) - \ell(\ell+1)}{2\epsilon(\nu+1)} ,$$

where we have substituted $1/\epsilon - 1$ for λ according to the indicial equation. The series is arbitrarily cut off before any terms in r^{-q} for $q > 0$, occur. (The error made in terminating the series in such a manner is small providing that $r > r_c$.) If we substitute the solution for r in the radial integral we obtain,

$$R_{n\ell}^{n'\ell'} = \int_0^\infty e^{-\left(\frac{1}{n}+\frac{1}{n'}\right)r}\; r^{n+n'+1} \sum_{\nu=0}^{n-|m|-1} \sum_{\nu'=0}^{n'-|m|'-1} a_\nu\, a_{\nu'}\, r^{-\nu-\nu'}\, dr$$

which is best rewritten as,

$$R_{n\ell}^{n'\ell'} = \left(\sum_{\nu} \sum_{\nu'} G_{\nu\nu'} \right) \frac{\Gamma(2+n+n')}{\left(\frac{1}{n}+\frac{1}{n'}\right)^{2+n+n'}}$$

where,

$$\Gamma(n) = \int_0^\infty e^{-x}\, x^{n-1}\, dx$$

$$G_{\nu\nu'} = G_{\nu,\nu'-1}\left(-\frac{n}{2}\left(\frac{1}{n}+\frac{1}{n'}\right)\right) \frac{(n'-\nu'-\ell')(n'-\nu'+\ell'+1)}{\nu'(n+n'+2-\nu-\nu')}$$

$$G_{\nu\nu'} = G_{\nu-1,\nu'}\left(-\frac{n'}{2}\left(\frac{1}{n}+\frac{1}{n'}\right)\right) \frac{(n-\nu-\ell)(n-\nu+\ell+1)}{\nu(n+n'+2-\nu-\nu')} \quad .$$

The last step is done so that computer roundoff errors are minimized in summing the terms for large n. At this point the problem is turned over to the computer using double precision (14 significant digits). This method is limited by computer round-off error to values of n less than 20.

A.2 Computer Programs

```
      FUNCTION RADMAT(IP,N1,N2,L1,L2,QD1,QD2)
C*******TERMINATES THE SERIES BY (N-L-QD) INSTEAD OF (N-L)  9/10/76 MLZ
C.......     "RADMAT" CALCULATES RADIAL MATRIX ELEMENTS TO ANY POWER OF R
C.......BETWEEN ANY TWO COULOMBIC STATES.  NONHYDROGENIC ENERGIES
C.......MAY BE SPECIFIED BY GIVING APPROPIATE QUANTUM DEFECTS.
C.......SINCE THE OUTER B.C.  IS MATCHED (AS COMPARED TO THE STANDARD
C.......TECHNIQUE OF MATCHING THE INNER B.C.) FOR THE FIRST TERM IN
C.......THE SERIES AND THE SERIES IS TERMINATED AS IF IT WAS HYDROGEN,
C.......IT SHOULD GIVE GOOD ESTIMATES OF MATRIX ELEMENTS FOR POSITIVE
C.......POWERS OF R.
C.......  <N1,L1!R**IP!N2,L2>  M.Z.  HAS DERIVATION OF THE ALGORITHIM
C.......  IP            =POWER OF R DESIRED
C.......  N1,L1,N2,L2    =N AND L QUANTUM NUMBERS FOR STATE 1 AND 2
C.......  QD1,QD2        =QUANTUM DEFECT FOR STATE 1 AND 2
C.......SET UP SOME USEFUL CONSTANTS
      A1=N1-QD1
      A2=N2-QD2
C.......CALL "RADIAL" TO DO THE DOUBLE SUM - MUST ALSO DO NORMILAZATION
      TMP=RADIAL(L1,L1,A1,A1,0)*RADIAL(L2,L2,A2,A2,0)
      TMP=1./TMP
      RADMAT=RADIAL(L1,L2,A1,A2,IP)
C.......EVALUATE THE THREE GAMMA FUNCTION (GET DOWN TO RANGE 2.->1.)
      A=1./A1+1./A2
      B=2./A1
      C=2./A2
      X=A1+A2+IP+1
      Y=2.*A1+1
      Z=2.*A2+1
   10 IF(X.LT.2.) GOTO 20
      X=X-1.
      TMP=TMP/A/A*X*X
   20 IF(Y.LT.2.) GOTO 30
      Y=Y-1.
      TMP=TMP*B/Y
   30 IF(Z.LT.2.) GOTO 40
      Z=Z-1.
      TMP=TMP*C/Z
   40 IF(X.GE.2..OR.Y.GE.2..OR.Z.GE.2.) GOTO 10
      TMP=TMP/GAMMA(Y)/GAMMA(Z)*B**Y*C**Z
      RADMAT=RADMAT*SQRT(TMP)*GAMMA(X)/A**X
      RETURN
      END
```

```
      FUNCTION RADIAL(L1,L2,ZN1,ZN2,IP)
C
C.....*RADIAL* EVALUATES THE DOUBLE SUM FOR *RADMAT*     9/9/76
C
      IMPLICIT REAL*8 (A-H)
      F(K,A,L)=-.5*AQ*A*(A-K-L)*(A-K+L+1)/K/(AX-I-J)
C.....INITIALIZE
      AN1=ZN1
      AN2=ZN2
      AX=AN1+AN2+IP+1
      AQ=1./AN1+1./AN2
      N1=ZN1-L1+.5
      N2=ZN2-L2+.5
      AS1=0.
      AS2=0.
C.....HERE WE DO THE SUM
      DO 40 I1=1,N1
      BSIDE=0.
      I=N1-I1
      DO 10 J1=1,N2
      J=N2-J1
      IF(J.EQ.0) GOTO 20
10    BSIDE=F(J,AN2,L2)*(BSIDE+1.D+00)
20    IF(I.NE.0) GOTO 30
      RADIAL=AS1+AS2+BSIDE+1.D+00
      RETURN
30    AT=F(I,AN1,L1)
      AS1=AT*(AS1+1.D+00)
40    AS2=AT*(AS2+BSIDE)
      END
```

```
      FUNCTION GAMMA(ARG)
C.....      THIS FUNCTION CALCULATES THE GAMMA FUNCTION FOR ARGUMENTS
C.....IN THE RANGE 37 -> 0  (REALLY 1.E-20).  A ZERO IS RETURNED IF ARG
C.....IS OUTSIDE THIS RANGE.
C.....   THE COEFFICIENTS ARE FROM THE "HANDBOOK OF MATHEMATICAL FUNCTIONS"
C.....EDITED BY MILTON ABRAMOWITZ AND IRENE STEGUN.
      DATA C01 / 1.0E0/
      DATA C02 / 5.7721566490153?9E-01/
      DATA C03 /-6.5578071520253?E-01/
      DATA C04 /-4.2002635034095?E-02/
      DATA C05 / 1.6653861138229?5E-01/
      DATA C06 /-4.2197734555544?E-02/
      DATA C07 /-9.6219715278??E-03/
      DATA C08 / 7.2189432466?3E-03/
      DATA C09 /-1.1651675918591E-03/
      DATA C10 /-2.1524167411?9E-04/
      DATA C11 / 1.2805028238?2E-04/
      DATA C12 /-2.0134854780?E-05/
      DATA C13 /-1.2504934821E-06/
      DATA C14 / 1.1330272?2E-06/
      DATA C15 /-2.0563384?7E-07/
      DATA C16 / 6.116095E-09/
      DATA C17 / 5.0020075E-09/
      DATA C18 /-1.1812746E-09/
      DATA C19 / 1.043427E-10/
      DATA C20 / 7.7823E-12/
      DATA C21 /-3.6968E-12/
      DATA C22 / 5.1E-13/
      DATA C23 /-2.06E-14/
      DATA C24 /-5.4E-15/
      DATA C25 / 1.4E-15/
      DATA C26 /1.0E-16/
C.....CHECK ARGUMENT LEGALITY
      GAMMA=0.
      IF(ARG.GT.37.0.OR.ARG.LT.1.0E-20) RETURN
C.....SET UP --- SPECIAL CASE IF ARG LESS THEN 1
      GAMMA=C01
      X=ARG
      IF(X.GE.C01) GOTO 10
      GAMMA=GAMMA/X
      GOTO 30
C.....LOOP TILL X IS IN THE RANGE 1 TO 2
   10 IF(X.LT.2.0) GOTO 20
      X=X-C01
      GAMMA=GAMMA*X
      GOTO 10
C.....NOW EVALUATE
   20 X=X-C01
   30 TMP=C19+X*(C20+X*(C21+X*(C22+X*(C23+X*(C24+X*(C25+X*C26))))))
      TMP=C12+X*(C13+X*(C14+X*(C15+X*(C16+X*(C17+X*(C18+X*TMP))))))
      TMP=C05+X*(C06+X*(C07+X*(C08+X*(C09+X*(C10+X*(C11+X*TMP))))))
      GAMMA=GAMMA/(C01+X*(C02+X*(C03+X*(C04+X*TMP))))
      RETURN
      END
```

APPENDIX B

VOLUME 35, NUMBER 26 PHYSICAL REVIEW LETTERS 29 DECEMBER 1975

Observation of Oscillations in Resonance Absorption from a Coherent Superposition of Atomic States*

Theodore W. Ducas, Michael G. Littman, and Myron L. Zimmerman
Research Laboratory of Electronics and Department of Physics, Massachusetts Institute of Technology, Cambridge, Massachusetts 02139
(Received 10 November 1975)

A technique is described for high-resolution spectroscopy using resonance absorption from a laser to monitor the time evolution of a coherently excited superposition of atomic states. As a demonstration a measurement was made of the $3^2P_{1/2}$ hyperfine splitting in sodium.

We have used resonant absorption to monitor the time evolution of a coherent superposition of atomic states, providing a measure of closely spaced structure. A pulsed tunable dye laser prepared a superposition of the two hyperfine components of the sodium $3^2P_{1/2}$ level. Modulations at the hyperfine frequency in the transition rate to a high $n^2S_{1/2}$ level were observed as a function of the delay of a second pulsed laser.

Both this method and quantum beat spectroscopy (QBS),[1-4] where the modulations of the coherent superposition state are observed in fluorescent decay, eliminate the Doppler width as a spectroscopic limit. In contrast to QBS, probing the modulations by resonant absorption allows structure to be measured in levels whose radiative decay is either difficult to observe or improbable (as in metastable levels). Furthermore with short laser pulses, better resolution can be achieved than that obtained in those QBS fluorescence techniques which depend upon the timing characteristics of photon detectors. This method (using picosecond lasers) can have resolution comparable to beam-foil spectroscopy,[4] while providing the additional feature of state-selective laser excitation.

Figure 1 shows the relevant energy levels in Na^{23}, where $\Delta\omega$ is the separation between the $F=2$ and $F=1$ hyperfine components of the $3^2P_{1/2}$ level. Here $\vec{F}$ ($\vec{F}=\vec{I}+\vec{J}$) is the total angular momentum, $\vec{I}$ is the nuclear spin angular momentum ($I=\frac{3}{2}$), and $\vec{J}$ is the electronic angular momentum ($J=\frac{1}{2}$). A laser pulse, tuned to the $3^2S_{1/2}-3^2P_{1/2}$ transition with a duration $\Delta t \ll 2\pi/\Delta\omega$, will excite a coherent superposition of the two hyperfine components of the $3^2P_{1/2}$ level. The bold sublevels in Fig. 1(a) illustrate the creation of a coherent superposition state of the $F=2, m_F=0$ and $F=1, m_F=0$ sublevels by a right-hand-circularly-polarized (rhcp) laser pulse. This state can be written as

$$\psi(t)=[a|1,0\rangle \exp(-i\omega_1 t)+b|2,0\rangle \exp(-i\omega_2 t)]\exp(-t/2\tau), \tag{1}$$

where $\hbar\omega_1$ and $\hbar\omega_2$ are the energies of the $F=1$ and $F=2$ levels, respectively, a and b are time-independent constants, and τ is the radiative lifetime of the $3^2P_{1/2}$ level ($\tau \approx 16$ nsec[5]).

It is convenient to transform to a product representation, $|I,m_I\rangle|J,m_J\rangle$ [see Fig. 1(b)].[6] In this representation the state in Eq. (1) can rewritten as

$$\psi(t)=[c\sin(\tfrac{1}{2}\Delta\omega t)|\tfrac{3}{2},+\tfrac{1}{2}\rangle|\tfrac{1}{2},-\tfrac{1}{2}\rangle+d\cos(\tfrac{1}{2}\Delta\omega t)|\tfrac{3}{2},-\tfrac{1}{2}\rangle|\tfrac{1}{2},+\tfrac{1}{2}\rangle]\exp[-\tfrac{1}{2}i(\omega_1+\omega_2)t]\exp(-t/2\tau), \tag{2}$$

where c and d are constants. The hyperfine coupling is manifest in the coefficients of the product wave function which oscillate with a characteristic frequency of the hyperfine splitting. At $t=0$, $\psi(t)$ is entirely $m_J=+\frac{1}{2}$ in character; at $t=\pi/\Delta\omega$ it has evolved to be completely $m_J=-\frac{1}{2}$ in nature. These oscillations can be monitored by resonant absorption of a short pulse of light ($\Delta t \ll 2\pi/\Delta\omega$) to a still higher $n^2S_{1/2}$ level. This is illustrated in Fig. 1(b) where the probe laser is rhcp. The population of the $n^2S_{1/2}$ level is a measure of the $m_J=-\frac{1}{2}$ character of this intermediate level. We have considered only a single set of sublevels; for a complete analysis we must consider all sublevels connected by the successive excitations. For the case where both the preparation and probe lasers have the same sense of circular polarization the $n^2S_{1/2}$ population is

$$N_{\text{same}}=A\sin^2(\tfrac{1}{2}\Delta\omega t)e^{-t/\tau}, \tag{3}$$

where t is the delay time between the two laser pulses. If the lasers have the opposite sense of

VOLUME 35, NUMBER 26 PHYSICAL REVIEW LETTERS 29 DECEMBER 1975

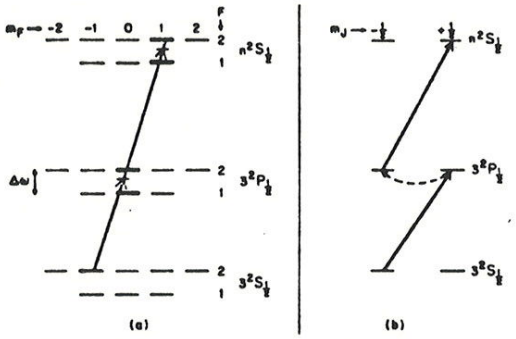

FIG. 1. Energy level diagram for relevant levels in sodium (a) as viewed in the $|F,m_F\rangle$ representation and (b) bold levels as viewed in the $|I,m_I\rangle|J,m_J\rangle$ product representation.

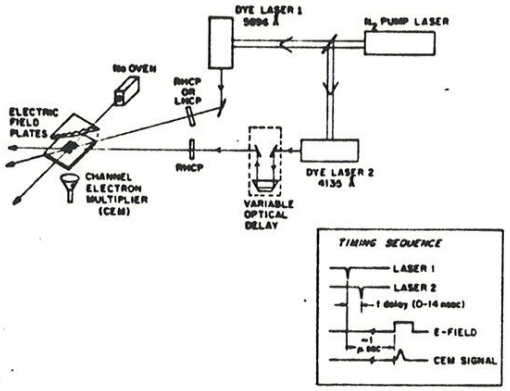

FIG. 2. Schematic diagram of experimental arrangement. Also shown is the timing sequence of laser excitation and electric field ionization.

circular polarization, the population is

$$N_{\text{opp.}} = A[\cos^2(\tfrac{1}{2}\Delta\omega t) + \tfrac{5}{8}]e^{-t/\tau}. \quad (4)$$

A schematic of the experimental apparatus is shown in Fig. 2. The primary features of the arrangement include two pulsed lasers with variable delay time with respect to each other, an atomic beam source, and a detector of the highly excited Na atoms which uses electric field ionization.[7]

The two pulsed tunable dye lasers were pumped by a common N_2 pulsed uv laser. Laser 1 was tuned to the $3^2S_{1/2} - 3^2P_{1/2}$ transition in sodium at 5896 Å. Laser 2 was tuned to $3^2P_{1/2} - 20^2S_{1/2}$ transition at 4135 Å. Both lasers exhibited peak powers of approximately 100 W, pulse widths of 2 nsec, and spectral widths of about 0.5 cm^{-1}. The low peak power of the lasers was the direct result of making the laser cavities as long as possible in an attempt to reduce the pulse width of the lasers. The pulse width of the lasers was the primary limitation on resolution.

The oscillation period was in the nanosecond regime and a variable optical path length provided a convenient way of accurately delaying the second laser pulse with respect to the first. The delay line consisted of a laser collimator, a long (7 ft) optical bench, and a "roof" prism. Delays as long as 14 nsec were readily obtained, allowing us to observe two cycles in the resonance oscillations of the $3^2P_{1/2}$ level. The collimator served to maintain the image size as the delay was changed.

The light from laser 2 was always rhcp, and the light from laser 1 could be made either rhcp or lhcp. The two nearly collinear laser beams intersected the atomic beam between electric field plates.

The Na atomic beam provided a density of 10^8–10^{10} atoms/cm^3 in the interaction region. The background pressure in the apparatus was 10^{-6} Torr. The number of atoms in the $20^2S_{1/2}$ level was measured by an ionization detector. Approximately 1 μsec after the lasers excited the $20^2S_{1/2}$ level in a field-free region, a 4 kV/cm electric field pulse was applied which ionized all atoms in the $20^2S_{1/2}$ state, but none in the $3^2P_{1/2}$ state. The average number of ions for about twenty laser pulses was monitored by a channel electron multiplier followed by a gated integrator.

The population of the $20^2S_{1/2}$ level was monitored versus the delay of laser 2 with respect to laser 1. Data for N_{same} and $N_{\text{opp.}}$ were recorded for delays in 0.5-nsec steps. By taking the ratio $N_{\text{same}}/N_{\text{opp.}}$, errors due to variations in photon flux, and atomic-beam flux were reduced. From Eqs. (3) and (4), for short laser pulses ($\Delta t \ll 2\pi/\Delta\omega$) the ratio is given by

$$\frac{N_{\text{same}}}{N_{\text{opp.}}} = \frac{\sin^2\tfrac{1}{2}\Delta\omega t}{\tfrac{5}{8} + \cos^2\tfrac{1}{2}\Delta\omega t}. \quad (5)$$

Figure 3 shows data from a typical run. The error bar shown represents the limit of error due primarily to fluctuations in the laser intensity. The data were least-squares fitted with the above expression modified for the finite length of the laser pulse. The total system response

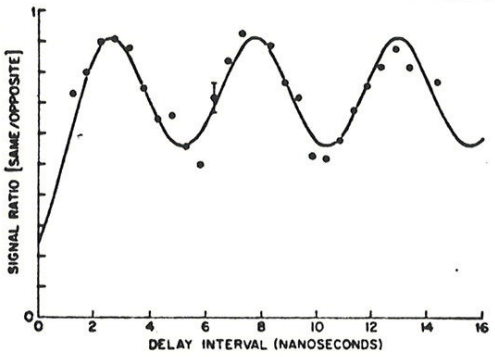

FIG. 3. Experimental results. The points plotted are the ratios of signals for same sense to opposite sense excitation versus delay between preparing and probing laser. The smooth curve is the least squares fit to the data (see text).

function in this case is the convolution of the time profile of the preparing laser with the profile of the probe laser. Thus the population of the $20^2S_{1/2}$ level in time is the convolution of this system response function with Eqs. (3) and (4) for the cases of same and opposite polarization, respectively. We modeled each of the laser pulses with a square-shaped function. The value for the hyperfine frequency for the $3^2P_{1/2}$ state in sodium was found to be 190(5) MHz. This measurement is in excellent agreement with previous experimental determinations of this quantity.[8-10]

We have shown the feasibility of measuring closely spaced structure using resonant absorption from a coherent superposition state. Sodium was studied for experimental convenience, and the $3^2P_{1/2}$ hfs was chosen because it was the simplest structure to analyze. Although we used an atomic beam, this experiment could easily have been performed in a cell with comparable precision since the technique eliminates Doppler broadening and leaves only the natural linewidth as a spectroscopic limit.

In addition to its applications in atomic spectroscopy, this technique can be used to great advantage in studying molecules because it does not depend upon the observation of fluorescence. This reduces problems encountered in molecular levels with many possible channels of radiative decay, and may allow investigation of systems which decay nonradiatively. These are just some examples of how the use of pulsed radiation to probe the resonance oscillations of coherently excited states can provide a means of measuring structure in systems not amenable to other spectroscopic methods.

We would like to thank Dr. Richard R. Freeman for his many helpful suggestions concerning this work.

---

*Work supported by the U. S. Air Force Office of Scientific Research (Contract No. F44620-72-C-0057).

[1]S. Haroche, J. A. Paisner, and A. L. Schawlow, Phys. Rev. Lett. 30, 948 (1973).

[2]W. Gornik, D. Kaiser, W. Lange, J. Luther, and H. H. Schulz, Opt. Commun. 6, 948 (1972).

[3]A. Corney and G. W. Series, Proc. Phys. Soc., London 83, 207 (1964).

[4]H. J. Andrä, Phys. Rev. Lett. 25, 325 (1970).

[5]W. L. Wiese, *Atomic Transition Probabilities*, U. S. National Bureau of Standards, National Standards Reference Data Series—4 (U.S. GPO, Washington, D.C. 1966), Vol. 1.

[6]For excitation rapid compared to the hyperfine period, and slow compared to the fine-structure period, the electric dipole selection rule for rhcp excitation is $\Delta m_j = +1$.

[7]T. W. Ducas, M. G. Littman, R. R. Freeman, and D. Kleppner, Phys. Rev. Lett. 35, 366 (1975).

[8]M. L. Perl, I. I. Rabi, and B. Senitzky, Phys. Rev. 98, 611 (1955).

[9]T. W. Hänsch, I. S. Shahin, and A. L. Schawlow, Phys. Rev. Lett. 27, 707 (1971).

[10]H. T. Duong, P. Jacquinot, S. Liberman, J. L. Picque, J. Pinard, and J. L. Vialle, Opt. Commun. 7, 371 (1973).

APPENDIX C

C.1 The Grating Position Controller

We describe here the grating angle controller which is used to allow computer selection of laser frequency. The grating is mounted in a standard 2" mirror mount (Oriel model 1450). The grating platform can be rotated by a micrometer screw which provides a turning range of about 20^{o}. The controller is designed to position the micrometer. A sketch of the grating assembly is given in Fig. C-1a with the components identified in the caption.

The controller is a simple servo system consisting of a positioner and a position encoder. The positioner is a miniature geared down (900:1) dc motor (Micro Mo Electronics - motor 050/004, gearhead 05/2-900:1) and the position encoder is a 5 kΩ - 10 turn potentiometer (Clarostat model 62-JA). The micrometer, potentiometer and motor are all mechanically coupled to one another by a common belt and pulley arrangement (PIC Design - "no-slip" type) in the drive

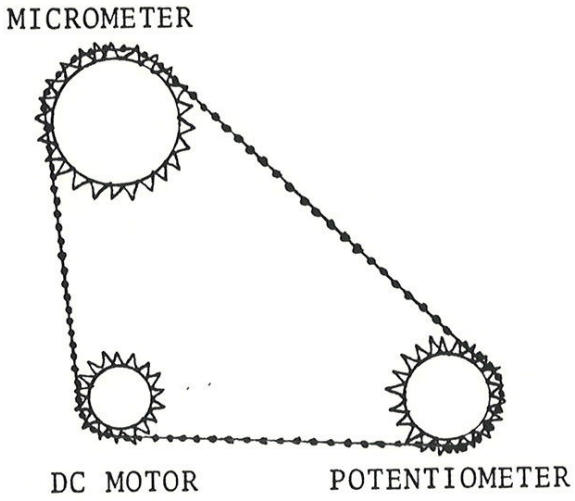

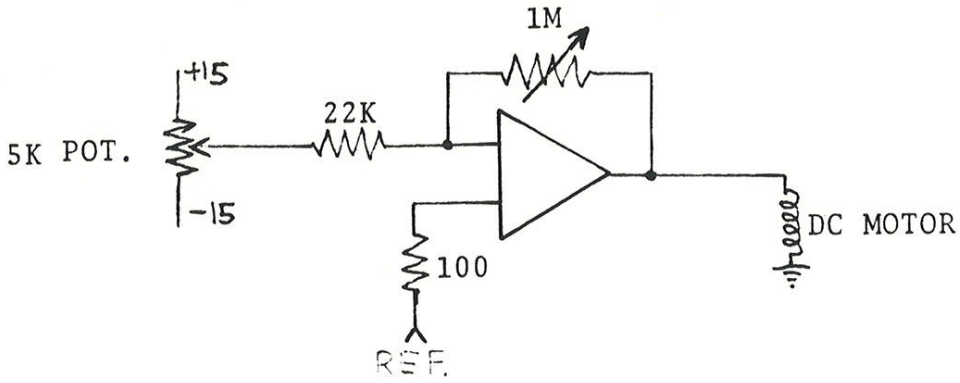

FIGURE C.1-1

(a) Sketch of the drive chain assembly. The micrometer, motor and potentiometer are indicated.
(b) Schematic of the servo electronics.

ratio, 22:72:56. A wiring diagram of the controller is given in Fig. C-1b. The differential amplifier (Texas Instruments SN747) is used to provide a motor drive voltage which is proportional to the difference between the two inputs. (Note that the direction of rotation of the motor reverses when the polarity is switched.) The motor drives the belt, which adjusts the position of the potentiometer until its variable tap voltage equals that of the reference in which case the motor comes to rest. (The gain of the servo is adjusted so that the system does not oscillate about the stable location.) For computer operation, the reference voltage is derived from a digital-to-analog converter (DAC) which is controlled by means of the CAMAC interface.

APPENDIX D

D.1 Resonance Absorption

Here we derive the power density needed to saturate the principle transition in sodium (3s → 3p). For a two-level system the optical cross-section is approximately $2\pi\lambda^2$. (This is easily derived from the Einstein expression for the rate of absorption per atom [CON 70, ch. IV], where we replace the A coefficient by $1/\tau$.) The condition for saturation is that the absorption rate equals the emission rate or in other words,

$$\frac{I}{\hbar\omega}\,\frac{\Delta\nu_n}{\Delta\nu_\ell}\,2\pi\lambda^2 = \frac{1}{\tau}\ .$$

Here $I/\hbar\omega$ is the photon number per unit time per unit area. The factor $\Delta\nu_n/\Delta\nu_\ell$ ($\Delta\nu_n$ is the resonance absorption width and $\Delta\nu_\ell$ is the laser bandwidth) is the fraction of photons which contribute to the excitation. $1/\tau$ is the spontaneous

emission rate. Using the following values we solve for I,

$$\lambda = 5.889 \times 10^{-5}\ \text{cm}^{-1}$$

$$\tau = 1.6 \times 10^{-8}\ \text{nsec}$$

$$\frac{\Delta\nu_n}{\Delta\nu_\ell} \approx 10^{-3}\ ,$$

to obtain a saturation power density of 40 watts/cm^2 . Since the laser peak power is about 1 kW and the interaction volume is 3 mm , we are heavily saturating this transition.

APPENDIX E

E.1 Level Crossing in a Two-Level System

Here we derive eq. IV.4.A-1. Let $E_A(F)$ and $E_\alpha(F)$ be the energies of two non-interacting levels which cross. Γ_A and Γ_α are their respective decay rates such that the complex energies of the levels are $E - \frac{i}{2}\Gamma$. These values are indicated by dashed lines for the energy and by arrows for the decay rate in Fig. E-1a. Now let us consider the problem where we allow coupling between the levels. The strength of the coupling is taken to be $V_{A\alpha}$ which we assume is independent of the field near the crossing. (Note that we do not allow any diagonal coupling terms since they are already included in $E_A(F)$ and $E_\alpha(F)$.) To solve for the complex energies we diagonalize the energy matrix,

$$\|H = \begin{vmatrix} E_\alpha - \frac{i}{2}\Gamma_\alpha & V_{A\alpha} \\ V_{A\alpha}^* & E_A - \frac{i}{2}\Gamma_A \end{vmatrix}$$

by solving the equation,

$$\det(\|H - \lambda \mathbb{1}) = 0$$

The new diagonal complex energies are solutions to the determinental equation,

$$\lambda = E - \frac{i}{2}\Gamma = \frac{1}{2}\left\{ E_A + E_\alpha - \frac{i}{2}(\Gamma_A + \Gamma_\alpha) \pm \sqrt{\left(E_A - E_\alpha - \frac{i}{2}(\Gamma_A - \Gamma_\alpha)\right)^2 + 4|V_{A\alpha}|^2} \right\},$$

which in terms of energy, leads to avoided crossing of the coupled levels (providing that $|(\Gamma_A - \Gamma_\alpha)| < 4|V_{A\alpha}|$). The point of closest approach between the levels occurs when $E_A = E_\alpha$ and if we let $\Gamma_A = \Gamma_\alpha$, then the separation is $2|V_{A\alpha}|$. (This fact allows us to determine $V_{A\alpha}$ from our Stark diagonalization where it is implicitly assumed that levels do not decay.) The mixing of levels also affects the decay rates in the vicinity of the crossing as illustrated in Fig. E. If the coupling between levels is sufficiently large (ie. $4|V_{A\alpha}|$

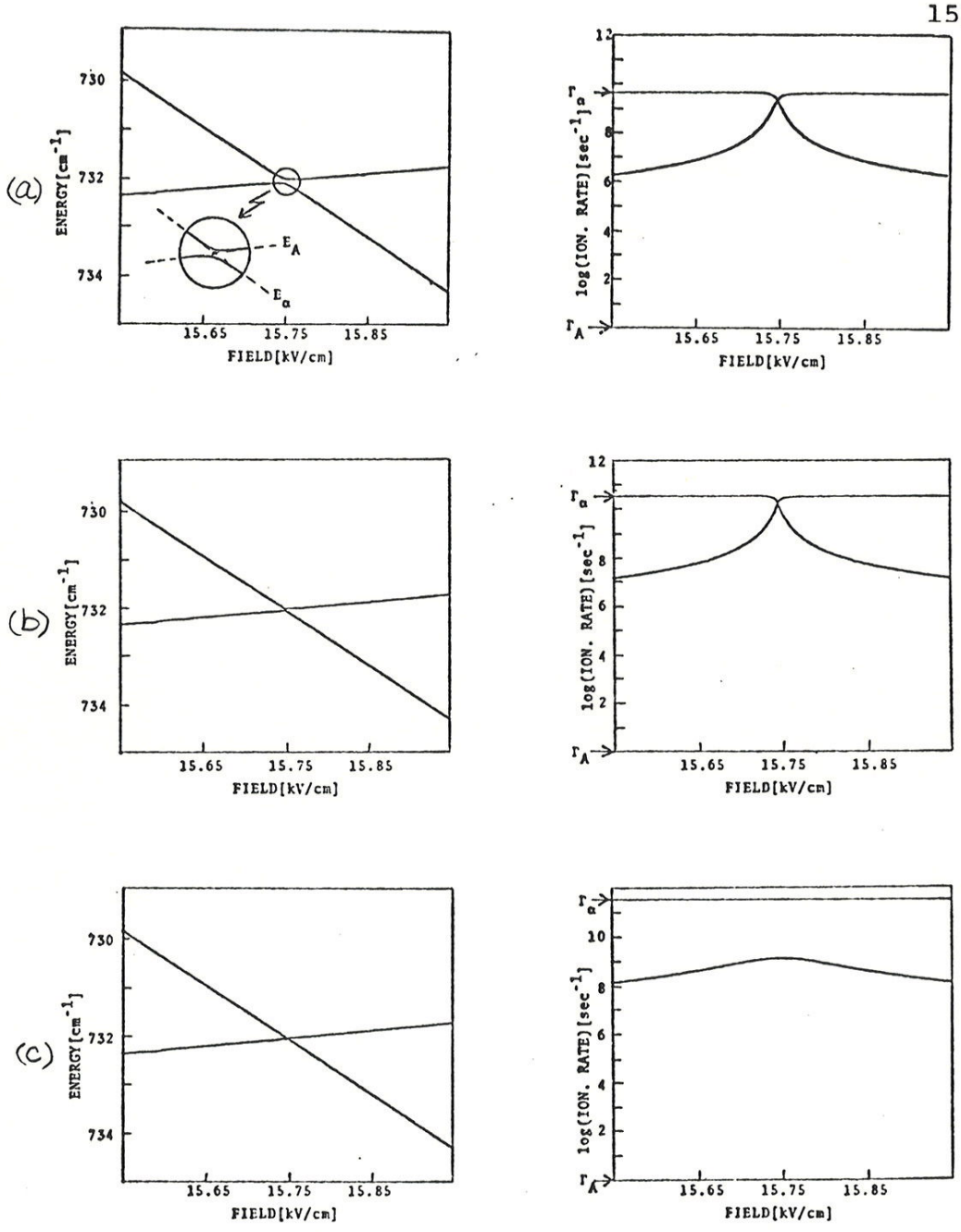

FIGURE E.1-1

Results of the two level diagonalization for levels A and α which cross at 15.75 kV/cm. The real part of the solution (energy) is at left and the imaginary part of the solution (decay rate) is at right.

(a) $|\Gamma_A - \Gamma_\alpha|/4|V_{A\alpha}| = 0.1$

(b) $|\Gamma_A - \Gamma_\alpha|/4|V_{A\alpha}| = 1.0$

(c) $|\Gamma_A - \Gamma_\alpha|/4|V_{A\alpha}| = 10.0$

GRE 57 L. C. Green, P. P. Rush and C. D. Chandler, Suppl. Astrophys. J. 3, 37 (1957).

GOU 33 S. Goudsmit, Phys. Rev. 43, 636 (1933).

GUS 75 N. A. Guschina and V. K. Nikulin, Chem. Phys. 10, 23 (1975).

HAM 62 R. W. Hamming, Numerical Methods for Scientists and Engineers (McGraw Hill, New York, 1962).

HAN 72 T. W. Hansch, Appl. Opt. 11, 895 (1972).

HAR 74 S. Haroche, M. Gross and M. P. Silverman, Phys. Rev. Lett. 33, 1063 (1974).

HAT 76 G. J. Hatton, Phys. Rev. A14, 901 (1976).

HEH 74 M. Hehengerger, H. V. McIntosh and E. Brandas, Phys. Rev. A10, 1494 (1974).

HEI 53 W. Heitler, Quantum Theory of Radiation (Oxford University Press, Oxford, 1953).

HER 76 D. R. Herrick, to be published in J. Chem. Phys.

HIL 76 R. M. Hill, T. F. Gallagher and S. A. Edelstein, in Abstracts of FICAP meeting, Berkeley, Calif., 1976.

HIR 71 J. O. Hirshfelder and L. A. Curtiss, J. Chem. Phys. 55, 1395 (1971).

HIR 76 B. Hird, H. C. Suk and A. Guilband, Rev. Sci. Inst. 47, 138 (1976).

HIS 64 J. R. Hiskes, C. B. Tarter and D. A. Moody, Phys. Rev. 133, A424 (1964).

KOC 74 P. Koch, Ph.D. Thesis, Yale University, 1974 (unpublished).

KOP 58 H. Kopferman and E. E. Schneider, Nuclear Moments (Academic Press, New York, 1958).

ILI 73 R. N. Il'in, in Atomic Physics 3 (Planum Press, New York, 1973), p.309.

LAM 52 W. E. Lamb, Phys. Rev. 85, 259 (1952).

LAN 31 C. Lanczos, Zs.fur Phys. 68, 204 (1931).

LAN 32 L. Landau, Phys. Z. Sowjetunion 1, 46 (1932).

LAN 74 L. Landau and E. Lifshitz, Quantum Mechanics (Permagon Press, New York, 1974), Vol. 2.

LAR 76 D. M. Larsen, Phys. Rev. B13, 1681 (1976).

LIA 76 P. F. Liao and J. E. Bjorkholm, Phys. Rev. Lett. 36, 1543 (1976).

LIT 74 M. G. Littman, Rev. Sci. Inst. 45, 1608 (1974).

LIT 76a M. G. Littman, M. L. Zimmerman, T. W. Ducas, R. R. Freeman and D. Kleppner, Phys. Rev. Lett. 36, 788 (1976).

LIT 76b M. G. Littman, M. L. Zimmerman and D. Kleppner, Phys. Rev. Lett. 37, 486 (1976).

MEI 37 K. W. Meissner and K. F. Luft, Ann. Phys. (Leipzig) 29, 698 (1937).

MOO 49 C. E. Moore, Atomic Energy Levels (National Bureau of Standards, USGPO, Washington D. C., 1949), Vol. I.

NEV 62 Von Neuman, in Mathematical Methods for Digital Computers (John Wiley and Sons, New York, 1962).

OPE 28 J. R. Oppenheimer, Phys. Rev. 13, 66 (1928).

PAR 67 R. G. Parsons and V. F. Weisskopf, Zs.fur Phys. 202, 492 (1967).

POU 72 S. K. Poultney, Adv. Elect. At. Phys. 31, 39 (1972).

PRI 74 D. E. Pritchard, J. Apt and T. W. Ducas, Phys. REv. Lett. 32, 641 (1974).

RAM 69 N. F. Ramsey, Molecular Beams (Clarendon Press, Oxford, 1969).

RIC 62 M. H. Rice and R. H. Good, J. Opt. Soc. Amer. 52, 239 (1962).

RIV 63 A. C. Riviere and D. R. Sweetman, in Proc. Third Intl. Conf. Phys. Elect. At.Coll. (North-Holland, Amsterdam, 1964), p.105.

RIV 68 A. C. Riviere, in Atomic and Electron Physics (Academic Press, 1968), p. 208.

SMI 66 B. M. Smirnov and M. I. Chibisov, Sov. Phys. JETP 22, 585 (1966).

TRA 29 H. R. von Traubenberg, Zs. fur Phys. 54, 307 (1929); 56, 254 (1929).

TRA 30 H. R. von Traubenberg, Zs. fur Phys. 62, 289 (1930).
H. R. von Traubenberg, Naturwiss, 18, 417 (1930).

TRA 31 H. R. von Traubenberg, Zs. fur Phys. 71, 291 (1931).

WIN 70 F. Winkler, Ph.D. Thesis, M.I.T., 1970 (unpublished).

ZEN 32 C. Zener, Proc. Roy. Soc. (London), A137, 696 (1932).

ZIM 74 P. Zimmermann, T. W. Ducas, M. G. Littman, D. Kleppner, Opt. Comm. 12, 198 (1974).

ACKNOWLEDGEMENTS

A number of people, whose aid has hastened the completion of this thesis, deserve words of thanks. First of all I thank my advisor, Dan Kleppner, for introducing me to the idea of field ionization, for making many helpful suggestions concerning this work, and for providing support, both spiritually and financially. Myron Zimmerman has generously taken the time to discuss with me both the theoretical and experimental aspects of the two important experiments described in sect. IV.4 and has made a valuable contribution. In addition, he deserves most of the credit for calculating the sodium Stark structure (see sect. II.3) and for writing the data handling computer programs. The experiments in sects. IV.2 and IV.3 were performed in collaboration with Ted Ducas, Rick Freeman, Myron Zimmerman and Dan Kleppner. I believe that we all learned a great deal from one another through this collaborative effort and in any case, I know that I certainly did. I appreciate the fact that other members of the research group have provided a forum where various ideas could be discussed. Of these members, I especially thank Bill Phillips for being willing to listen and for contributing suggestions and insight concerning this work and other things. I am grateful for the friendship of

the many past and present group members. I also express my graditude to the members of the Research Laboratory of Electronics for the services and advice that they have provided. Finally, I thank my wife, Marion, who has endured with me the arduous journey through graduate school.